THESIS FOR THE DEGREE OF DOCTOR OF PHILOSOPHY

State-of-Health Estimation of Li-ion Batteries: Ageing Models

JENS GROOT

Division of Electric Power Engineering
Department of Energy and Environment
CHALMERS UNIVERSITY OF TECHNOLOGY
Göteborg, Sweden 2014

State-of-Health Estimation of Li-ion Batteries: Ageing Models
JENS GROOT

Doctoral Thesis at the Graduate School in Energy and Environment

Division of Electric Power Engineering
Department of Energy and Environment
Chalmers University of Technology
SE-412 96 Göteborg
Sweden
Telephone: +46 (0)31 772 1000

Chalmers Bibliotek, Reproservice
Göteborg, Sweden 2014

State-of-Health Estimation of Li-ion Batteries: Ageing Models
JENS GROOT
Division of Electric Power Engineering
Department of Energy and Environment
CHALMERS UNIVERSITY OF TECHNOLOGY

Abstract

Significant research efforts are being made to understand, and ultimately mitigate, the degradation of Li-ion batteries upon usage. Currently, battery ageing models are used in order to optimise the battery usage and to achieve robust battery solutions. The purpose with this work is to obtain deeper understanding of the ageing factors for high-power graphite || $LiFePO_4$ cells and to develop a semi-empirical ageing model suitable for use in the full-vehicle simulations.

Extensive laboratory tests of commercially available graphite || $LiFePO_4$ cells were conducted with special focus on high charge and discharge rates at temperatures between +23 °C and +53 °C. Furthermore, cells were aged according to measured and simulated load profiles from heavy-duty HEVs and PHEVs. The results were analysed using *ex situ* techniques such as incremental analysis and fitted towards half-cells voltage profiles. Specifically, ageing tests with 4 C-rate charge rate in combination with 1 C-rate discharge, and cycles with pauses between steps, were found to degrade the cells significantly faster than cycles with 4 C-rate in both charge and discharge. This behaviour was also observed for the PHEV cycles with charging at 4 C-rate. In addition, *post mortem* analyses were performed on selected cells, both on electrodes and electrolytes, suggesting that the electrode degradation is unevenly distributed.

A segmented 1D semi-empirical lumped-circuit cell model was designed and coupled to a state-of-health ageing algorithm based on the test results. This model was subsequently used to forecast ageing rates and showed promising results for HEV load cycles, indicating that the cell degradation is unevenly distributed with the most severe ageing occurring close to the separator. In contrast, the model could not forecast the ageing accurately for some specific cases with high charge rates combined with low discharge rates, indicating that additional ageing mechanisms must be included to model the ageing at such severe load conditions.

Index Terms: State-of-health, battery model, lithium-ion battery, cycle life test, battery testing, HEV, PHEV, EV, ICA, DVA, impedance spectroscopy

“The most exciting phrase to hear in science, the one that heralds new discoveries, is not 'Eureka!' but 'That's funny...' ”

Isaac Asimov

Acknowledgements

This work would not have been possible without great support from a wide network within industry and academia. Still, I would like to thank some persons especially, first of all my tutors Prof. Torbjörn Thiringer and Dr. Helena Berg and for the continuous encouragement and support throughout the past six years.

I would like to thank my PhD colleagues within the "Li-Cluster" in Sweden; Dr. Matilda Klett at Argonne National Laboratory, Dr. Pontus Svens at Scania CV AB and Rickard Eriksson at Uppsala University. Our numerous discussions have been both interesting and fun, not only from a strict scientific point of view.

To all of my colleagues at *Electromobility Sub-systems* group at Volvo GTT-ATR as well as my dear friends and family: thanks for your patience and support during this long project.

I also need to thank my dog Tesla for showing me how good it is to take a walk when trying to formulate ideas from stray thoughts.

Finally, I wish to thank the Swedish Energy Agency and AB Volvo for the financial support.

Jens Groot
Göteborg, Sweden
October, 2014

Preface

In 2008, AB Volvo, Scania CV AB, the Royal Institute of Technology (KTH), Uppsala University (UU) and Chalmers University of Technology started a joint research cluster that aims to understand the ageing mechanisms of a Li-ion battery systems used in heavy-duty HEV powertrains. The cluster is co-funded by the Swedish Energy Agency and the two industrial partners.

The investigation focuses on finding the correlation between operating conditions in a real application and the fundamental ageing processes in the battery cell. Research is made on several levels; from *in situ* measurements on electrode materials and research cells made by KTH and UU to applied tests of commercially available Li-ion cells in laboratory and field applications performed by Volvo and Scania. More specifically Volvo focuses on the development of models for the ageing mechanisms.

The first part of research project at Volvo and Chalmers was concentrated around test and analysis methods and was concluded with the licentiate thesis "*State-of-Health Estimation of Li-ion Batteries: Cycle Life Test Methods*" [1] 2012 to be followed by the work summarised in this thesis, covering new test results and State-of-Health modelling.

List of Appended Papers

This thesis summarises the work published in the following papers, where paper III-VII were a result of a close collaboration by the authors.

Paper I

J. Groot, *"Statistic Method for Extraction of Synthetic Load Cycles for Cycle life Tests of HEV Li-ion Batteries"*, conference: International Battery, Hybrid and Fuel Cell Electric Vehicle Symposium (EVS-24), Stavanger, Norway, 2009.

Paper II

J. Groot, *"Battery Benchmarking and Cyclelife Test Methods"*, conference: Transport Research Arena (TRA) Europe 2010, Brussels.

Paper III

F. Savoye, P. Venet, M. Millet, J. Groot, "*Impact of periodic current pulses on Li-ion battery performance*", IEEE Transactions on Industrial Electronics 59, Issue 9, 3481-3488, (2012).

Contribution: collaboration around test methods and characterisation techniques

Paper IV

M. Klett, R. Eriksson, J. Groot, P. Svens, K. Ciosek Högström, R. Wreland Lindström, H. Berg, T. Gustafson, G. Lindbergh, K. Edström, *"Non-uniform aging of cycled commercial $LiFePO_4$//graphite cylindrical cells revealed by post-mortem analysis",* Journal of Power Sources **257** (2014) 126-137

Contribution: performed cycle life test of the analysed cells and provided full-cell analysis (capacity, EIS, power)

Paper V

J. Groot, M. Świerczyński, A.I. Stan, S. Knudsen Kær, "*On the complex ageing characteristics of high-power $LiFePO_4$-cells cycled with high charge and discharge currents*", submitted (2014)

Contribution: performed most of the cycle life tests and carried out analysis in terms of capacity and EIS

Paper VI

Y. Olofsson, J. Groot, T. Katrašnik, G. Tavčar, "*Impedance spectroscopy characterisation of automotive NMC/graphite Li-ion cells aged with realistic PHEV load profile*", IEEE International Electric Vehicle Conference 2014

Contribution: test method set-up, performed analysis to identify ageing mechanisms (ICA, EIS etc.)

Paper VII

S. Wilken, J. Groot, P. Johansson, "*Raman spectroscopy of aged electrolyte from commercial $LiFePO_4$/graphite cylindrical cells*", submitted (2014)

Contribution: cell ageing, electrical characterisation, joint development of cell disassembly technique

Table of Contents

Glossary

AC	Alternating Current
BOL	Beginning of Life
CC	Constant Current
CCCV	Constant Current / Constant Voltage
DC	Direct Current
DVA	Differential Voltage Analysis
EIS	Electrical Impedance Spectroscopy
ESR	Equivalent Series Resistance
EOL	End of Life
EV	Electric Vehicle
GITT	Galvanostatic intermittent titration technique
HEV	Hybrid Electric Vehicle
ICA	Incremental Capacity Analysis
ICE	Internal Combustion Engine
KTH	Kungliga Tekniska Högskolan / The Royal Institute of Technology
MOL	Middle of Life
OEM	Original equipment manufacturer
PHEV	Plug-in Hybrid Electric Vehicle
RMS	Root-Mean-Square
RPT	Reference Performance Test
SEI	Solid Electrolyte Interface
SOC	State of Charge
SOH	State of Health
UU	Uppsala University
xEV	HEV, PHEV or EV

Chapter 1 Introduction

Over the past decade vehicles with electrified powertrains have progressed from small-series demonstration fleets or niche products to an established variant of both passenger cars and heavy-duty commercial vehicles. Despite this strong industrialisation trend the energy storage system, most often in a form of a Lithium-ion (Li-ion) battery, is still a comparably expensive component with an uncertain or short lifetime. At the same time, significant research effort is made to both enhance the existing Li-ion battery family and to find its successor. Although a significant increase in performance, lifetime and cost has been achieved there is still an increasing demand from the automotive sector to obtain better understanding of performance limitations in general and ageing characteristics in particular.

The battery in an xEV is often deeply integrated into the drivetrain with limitations affecting drivability, vehicle performance and vehicle economics. Hence, an accurate prediction of its performance over time and as a function of usage patterns is vital to assure reliable vehicle performance and sufficient end-user economy. A multitude of different ageing models have been proposed and used, ranging from simplified and entirely empirical models to advanced first-principles models of the electrochemical processes. Whereas the former may lack sufficient accuracy, the latter ones are usually inflexible and require deep knowledge of the cell's constituents or extensive *in situ* cell characterisation. Consequently, the use of physical first-principles models is not practically possible for screening a multitude of cells for use in the automotive sector and suitable, simplified models, have to the authors knowledge not been presented in literature. Thus, the challenge from the automotive point of view is to find or develop a model accurate enough to enable sufficiently good estimate of battery service life, and flexible enough allow rapid product development.

Considering the fast technical development, testing and validation of batteries are profound. Naturally, this applies both for performance and for model development. Due to the nature of battery design, where ageing mechanisms are known to be non-linear and interdependent, accelerated testing of cycle life has proved to be very difficult. One consequence of this is that most cell manufacturers rely on simplified load cycles and

standardised operating conditions to be able to evaluate product generations and cells from competitors. In contrast, automotive OEMs often use specific sets of load conditions to target the actual application in order to verify performance and lifetime. Consequently, it is still difficult to use supplier data to estimate battery lifetime in a given application, or to base the cycle life estimate of a new cell on previous experience with a particular battery in a particular application.

1.1 Ageing Mechanisms & Characterisation of Ageing

All secondary batteries degrade over time and with usage (cycling). This degradation is manifested as a loss of available capacity, energy and/or an increase in impedance, *i.e.* reduction of power and efficiency. Due to their comparably high cost, the degradation of Li-ion batteries has been extensively studied over the past two decades. A summary of the most commonly discussed ageing mechanisms are given in the following section, with focus on graphite || $LiFePO_4$ cells.

Although the ageing mechanisms undoubtedly are complex and with rates strongly related to operating conditions [2]-[6], they can be divided into a few categories:

- Loss of active and accessible electrode material of anode and/or cathode
- Loss of cyclable lithium
- Loss of conductivity in electrodes or electrolyte

An overview of the most commonly studied ageing mechanisms on electrode level, to large extent based on the review made by Vetter *et.al* [5], is presented in Figure 1.1.

Depending on the combinations of operating conditions one or a few ageing mechanisms may dominate the overall degradation, *e.g.* at elevated temperatures [2] and high charge rates [7].

The loss of cyclable lithium in cells with graphite anodes is often dominating the total cell capacity loss [8]-[11] and may be directly linked to surface film formation, mainly to the solid electrolyte interphase (SEI). This was also confirmed by the *post mortem* analysis presented in *Paper IV*. Other side reactions, such as Li-plating and corrosion, may also consume cyclable lithium [12]-[14].

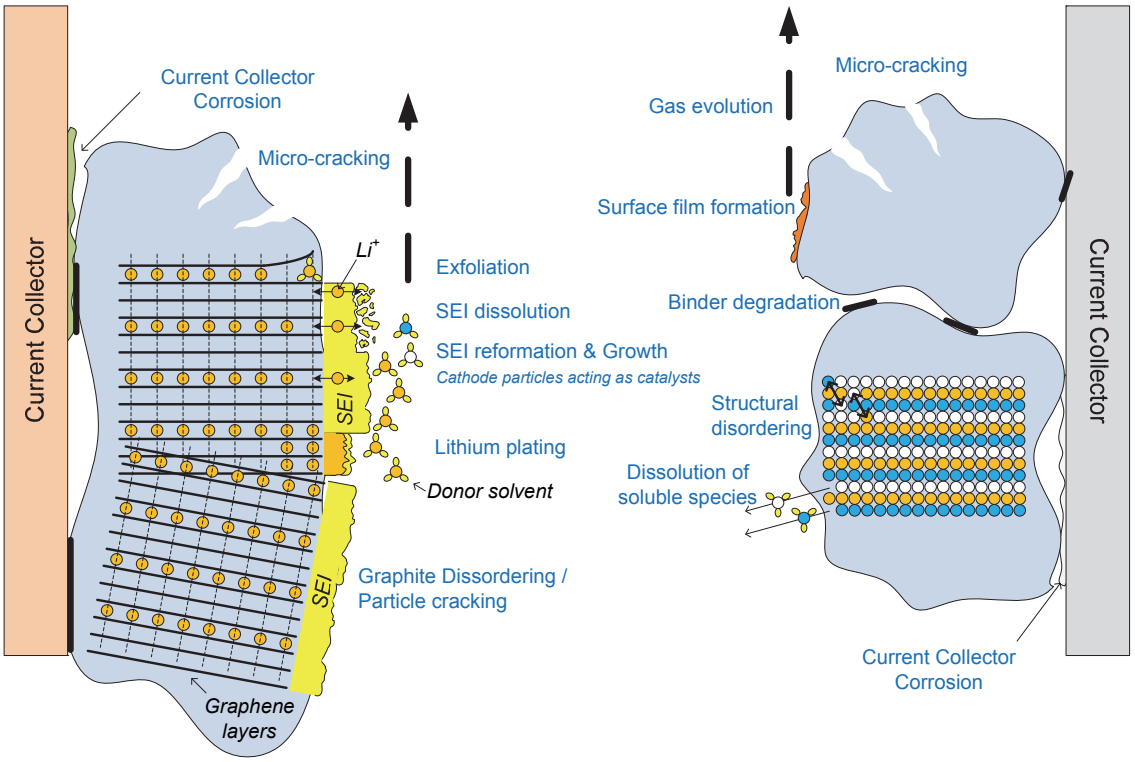

Figure 1.1 Overview of ageing mechanisms in Li-ion batteries with graphite anodes

Several studies have concluded that loss of cell capacity also can be attributed to loss of active surface area on the graphite electrode [8], [10]-[15], and that the structure of the surface in terms of porosity and tortuosity may change significantly upon cell cycling [16], [17]-[19].

Naturally, the electrolyte is also involved in the cell degradation, directly or indirectly. Several different additives are used in all commercially used electrolytes to mitigate specific degradation mechanisms, improve performance or to improve cell safety. Although important, in most cases the ageing is still dominated by loss of cyclable lithium and loss of active electrode material. *Paper VII* includes a *post mortem* study of the electrolyte of some of the cells tested in the present work and concludes that although there are specific signs of electrolyte degradation, the estimated impact on the cell performance is relatively low.

In summary, a Li-ion cell experiences ageing upon cycling and storage in terms of capacity loss or impedance growth due to side reactions consuming cyclable lithium, reducing the accessible electrode area or by changing the electrode structure.

1.2 Cell Degradation Models

Numerous methods to model the degradation of Li-ion batteries have been presented, ranging from complex physical first-principles models to purely empirical models only valid for a specific set of operating conditions. While first-principle physical models generally offer the highest accuracy and also a direct insight to the interaction between the different chemical reactions and multi-domain dependence, empirical models are considerably easier to parameterise and less computationally demanding. In some cases, especially when simulating complete vehicles with energy storage systems comprising hundreds of cells, physical first-principle models are simply too complex and demanding.

1.2.1 Physical First-Principles Models

Indeed, physical models can be designed at infinite levels of complexity, from simplified 1D-models solely considering the main electrochemical reactions to 3D multi-domain models incorporating thermal models, parasitic reactions, complex surface structures and the mechanical cell design. While [20] combined a physical model for the electrochemical domain, an empirical relation was used for the actual ageing, [15] concentrated on the degradation of graphite and $LiFePO_4$ (LFP) electrodes characterised mainly by electrochemical impedance spectroscopy (EIS). A complete cell model was also presented by [21] and [22] where a complex cell model was combined with extensive experimental data to forecast capacity fade and impedance rise for commercial LFP cells. Similar models were also developed for cells with $LiCoO_2$ (LCO) cathodes by [23], [24] and [25]. To sum up, complex first-principles physical models can undoubtedly provide both accuracy and very detailed simulation results for the specific cell modelled to the cost of computational effort and parameterisation work.

1.2.2 Empirical Models

In contrast to physical models, empirical models can be parameterised without detailed knowledge of the electrochemical cell design, albeit the accuracy may be improved by including some relations for the electrochemical reactions. Models can also be developed based on statistical and mathematical sub-models [26]-[28] or as semi-empirical models with a combination of empirical relations and electrochemical models [29]-[30]. Also, significant effort has been done to model specific ageing mechanisms such as SEI growth [31]-[32]. However, from a complete vehicle perspective, complete

degradation models are desired; preferably optimised for accuracy still while still relying on a minimum of cell knowledge and experimental validation data. In the area of large-scale energy storages for grid operation, several ageing models for LFP cells based on equivalent circuits were designed [33] and [34]. These models were validated using experimental data from simple charge/discharge cycles at various temperatures, SOC levels and current rates but did not treat complex load cycles or combinations of slow discharge and rapid charge. Also, impedance spectroscopy [35] was found to be an especially useful characterisation technique for analysing cell degradation. Furthermore, the calendar ageing, important for light duty vehicles, was treated separately by [36].

A useful empirical ageing model is given in [37] where various ageing factors are composed into one ageing expression based on extensive laboratory tests. The derived ageing model was, however, only validated towards simplified load cycles and the cell current was assumed to be evenly distributed in the cell. In contrast, the work by [15], [25], and [38] suggests that the current in a typical Li-ion cell is unevenly distributed both in liquid and solid phase, *i.e.* both over the thickness of the electrodes and the current collector area.

Despite the extensive research made in the field of ageing models, some areas have not been successfully covered yet; simple empirical models for non-accelerated operating conditions like elevated temperatures, still valid for complex load cycles for vehicles where high-rate charging is combined with charge-depleting HEV operation, have not yet been presented.

1.3 Purpose, Scope & Main Contribution

The purpose with the work covered by this thesis is to obtain deeper understanding of the ageing mechanisms in power-optimised graphite || $LiFePO_4$ cells suitable for heavy-duty xEV applications and to develop a semi-empirical ageing model. This model shall be a compromise between complexity and robustness and based on extensive laboratory tests of cycle life for the selected cell type. Neither entirely electrochemical models nor pure mathematical black-box empirical models are considered in order to find a sufficiently robust model structure suitable for further development. Furthermore, the model must cover a wide range of current rates, SOC ranges and temperatures.

Some specific scientific contributions made during the work presented in this thesis are:

- Quantification of cycle life ageing of commercially available graphite || $LiFePO_4$ cells using realistic and synthetic load profiles, with operating conditions ranging from narrow to wide SOC windows, low to high current rates and from medium to high temperatures.
- The specific characterisation of ageing, found empirically, when high charge currents are combined with low discharge currents and when pauses are introduced within high-rate cycling, both types resulted in drastically reduced cycle life.
- Comparison of ageing at synthetic and / or simplified load cycles to simplified, standardised constant current cycles.
- Assessment and development of non-invasive, *ex situ* characterisation methods.
- Further developed a segmented semi-empirical lumped-circuit electrode model used to estimate cycle life based on operating conditions.

1.4 Outline

Chapter 2 covers the performed cycle life tests, including the experimental setup, choice of load cycles and characterisation techniques. This chapter is followed by an overview of the cycle life test results in Chapter 3 where key properties such as capacity fade and impedance increase is presented. Then, the degradation is analysed and characterised in Chapter 4, focusing on loss of cyclable lithium and active anode material. The results are used as input to the model design presented in Chapter 5 where a selection of simulation results is also given, followed by concluding remarks and suggestions to future work in Chapter 6 and Chapter 7 respectively.

Chapter 2 Cycle Life Tests

In Chapter 1 an overview of the most important ageing mechanisms of Li-ion batteries was given. Based on this literature review and results previously published [1] a comparably extensive test matrix was set up to assess the impact of various ageing factors. To large extent the test procedure was identical as previously presented with a few minor modifications, first and foremost for the reference test procedure (RPT). This chapter includes a brief overview of the test procedure, the test matrix and the load cycles, followed by a description of the experimental set-up.

2.1 Test Sequence

Each cycle life test was performed on two cells in parallel on two independent test channels to be able to track cell-to-cell variations, thereby providing a rudimentary statistical average of the results. In addition, this served as input to verify that the test and the test equipment performed according to the intended scope. An overview of the test sequence is presented in Figure 2.1.

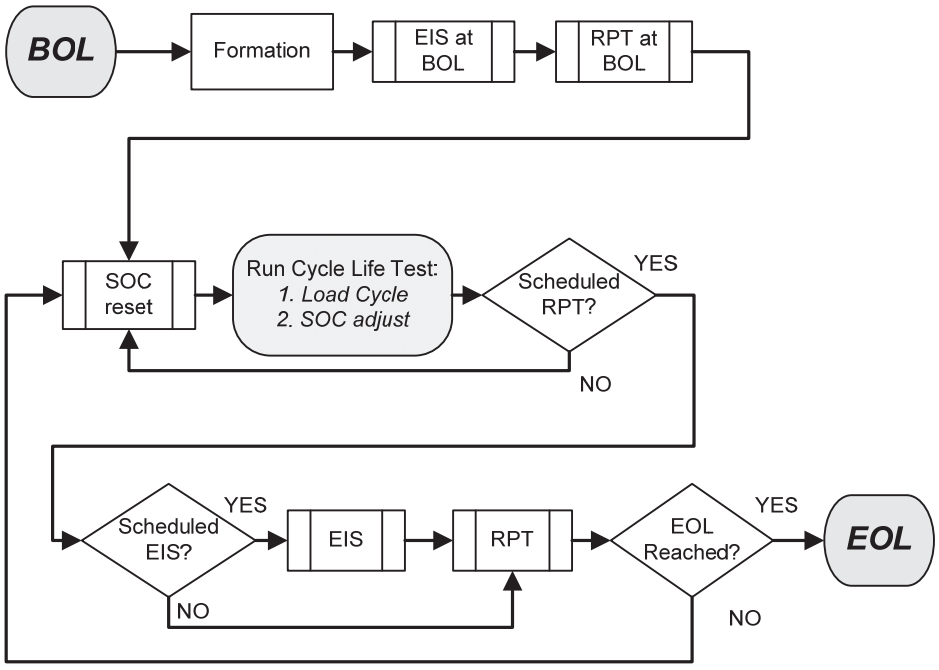

Figure 2.1 Test sequence overview

Initially, all cells were subjected to approx. four complete charge/discharge cycles at 1 C-rate in a formation test. No specific data from this test is used for further analysis;

instead it served as method to verify that the tested cells were performing according to specification and showed stable performance in terms of capacity. Following the formation test an initial RPT was conducted as well as an electrochemical impedance spectroscopy (EIS) measurement, together serving as the complete performance characteristics at beginning of life (BOL). The actual cycle life test, consisting of a specified number of load cycles with RPTs and EIS performed on a regular basis, was then started and run until the cell reached end of life (EOL) arbitrary defined as the point when the cell capacity at 1 C-rate had reached 80% of the initial capacity. For some cases testing was continued further to evaluate the performance at severe ageing. However, all comparisons in between test cases are solely based on performance at or close to the defined EOL. For cycles operating at partial SOC, a separate SOC adjustment procedure was conducted regularly. Here, special routines were developed to enable sufficient SOC control without complete charge or complete discharge.

2.2 Reference Performance Test & EIS

The design of an RPT is generally a compromise between the quality of the measured characteristics and the additional ageing the RPT itself may cause as discussed in [1] and *Paper II*. In addition, the test time needed for each RPT must be kept sufficiently short in order to keep the load conditions of the cell under test sufficiently uniform and constant. For the purpose of the present work and experience from previous tests, the RPT in this work was designed to measure the following cell properties, referring to the overview presented in Figure 2.2:

- Capacity and energy at 1 C-rate (*Step 2*) and C/10 C-rate (*Step 3*) during constant current / constant voltage (CCCV) charge and constant current (CC) discharge. An additional discharge at C/10 was performed before and after each 1 C-rate charge and discharge step to ensure a stable SOC 0% reference point.
- Charge power (*Step 4*) at 10 C-rate, 18s, CCCV, at maximum rated voltage, for initial SOC≈[30 50 70]%. Interpolated values at 50% are mainly used for inter-cell comparisons.
- Discharge power (*Step 5*) at 10 C-rate, 18s, CCCV, at minimum rated voltage, for initial SOC≈[40 60 80]%. Interpolated values at 50% are mainly used for inter-cell comparisons.
- DC impedance (relaxation) measured after each charge/discharge power pulse; ohmic (<0.1 s) and total impedance after 10 s and 600 s respectively (method

described in *Paper II*). Interpolated values at 50% are mainly used for inter-cell comparisons.

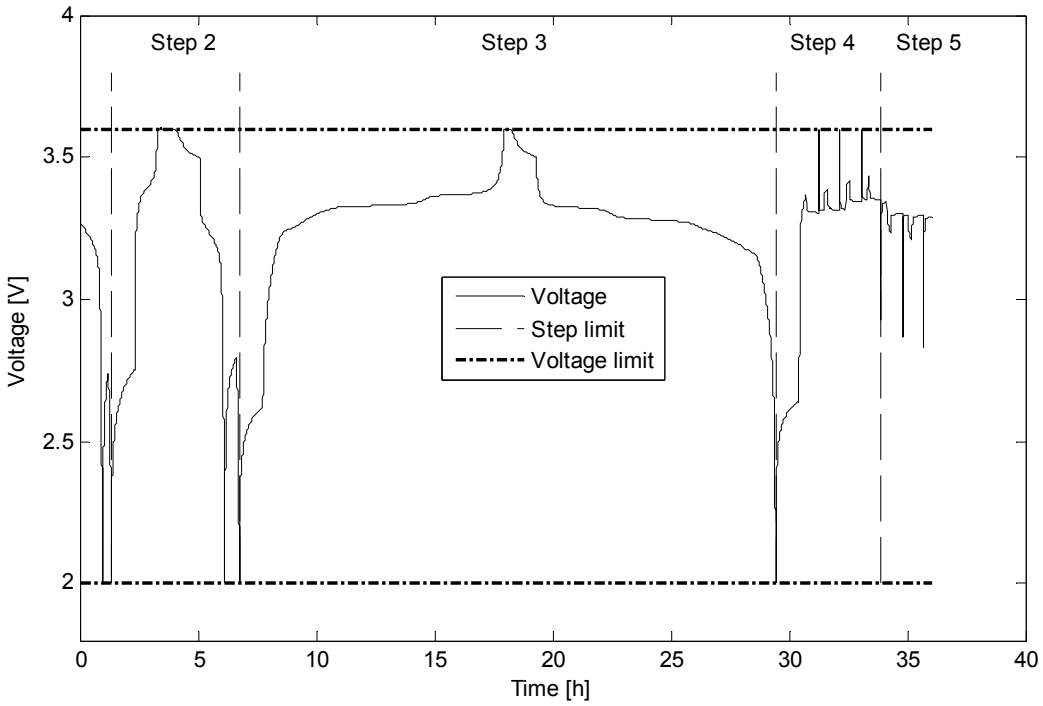

Figure 2.2 Overview of cell voltage during an RPT

The fundamental cell states SOC=0% and 100% were defined as the cell state after being discharged with C/10 C-rate to the rated minimum discharge voltage 2.0 V and after being charged with CCCV using the rated maximum voltage 3.6 V until I < C/20 C-rate respectively.

Regularly, at every other RPT and at BOL and EOL, a standard EIS was performed using potentiostatic mode, 10 mV AC, no DC polarisation, 50 kHz…10 mHz, 11 points per decade, at SOC≈[20 40 60] %. Interpolated spectrums at 50% SOC related to actual cell capacity were used for further analysis.

2.3 Temperature Control

All cycle life test and RPTs in the second phase of the work (see Table 1) were performed with forced convection, either in +22 °C air controlled laboratory environment or in climate chambers with internal forced convection. Although forced air convection was not used for the tests at +22 °C during the first test phase, each cell was monitored using a surface-mounted thermocouple thermally isolated from

surrounding air and thermal limits were set in the test program to ensure that the cells were operated and tested in the desired temperature.

2.4 Test Matrix

During the first phase of the present work, thoroughly presented in [1], a series of cycle life tests were performed according to simulated, measured and synthetic HEV and PHEV load cycles (see Section 2.6). These tests, presented in the upper section of Table 1, were designed and performed in order to identify and screen important ageing factors relevant for the considered target application.

Table 1 Test matrix

Phase	Cell ID	Cycle	Ambient air [°C]	Max. charge current [C-rate]	Max. dis-charge current [C-rate]	ΔSOC [%]	Average SOC [%]	Capacity throughput [C-rate / cycle]
	8 & 9	*A*, HEV	+23	17.3	22.3	≈20	≈35	2.02
	10 & 11	*B*, HEV	+23	15.1	23.2	≈20	≈35	2.05
	16 & 17	*A*, HEV	+32	17.3	22.3	≈20	≈35	2.05
I	14 & 15	*C*, +4/-4C	+23	3.75	3.75	100	50	0.95
	18 & 19	*C*, +4/-4C	+32	3.75	3.75	100	50	0.96
	20 & 21	*E*, PHEV 2C	+32	3.81	4.78	≈90[2]	≈60	1.00
	22 & 23[1]	*F*, PHEV 4C	+23	4.00	4.78	≈90[2]	≈60	0.99
	101 & 102	*G*, Calendar	+23[3]	0	0	0	30[3]	0.00
	123 & 124	*M*, +1/-1C	+23	1	1	100	50	0.96
	127 & 128	*N*, +2/-2C	+23	2	2	100	50	0.97
	107 & 108	*C*, +4/-4C	+23	3.75	3.75	100	50	0.96
	119 & 120	*M*, +1/-1C	+32	1	1	100	50	0.97
	125 & 126	*N*, +2/-2C	+32	2	2	100	50	0.98
	132[4]	*N*, +2/-2C	+45	2	2	100	50	0.98
	131[4]	*C*, +4/-4C	+45	3.75	3.75	100	50	0.98
	111 & 112	*J*, +4*/-4*C[5]	+23	3.75	3.75	100	50	0.97
II	109 & 110	*J*, +4*/-4*C[5]	+32	3.75	3.75	100	50	0.96
	12 & 13[1]	*D*, +4/-4C	+23	3.75	3.75	17[6]	34[6]	2.12
	117 & 118	*K*, +4/-4C	+23	3.75	3.75	17	10	2.03
	121 & 122	*L*, +4/-4C	+23	3.75	3.75	17	90	2.03
	103 & 104	*H*, +4/-1C	+23	3.75	1	100	50	0.98
	105 & 106	*I*, +1/-4C	+23	1	3.75	100	50	0.96
	113 & 114	*H*, +4/-1C	+32	3.75	1	100	50	1.00
	115 & 116	*I*, +1/-4C	+32	1	3.75	100	50	0.99
	129[4]	*H*, +4/-1C	+45	3.75	1	100	50	1.00
	130[4]	*I*, +1/-4C	+45	1	3.75	100	50	0.99

1. **Test initiated during first project phase and finalised during the second phase**
2. **Average during complete cycle life test, SOC window expands due to capacity fade**
3. **Cells stored at +22 °C controlled laboratory temperature and 30% SOC**
4. **Only one cell tested per case due to resource limitations**
5. **Pause of approx. 15 min between each step to allow for thermal relaxation**
6. **Approximate values. The average SOC over the complete cycle life test was 34%**

In addition, a few tests using CCCV tests at 3.75 C-rate were performed to investigate the ageing at full SOC range. To large extent these tests were used to test and validate the ageing model presented in Chapter 5.

For the second phase of this research project a new batch of graphite || $LiFePO_4$ cells were put under test. Here, the scope was set to characterise specific ageing factors such as charge rate, discharge rate, temperature, pauses, and SOC range. An overview of the cycle properties is given in Table 1 with specific properties presented in Chapter 3.

2.5 Experimental Setup

All tests were performed using the same test equipment and two climate chambers. Whereas the tests performed during the first phase, with cells 8-23, were performed without forced air-cooling at +22 °C, the remainder of the tests were performed with either forced air convection in ambient air in a custom built cell holder (Figure 2.3) or inside climate chambers with circulation fans. Hence, the temperature control during the second phase was greatly improved.

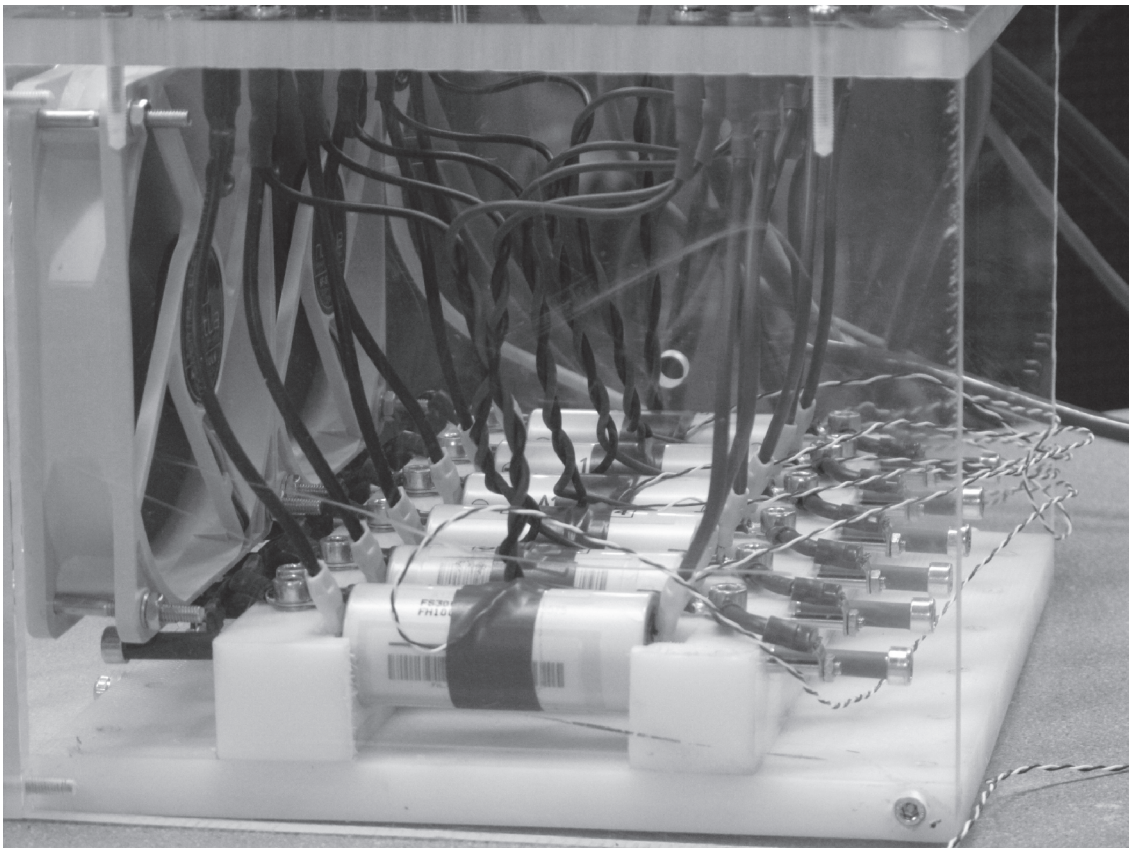

Figure 2.3 A123 ANR26650M1A cells mounted in custom-made cell holder with fans

Two batches of cells, delivered 2010 and 2012 respectively, were used. All cells within each batch had the same manufacturing date and specification according to the supplier and should therefore be considered to have uniform performance. Details are given in Table 2 below.

Table 2 Cell specification of A132 ANR26650M1A [39] & [40]

Component / property	Description / value
Cathode	$LiFePO_4$
Anode	Graphite
Electrolyte	$LiPF_6$ in unspecified solvent
Separator	Unspecified
Capacity	2.3 Ah
Nominal voltage	3.3 V
Maximum discharge current	Approximately 70 A continuous
Maximum charge current	Approximately 10 A continuous
Weight	70 g
Type	Cylindrical

2.5.1 Test Equipment

A programmable multi-channel battery test equipment from MACCOR® [41] was used for all cycle life tests, see specification below.

MACCOR® Series S4000 [41]

Current Range: -60…+60 A

Voltage Range: 0...5 V

Voltage Accuracy: 0.01% + 1 digit

Current Accuracy: 0.02% + 1 digit

Temperature Accuracy: ±0.5 °C

Impedance spectroscopy were performed using a programmable potentiostat / impedance spectrometer from GAMRY® [42] with specification below and an accuracy plot presented in Figure 2.4.

GAMRY® Reference 3000 [42]

Current Range: -3…+3 A

Voltage Range: 0...5 V

Voltage Accuracy: ± 1 mV ±0.3% of reading

Current Accuracy: ±0.3% range ± 10 pA

Current Ranges: 11 (300 pA-3 A)

Impedance Range: 0.1 mOhm-1 TOhm

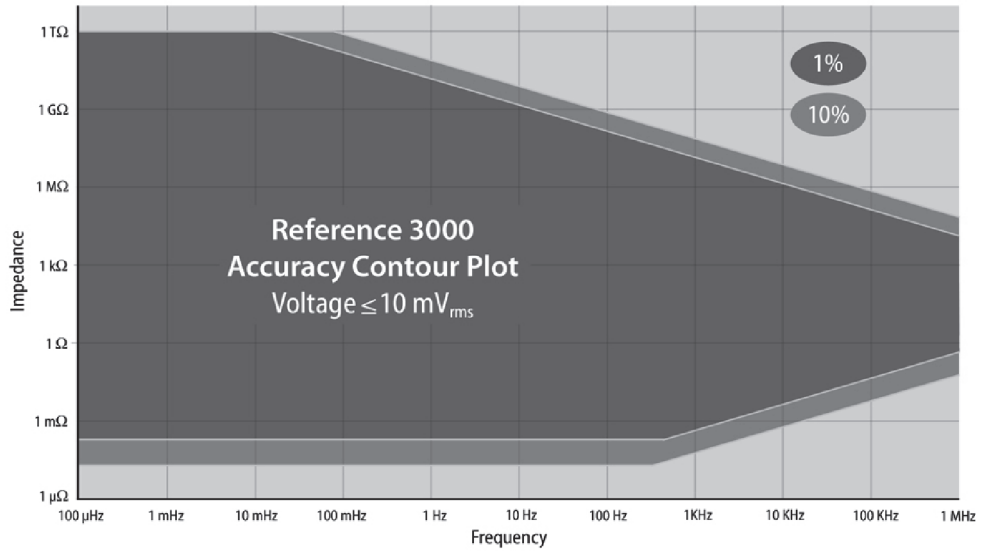

Figure 2.4 Accuracy for GAMRY® Reference 3000 [42]

A small programmable climate chamber from MACCOR® was used to control the temperature of cells cycled at +32 °C ambient temperature and second chamber from WEISS® was used for tests at +45 °C. Both chambers have a specified temperature uniformity and accuracy of ±0.5 °C.

2.6 Load Cycle Overview

All constant current, full SOC range cycles (*C, M, N, H, I* & *J*, see Table 1) were used within the cell's full operational window, *i.e.* charged to 3.6 V with CCCV until I ≤ C/20 and discharged with CC to 2.0 V. No pauses between steps were included except for *Cycle J* in which an approx. 15 min rest period was integrated to allow cell relaxation and temperature equalisation. Most of the test results, and a more detailed description, are given in *Paper V*, with typical SOC profiles for the first 120 min presented in Figure 2.5 to Figure 2.10.

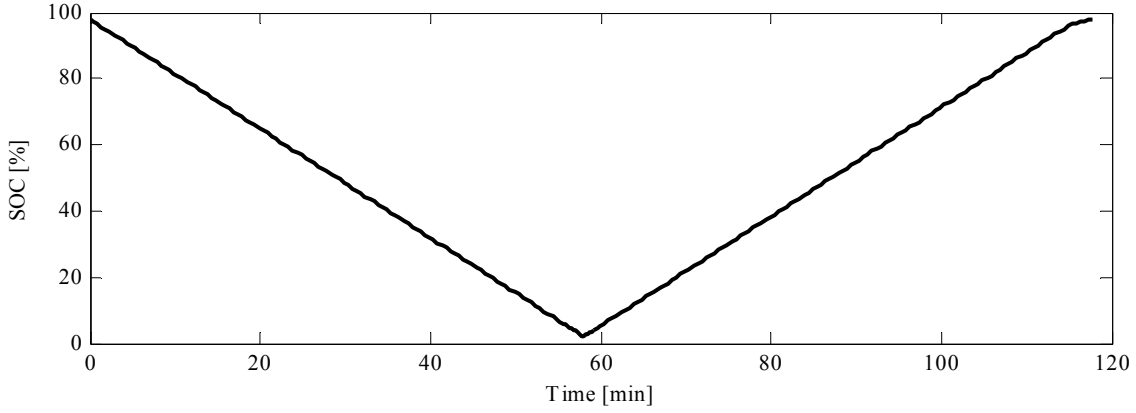

Figure 2.5 SOC overview of *Cycle M*; 1C charge and 1C discharge

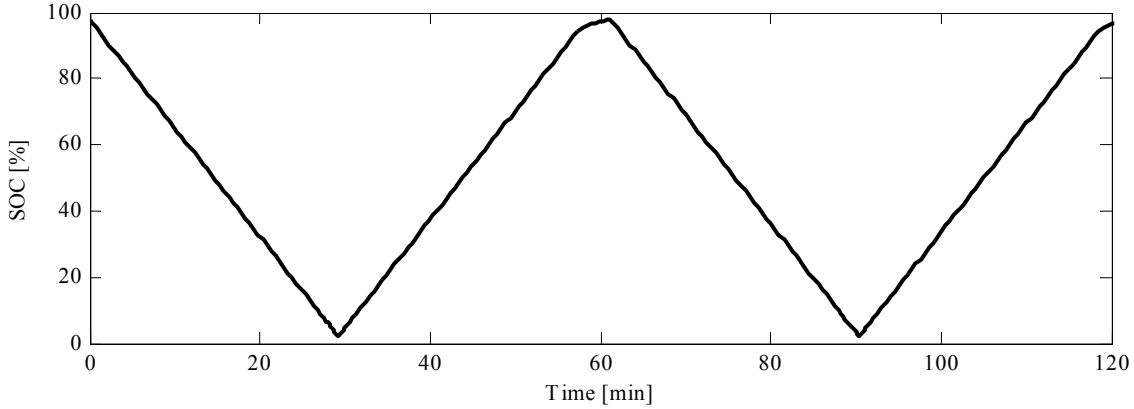

Figure 2.6 SOC overview of *Cycle N*; 2C charge and 2C discharge

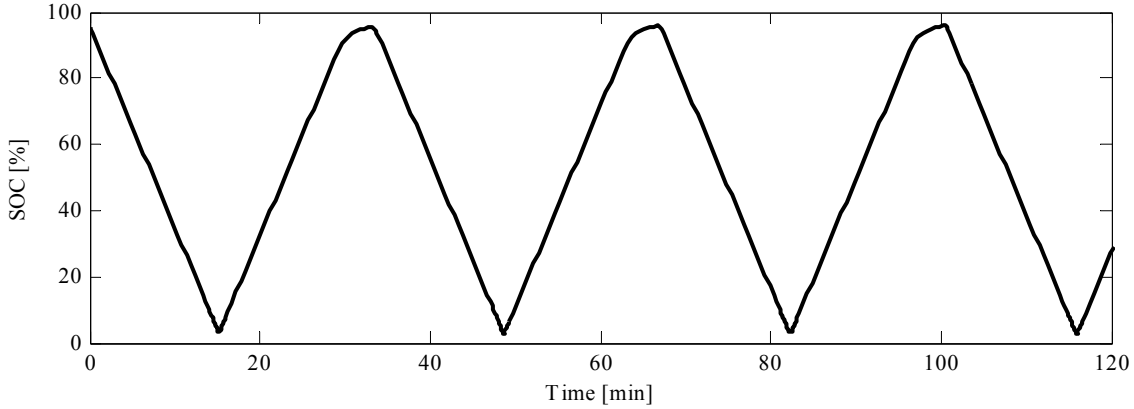

Figure 2.7 SOC overview of *Cycle C*; 4C charge and 4C discharge

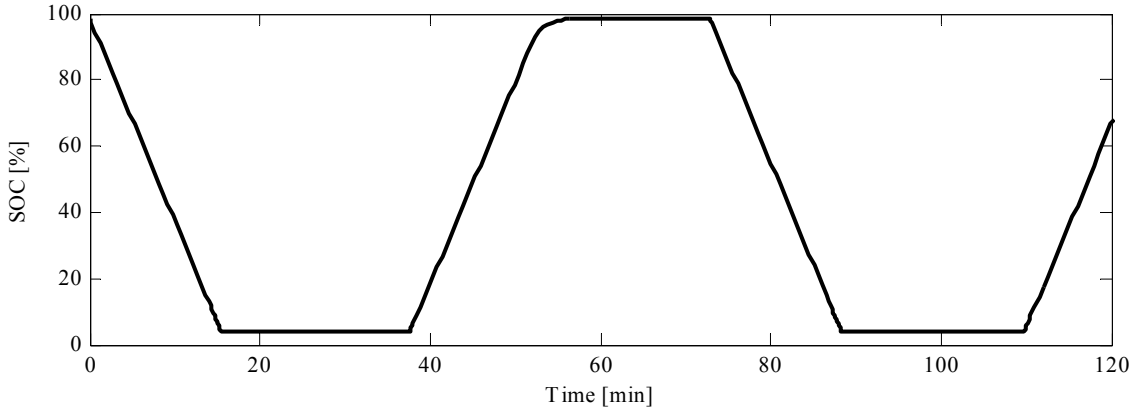

Figure 2.8 SOC overview of *Cycle J*; 4C charge and 4C discharge with pause in between steps

None of the wide SOC, constant current cycles can be regarded as representative for heavy-duty xEVs but they do serve as valid reference cycles for validation of ageing models and to correlate the ageing of complex cycles to that of the more established simplified cycles. In addition, *Cycle H* and *I* were designed to target the specific ageing occurring when very different current rates and cycling patterns are combined.

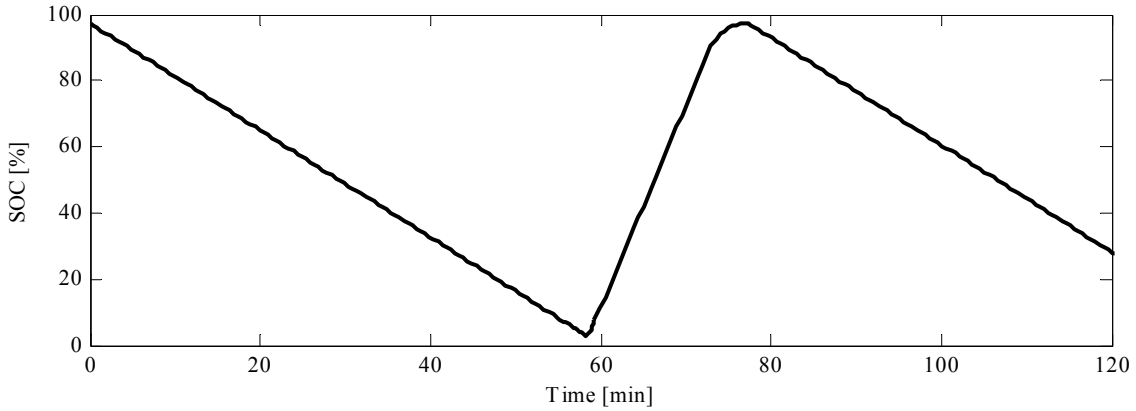

Figure 2.9 SOC overview of *Cycle H*; 4C charge and 1C discharge

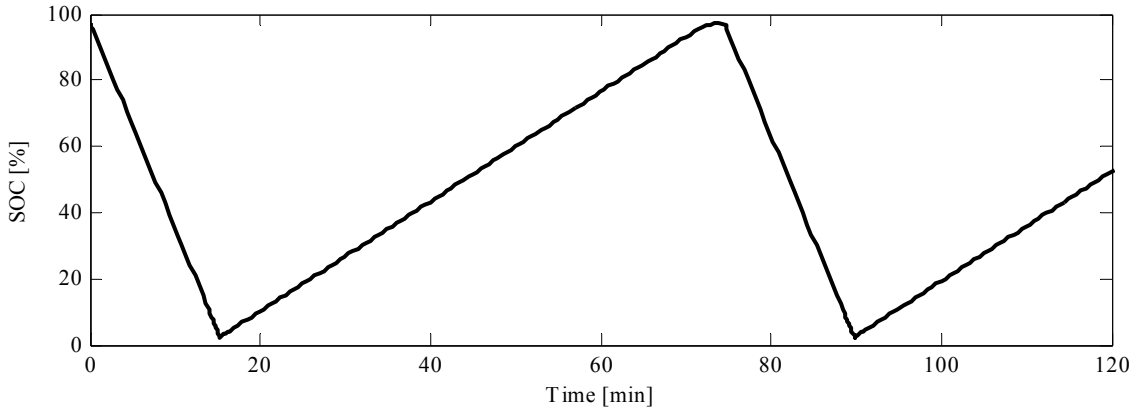

Figure 2.10 SOC overview of *Cycle I*; 1C charge and 4C discharge

The three cycles operating in a narrow SOC range, *Cycle D*, *K* & *L*, were all cycled with 4 C-rate in a SOC window of approx. 17% at either low SOC (0-20%, *Cycle K*), HEV target SOC (20-40%, *Cycle D*) or high SOC (80-100%, *Cycle L*), see Figure 2.11.

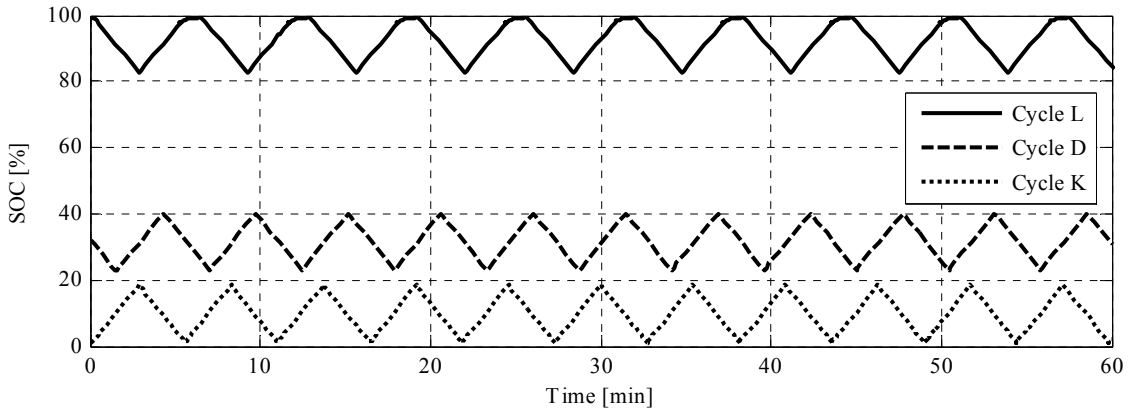

Figure 2.11 SOC overview of *Cycle D, K* & *L*; 4C charge and 4C discharge within 20% ΔSOC

These three cycles were specifically designed to isolate the ageing factors related to SOC regions.

The HEV cycles were based on measured or simulated load profiles from heavy-duty vehicles and are described in full in [1]. A key difference between the two cycles is that the simulated load cycle is based on a statistical model, fully presented in *Paper I*. These cycles were included in the cycle life test matrix for two reasons. Firstly, to serve as validation cycles of the ageing model and secondly, to take into consideration the possible additional stress that transient operation may introduce as also discussed in *Paper III*.

Both HEV cycles operate in a narrow SOC range of approx. 20-45% (Figure 2.12 & Figure 2.13).

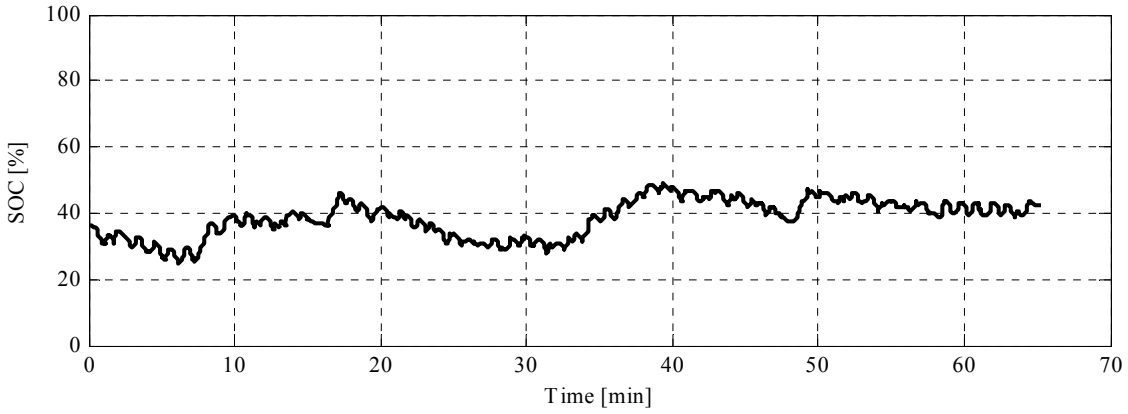

Figure 2.12 SOC overview of *Cycle A*; logged HEV cycle

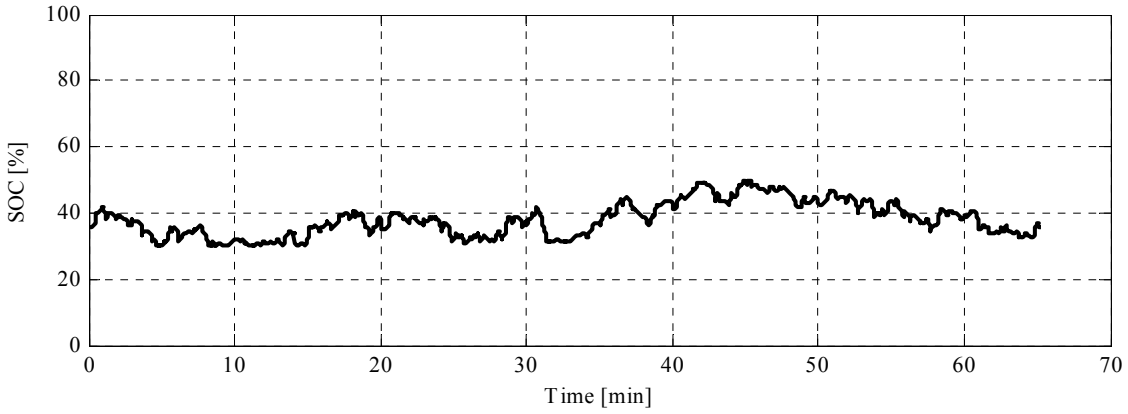

Figure 2.13 SOC overview of *Cycle B*; synthetic HEV cycle

The two PHEV cycles utilise almost the entire SOC range (Figure 2.14 & Figure 2.15). This is arguably more similar to the battery load cycles seen in pure EV applications but with one main difference; the re-charge rate (2 and 4 C-rate) that is considerably higher than for typical passenger car applications.

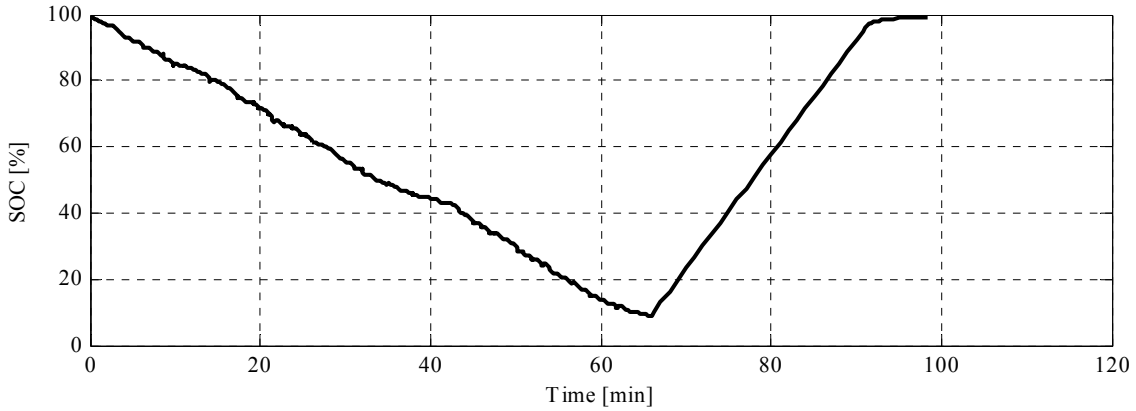

Figure 2.14 SOC overview of *Cycle E*; simulated PHEV cycle with 2 C-rate recharge

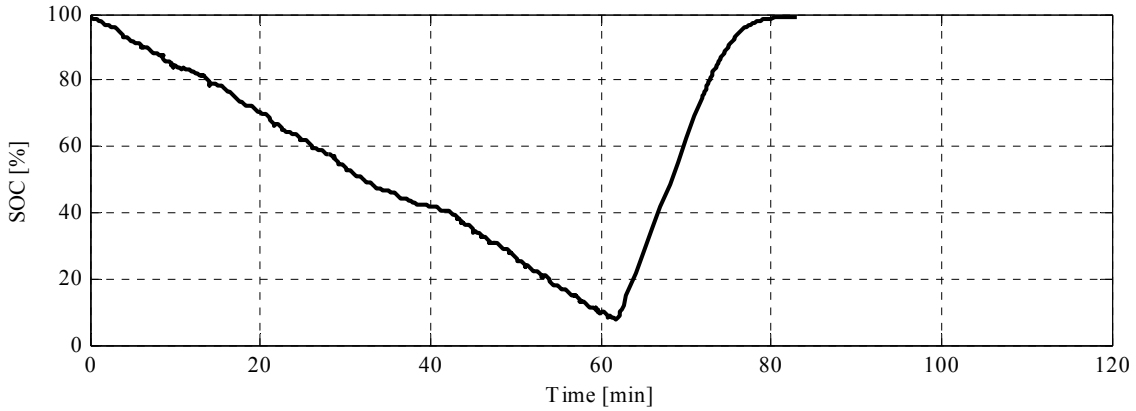

Figure 2.15 SOC overview of *Cycle F*; simulated PHEV cycle with 4 C-rate recharge

The ageing of Li-ion cells for demanding PHEV passenger car applications was treated separately in a related project and presented in *Paper VI*.

Chapter 3 Ageing Test Results

The cycle life of any battery is, naturally, best defined from an application point of view. That is, the end-of-life is defined when the battery fails to fulfil the application requirements. In vehicles, the EOL is often defined as the point at which the battery shows a certain capacity fade or power fade; for EVs the capacity is often the most critical performance property and in a HEV the maximum power and the power efficiency has a direct impact on fuel consumption. However, the vast majority of published research uses the capacity criteria rather than a definition based in power. Hence, in order to compare results in a straight-forward manner, the EOL for the cells in the present work is arbitrary defined as the point in time (or number of cycles) when the capacity fade is 20% in relation to the initial capacity.

This chapter includes an overview of test results for all studied cells in terms of capacity and power. Since RPTs are performed at a regular basis with a fixed interval, measurements may be taken just before, or after, the defined EOL is reached. To facilitate a fair comparison between test cases, key parameters are interpolated to the point of exactly 20% capacity fade. In addition, a section presenting the calendar ageing tests is included at the end of this chapter. Further analysis of test results and ageing mechanisms are presented in Chapter 4.

Table 3 summarises the load conditions and selected test results for all treated test cases. Here, the EOL capacity throughput is defined as

$$C_{TP} = \int_0^{T_{Cycle}} |i| dt \frac{1}{Q_{Ref} \cdot 3600 \cdot 2} \tag{3.1}$$

where Q_{ref} is the nominal cell capacity. This definition of C_{TP} represents a normalised value, where one C_{TP} is equal to one full cycle including both charge and discharge. The EOL test time indicated in the table represents the complete duration of the cycle life test, from start of test to end of test, based on calendar time. That is, rest periods in between tests and RPTs are included in this value.

Table 3 Test Results Overview

Phase	Cell ID	LOAD CONDITIONS				TEST RESULTS			
		Cycle	Average temp. [°C]	Min. SOC [%]	Max. SOC [%]	EOL Cap. TP [cycles]	EOL Test Time [days]	EOL Ohmic R [%]	EOL 10mHz |Z| [%]
I	8 & 9	*A*, HEV	31.5	≈25	≈50	8417	437	110	116
	10 & 11	*B*, HEV	35.7	≈25	≈50	7108	298	103	114
	16 & 17	*A*, HEV	38.7	≈25	≈50	10033	423	123	118
	14 & 15	*C*, +4/-4C	35.6	0	100	1444	49	108	111
	18 & 19	*C*, +4/-4C	40.3	0	100	1451	43	116	111
	20 & 21	*E*, PHEV 2C	35.2	10[2]	100	2580	229	102	102
	22 & 23[1]	*F*, PHEV 4C	30.4	10[2]	100	543	45	103	111
II	101 & 102	*G*, Calendar	22[3]	30[3]	30[3]	-	>1000	-	-
	123 & 124	*M*, +1/-1C	23.5	0	100	4286	383	118	106
	127 & 128	*N*, +2/-2C	26.1	0	100	2943	136	114	106
	107 & 108	*C*, +4/-4C	29.2	0	100	2196	88	108	102
	119 & 120	*M*, +1/-1C	32.0	0	100	3896	370	115	108
	125 & 126	*N*, +2/-2C	34.4	0	100	2270	106	113	104
	132[4]	*N*, +2/-2C	46.9	0	100	1687	85	117	109
	131[4]	*C*, +4/-4C	52.8	0	100	1061	29	114	110
	111 & 112	*J*, +4*/-4*C[5]	27.1	0	100	740	45	108	102
	109 & 110	*J*, +4*/-4*C[5]	35.2	0	100	853	55	107	103
	12 & 13[1]	*D*, +4/-4C	29.2	≈20[6]	≈45[6]	16740	600	100	117
	117 & 118	*K*, +4/-4C	30.5	0	20	2147	69	134	148
	121 & 122	*L*, +4/-4C	29.5	80	100	6103	242	109	104
	103 & 104	*H*, +4/-1C	23.3	0	100	517	29	116	122
	105 & 106	*I*, +1/-4C	25.0	0	100	1537	92	96	101
	113 & 114	*H*, +4/-1C	33.5	0	100	759	50	99	113
	115 & 116	*I*, +1/-4C	34.1	0	100	2488	169	101	98
	129[4]	*H*, +4/-1C	46.7	0	100	634	39	108	116
	130[4]	*I*, +1/-4C	46.6	0	100	1989	138	113	110

1. **Test initiated during first project phase and finalised during the second phase**
2. **Average during complete cycle life test, SOC window expands due to capacity fade**
3. **Cells stored at +22 °C controlled laboratory temperature and 30% SOC**
4. **Only one cell tested per case due to resource limitations**
5. **Pause of approx. 15 min between each step to allow for thermal relaxation**
6. **Approximate values. The average SOC over the complete cycle life test was 34%**

The cell impedance is here represented by two values, ohmic resistance and 10 mHz impedance, extracted from an interpolated EIS measurement at EOL and fitted towards the impedance model presented in Figure 3.1.

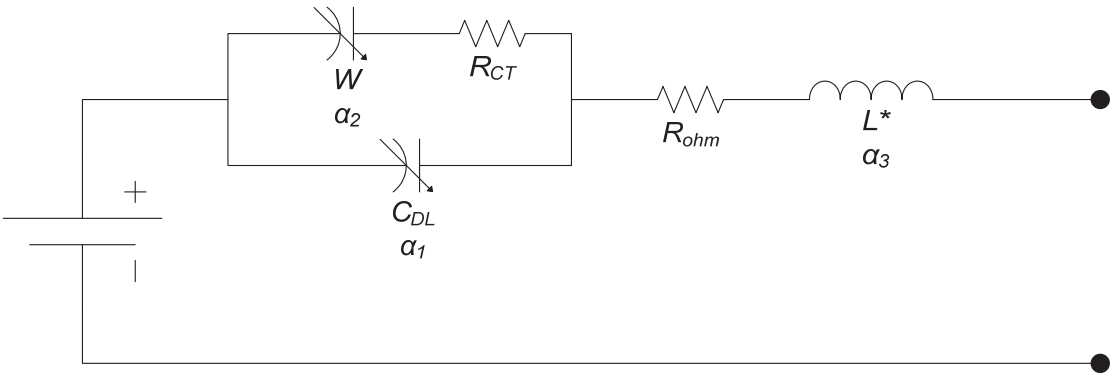

Figure 3.1 Small-signal impedance model for a Li-ion battery cell with parameters extracted via least-square fitting method

In this model, both C_{DL} and the Warburg impedance W are modelled with CPEs (constant phase elements) with transfer function

$$Z_{CPE} = \frac{1}{C \cdot (j\omega)^{\alpha}} \tag{3.2}$$

and the inductance L^* is multiplied with a correction factor according to

$$Z_L = L \cdot (j\omega)^{\alpha} \tag{3.3}$$

to compensate for measurement inaccuracies resulting from stray inductance and skin effect of instrument cabling.

Firstly, it can be noted that the test duration in terms of test time and capacity throughput varies significantly; ranging from about one month and 500 cycles to over two years and almost 17 000 cycles. Secondly, there are noteworthy differences in cycle life between cycles with comparably similar load conditions and cycle properties.

3.1 Capacity Fade

Cycle M, N & C represent three variants of standardised cycles at full SOC range, designed for simple and short-duration tests and commonly used by cell manufactures. The capacity fades for these cycles are presented in Figure 3.2 and Figure 3.3 for temperatures ranging from +24 °C to +53 °C. In general, the ageing trends are quite clear for these cycles; an increase in temperature or current rate leads to accelerated ageing with the current rate being the strongest factor.

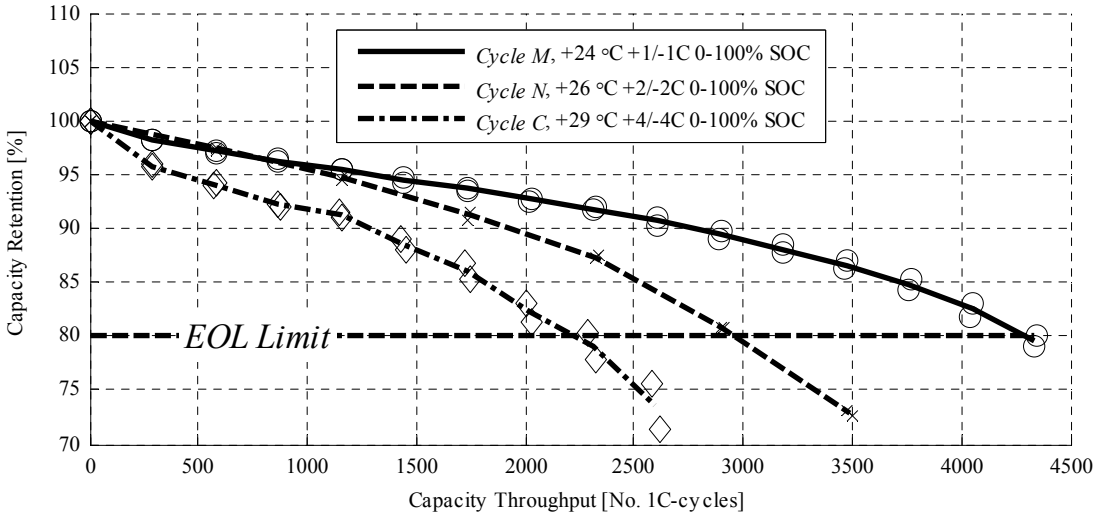

Figure 3.2 Capacity retention for *Cycle M, N & C* at +24…+29 °C. Markers indicate the measurements of individual cells and the lines indicate the average.

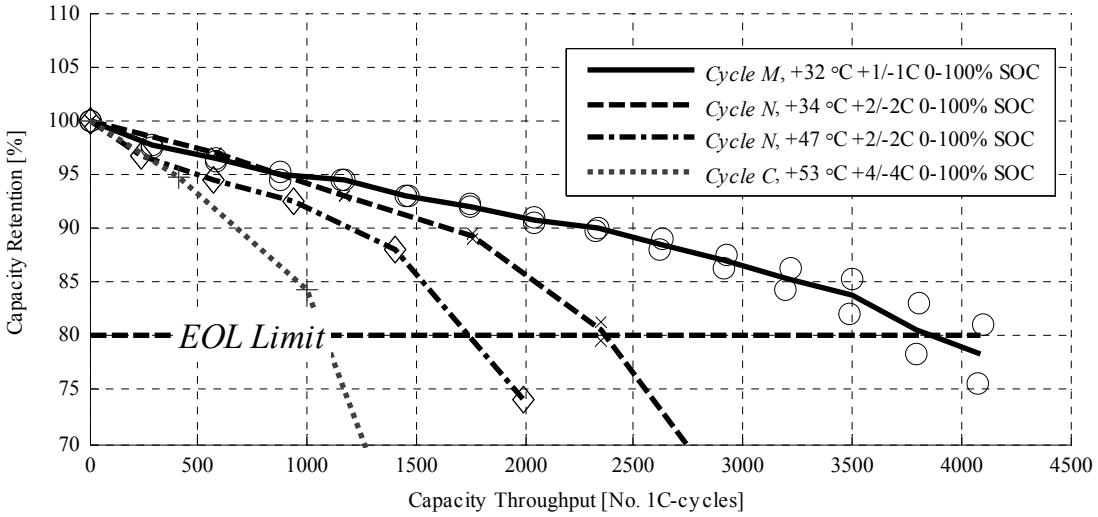

Figure 3.3 Capacity retention for *Cycle M, N & C* at +32...+53 °C. Markers indicate the measurements of individual cells and the lines indicate the average.

In strong contrast to the results for *Cycle M, N & C*, the results with *Cycle J* which includes rest periods of approx. 15 min in between steps show a drastically increased ageing rate (Figure 3.4) despite similar temperatures and identical current rate for charge and discharge compared to *Cycle C*.

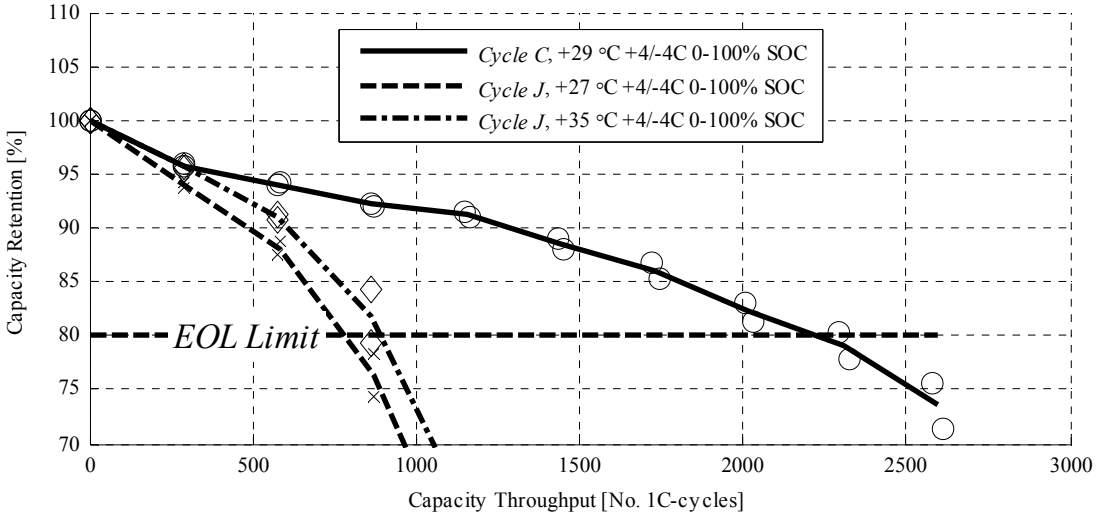

Figure 3.4 Capacity retention for *Cycle C & J* at +27...+35 °C. Markers indicate the measurements of individual cells and the lines indicate the average.

Two tests were performed using *Cycle J*, with temperatures below and above the reference case with *Cycle C*, and both tests yielded very short cycle life. This test can also be seen as an illustrative example of the complexity and non-linearity of Li-ion cell ageing. Further analysis of this case is given in Chapter 4.

Similarly to the result with *Cycle J*, *Cycles D, K & L* (Figure 3.5) show a significant spread in cycle life with the only cycle difference being the SOC range; low SOC for *Cycle K*, medium SOC for *Cycle D* and high SOC for *Cycle L*. In addition to the vast difference in cycle life, it shall also be noted that the ageing characteristics in terms of fade rate are very different; whereas *Cycle D* leads to a slow and almost linear fade rate until EOL, *Cycle K* causes a very rapid initial fade followed by slower and linear fade and *Cycle L* is characterised by the opposite behaviour compared to *Cycle K*. Another observation is that the spread in degradation rate between the two cells cycled at *Cycle L* is significant close to EOL.

Further differences between these cycles, and a possible explanation to the sudden drop in capacity observed for *Cycle D* after approx. 7000 capacity throughputs, is given in Section 4.2.

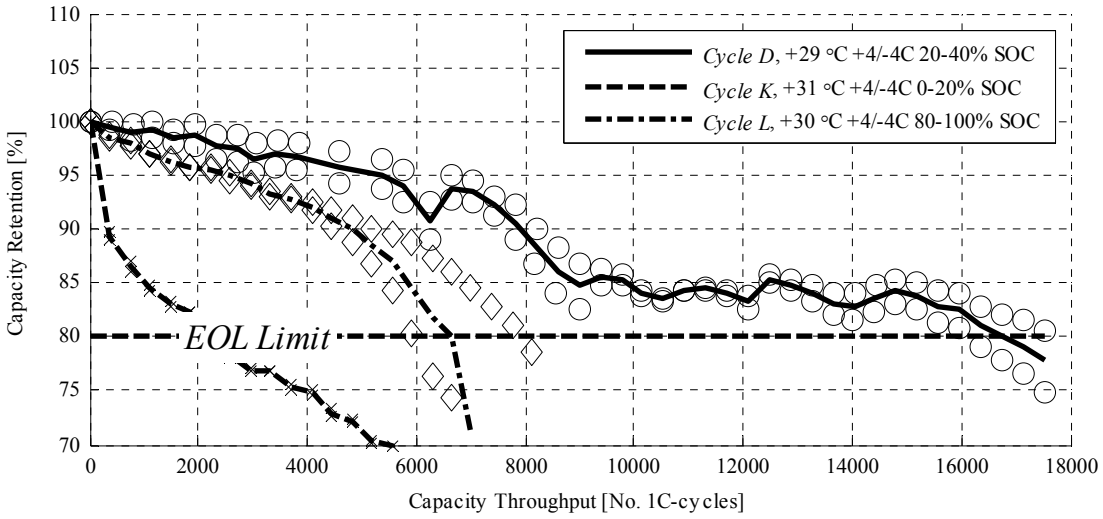

Figure 3.5 Capacity retention for *Cycle D, K & L* at +29…31 °C. Markers indicate the measurements of individual cells and the lines indicate the average.

Cycles H & I show yet another difference to the symmetric *Cycle M, N & C*; at low temperatures, the combination of low discharge rate and high charge rate in *Cycle H* leads to an exceptionally fast ageing (Figure 3.6), significantly faster than all other cycles, including *Cycle C* that has the same charge current but a *higher* discharge rate.

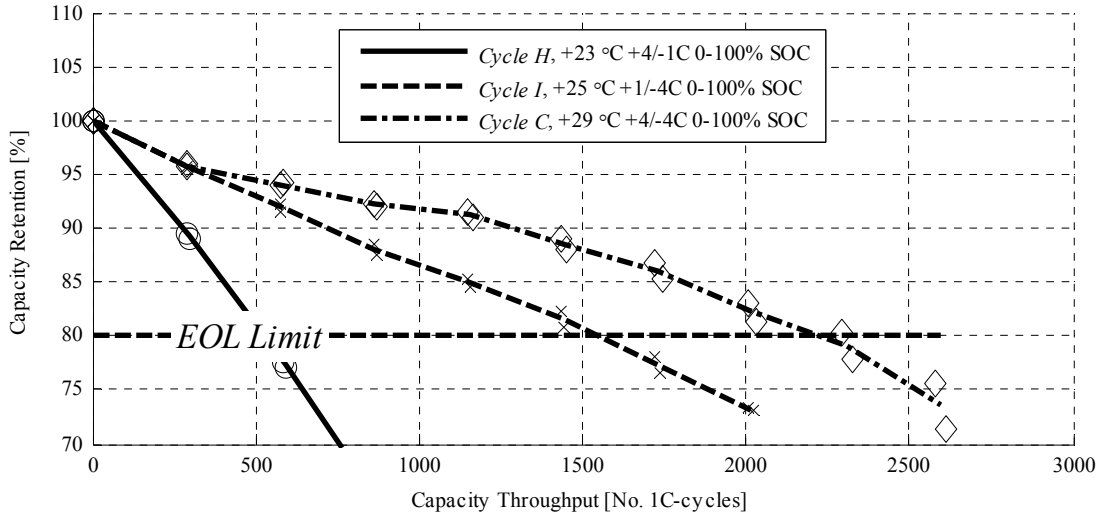

Figure 3.6 Capacity retention for *Cycle H, I & C* at +23…+29 °C. Markers indicate the measurements of individual cells and the lines indicate the average.

The average temperature differs between the two tests but when the same test cases at higher temperatures (Figure 3.7 & Figure 3.8) are studied, the same relation between *Cycle H & C* is shown, indicating that the temperature in itself cannot explain the differences.

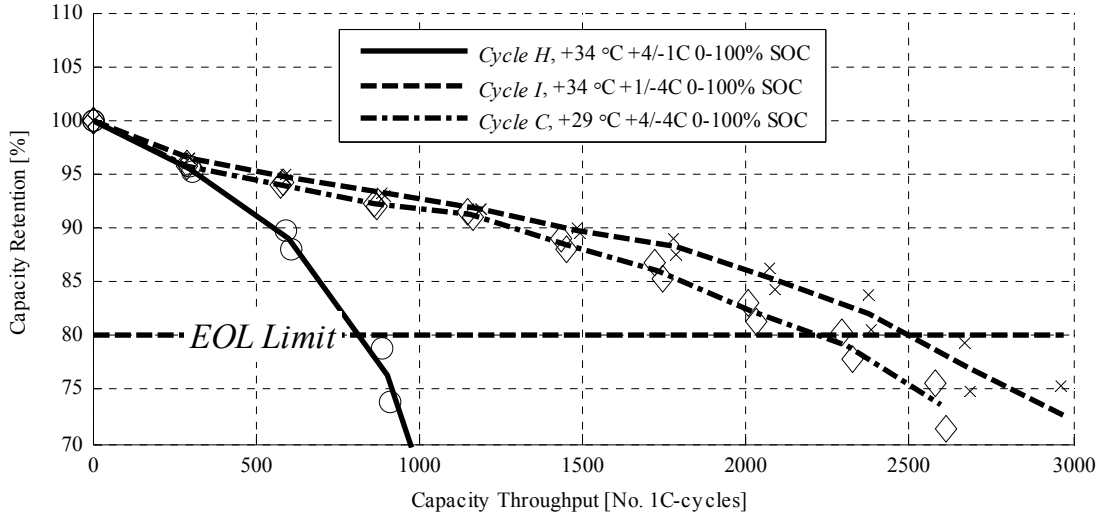

Figure 3.7 Capacity retention for *Cycle H, I & C* at +29…+34 °C. Markers indicate the measurements of individual cells and the lines indicate the average.

Furthermore, *Cycle I* with its lower charge rate compared to *Cycle C* does not lead to a noteworthy increase in cycle life, in sharp contrast to what is generally regarded as battery life-extending method, except for at very high temperatures (Figure 3.8) where the cycle life for *Cycle I* is almost twice that of *Cycle C*.

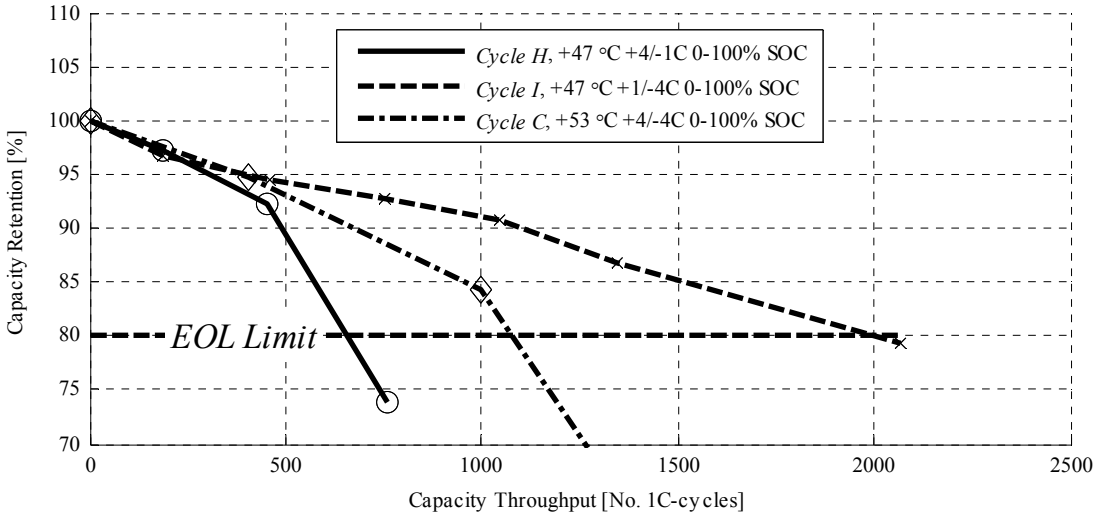

Figure 3.8 Capacity retention for *Cycle H, I & C* at +47…+53 °C. Markers indicate the measurements of individual cells and the lines indicate the average.

3.2 Impedance Growth

In general, merely marginal power fade at discharge was measured despite a noteworthy impedance growth. In contrast, the charge power was significantly affected for most cases, although not to the extent that cycle performance was reduced. Despite the comparably small decrease in maximum power, an impedance growth may reduce the power efficiency considerably, in turn reducing the potential fuel saving when used in HEVs and PHEVs. Furthermore, increased losses lead to an increase in cell temperature, in turn accelerating the degradation or requiring a more efficient cooling system.

Interestingly, an initial decrease in impedance, and corresponding increase in power, was measured for some cases, well in-line with a reduced charge transfer impedance (see Chapter 4). This was also observed in *Paper VI* for a different Li-ion cell type. Although this has a positive effect on vehicle performance, it may also be regarded as a sign of fast ageing as it was primarily observed for test cases with short cycle life.

At temperatures below +30 °C, *Cycles N & C* show similar trends for the growth of ohmic impedance (Figure 3.9) and charge transfer impedance (Figure 3.10); an initial decrease of ohmic impedance followed by an increase towards EOL. The charge transfer impedance growth shows a more linear and monotonically increasing trend with

significant increase at EOL. In contrast, *Cycle M* results in a very moderate increase in both ohmic and charge transfer impedance.

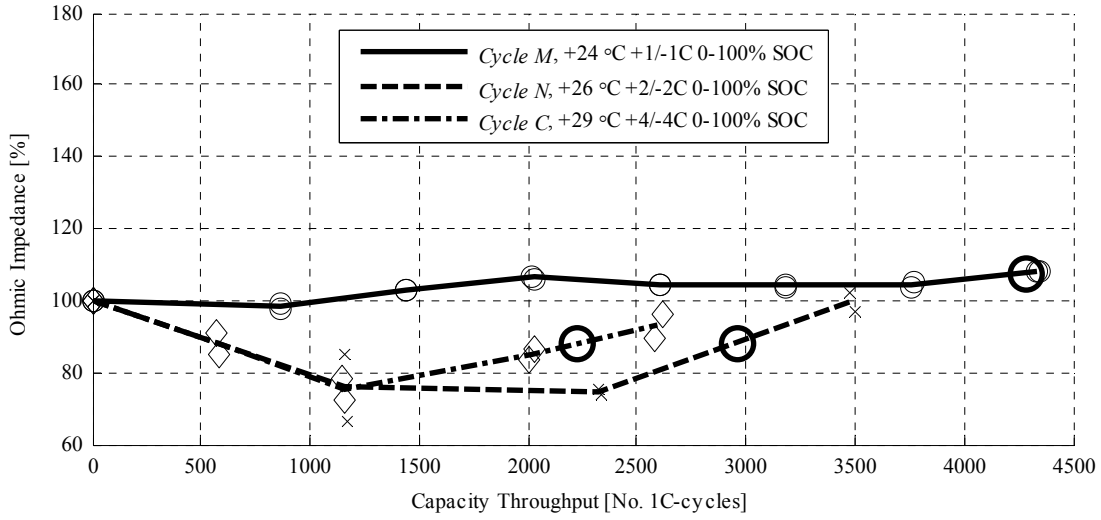

Figure 3.9 Normalised ohmic impedance for *Cycle M, N & C* at +24…+29 °C. Large circles: EOL; Other markers: measurements of individual cells; Lines: average.

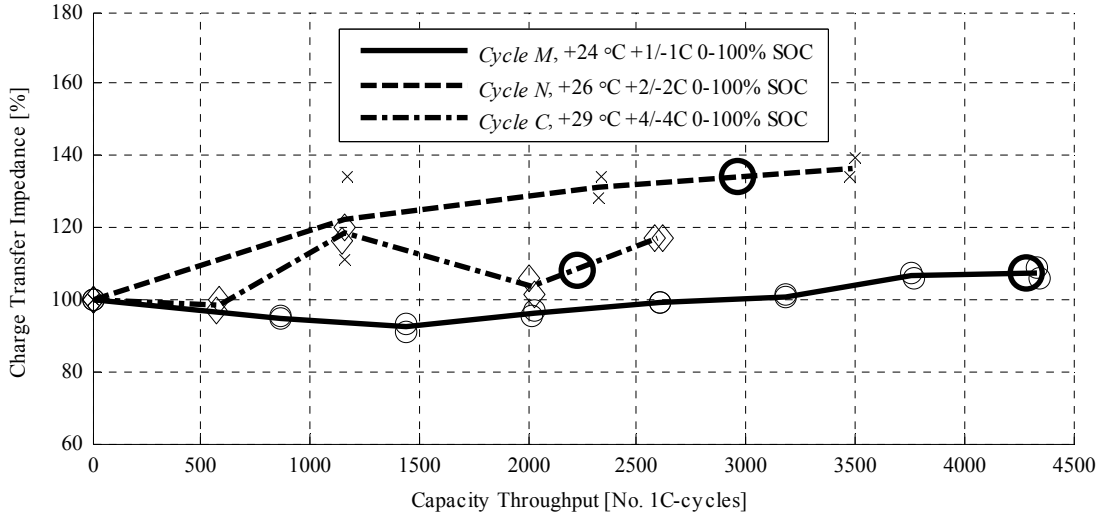

Figure 3.10 Normalised charge transfer impedance for *Cycle M, N & C* at +24…+29 °C. Large circles: EOL; Other markers: measurements of individual cells; Lines: average.

At medium to high temperatures only *Cycle N* shows an initial decrease of ohmic impedance and low growth at EOL (Figure 3.11). The increase in ohmic and charge transfer impedance (Figure 3.12) observed for *Cycle M* at +32 °C is almost identical to that of +24 °C. Another surprising observation is that for *Cycle N & C*, the ohmic impedance growth is higher at higher temperatures, but the opposite is seen for the charge transfer impedance.

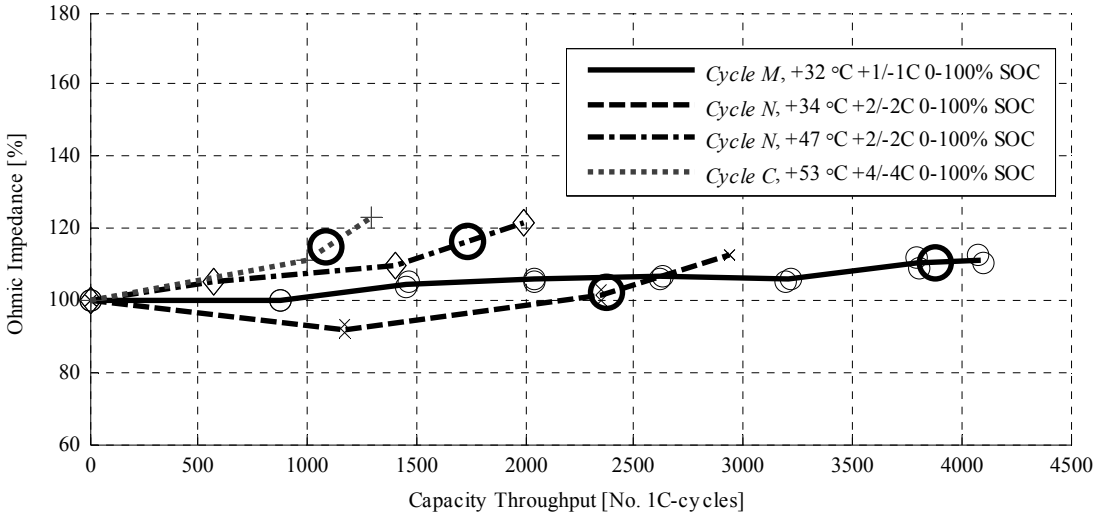

Figure 3.11 Normalised ohmic impedance for *Cycle M, N & C* at +32…+53 °C. Large circles: EOL; Other markers: measurements of individual cells; Lines: average.

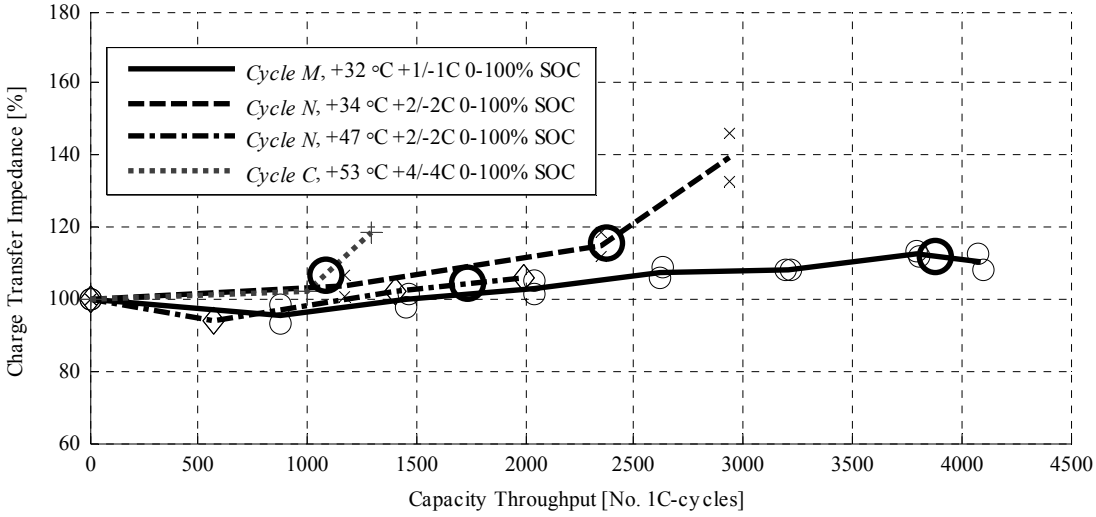

Figure 3.12 Normalised charge transfer impedance for *Cycle M, N & C* at +32…+53 °C. Large circles: EOL; Other markers: measurements of individual cells; Lines: average.

Despite the rapid capacity fade for *Cycle J* compared to *Cycle C*, the growth in ohmic (Figure 3.13) and charge transfer (Figure 3.14) impedance is similar except for at +35 °C where slightly higher charge transfer impedance is observed. Also, *Cycle J* at +27 °C results in an initial drop in charge transfer impedance not observed for higher temperatures or for *Cycle C*.

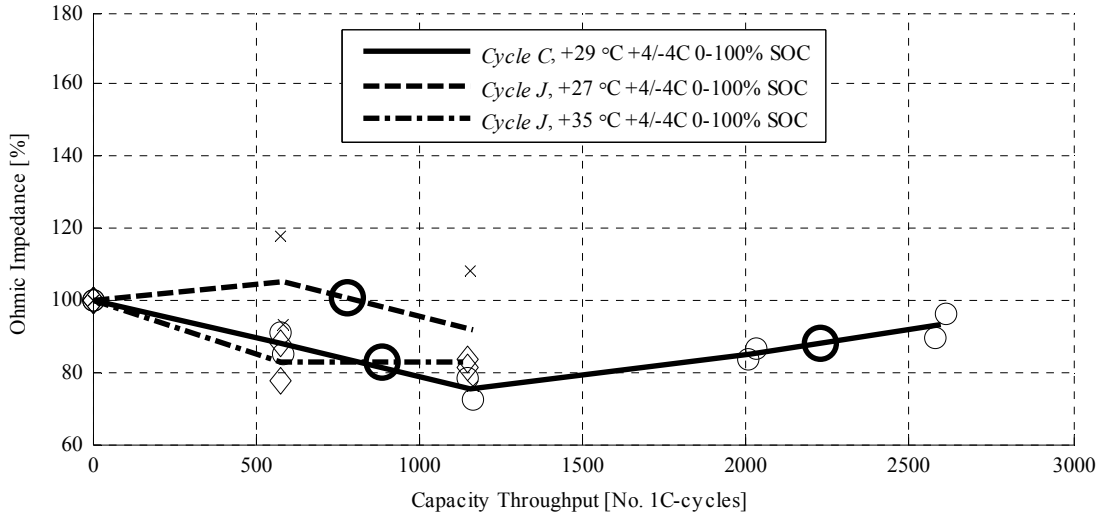

Figure 3.13 Normalised ohmic impedance for *Cycle J & C* at +27…+35 °C. Large circles: EOL; Other markers: measurements of individual cells; Lines: average.

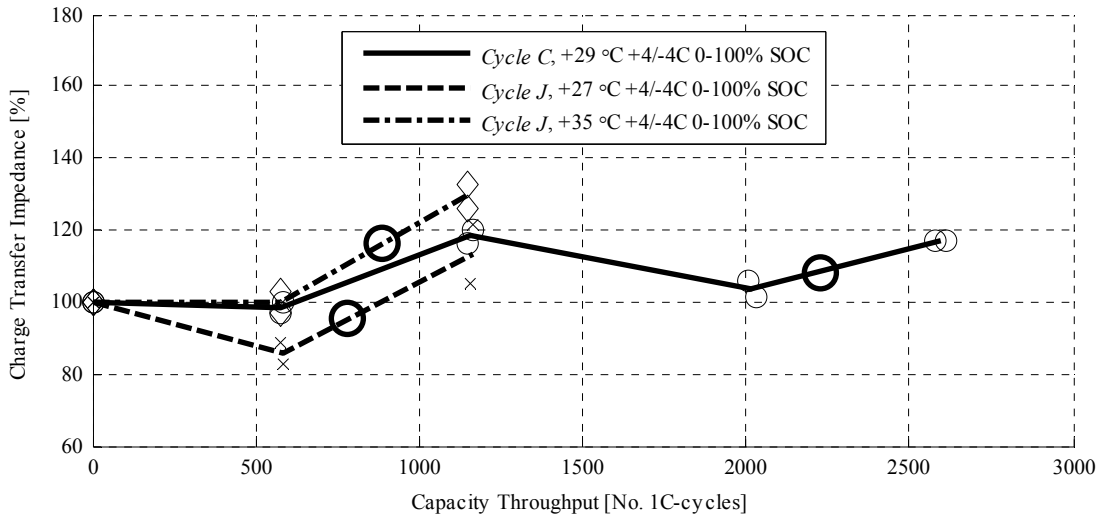

Figure 3.14 Normalised charge transfer impedance for *Cycle J & C* at +27…+35 °C. Large circles: EOL; Other markers: measurements of individual cells; Lines: average.

Cycle K, D & L show very different ageing patterns in terms of impedance growth, however similar to the differences in capacity fade. Whereas *Cycle K* yields a very large increase initially of both ohmic (Figure 3.15) and charge transfer impedance (Figure 3.16) followed by a linear growth, *Cycle D & L* show a much slower growth. In addition, *Cycle L* results in an initial decrease of charge transfer impedance. At EOL, only *Cycle K* shows significant growth.

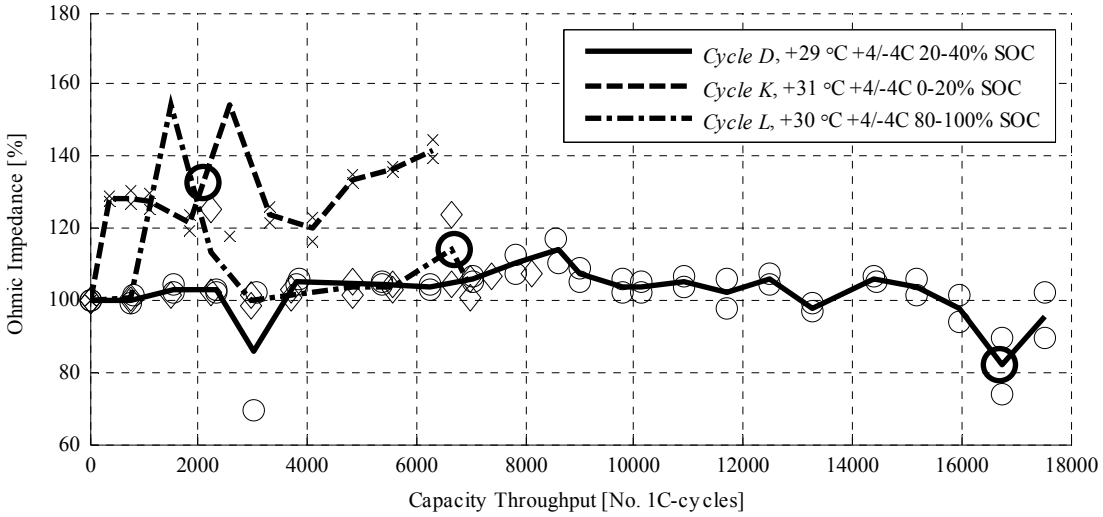

Figure 3.15 Normalised ohmic impedance for *Cycle D, K & L* at +29…+31 °C. Large circles: EOL; Other markers: measurements of individual cells; Lines: average.

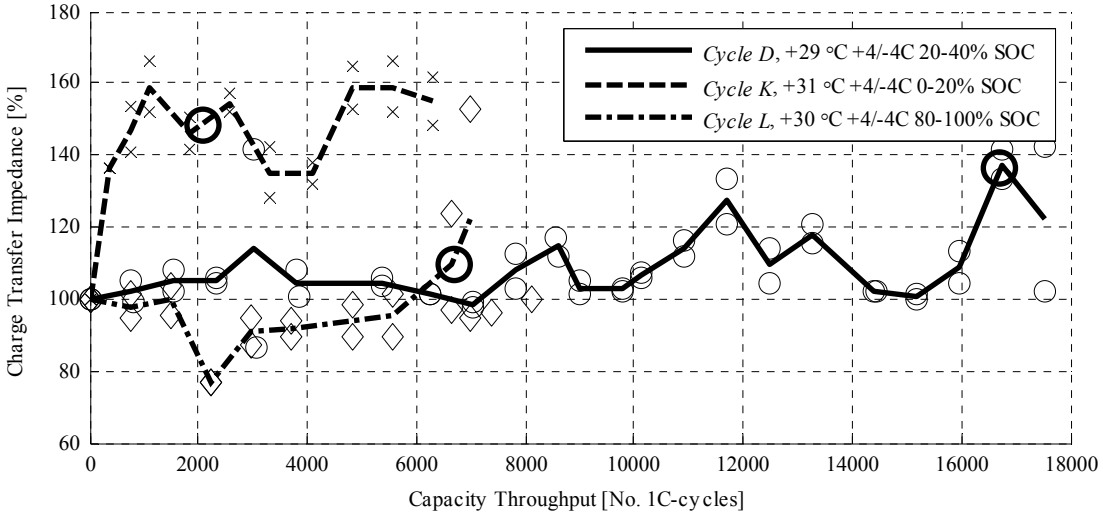

Figure 3.16 Normalised charge transfer impedance for *Cycle D, K & L* at +29…+31 °C. Large circles: EOL; Other markers: measurements of individual cells; Lines: average.

In terms of impedance growth *Cycle I, H & C* show very different trends for low (Figure 3.17 and Figure 3.18) to medium (Figure 3.19 and Figure 3.20) temperatures.

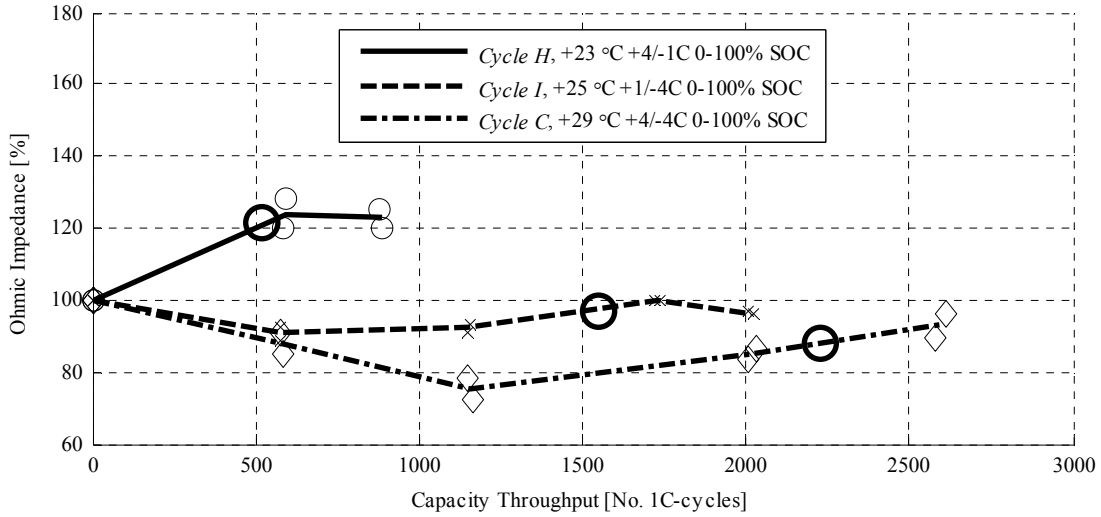

Figure 3.17 Normalised ohmic impedance for *Cycle H, I & C* at +23…+29 °C. Large circles: EOL; Other markers: measurements of individual cells; Lines: average.

Cycle I generally shows the least significant impedance growth and the behaviour of *Cycle H* can possibly be regarded as an acceleration of what can be seen for *Cycle C*.

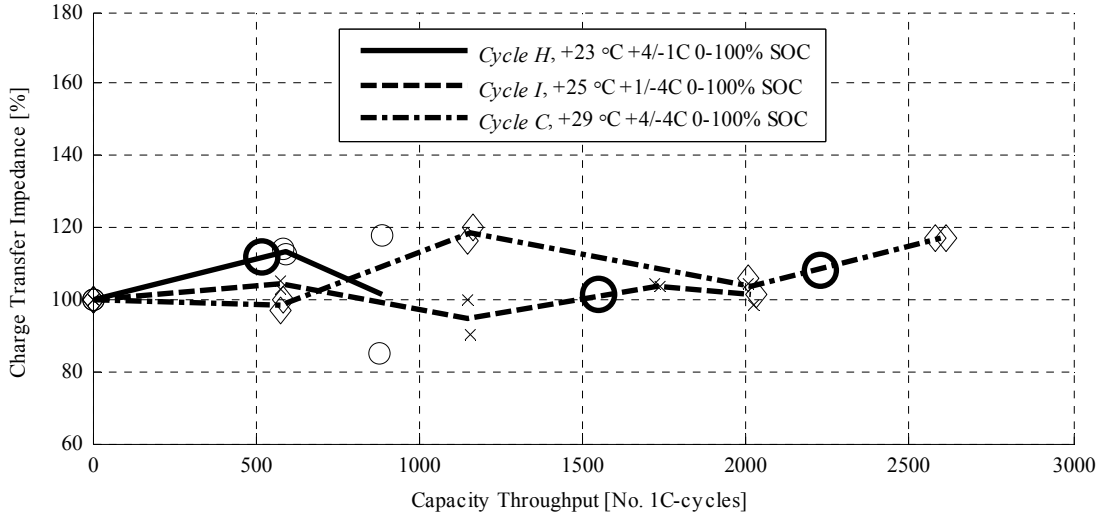

Figure 3.18 Normalised charge transfer impedance for *Cycle H, I & C* at +23…+29 °C. Large circles: EOL; Other markers: measurements of individual cells; Lines: average.

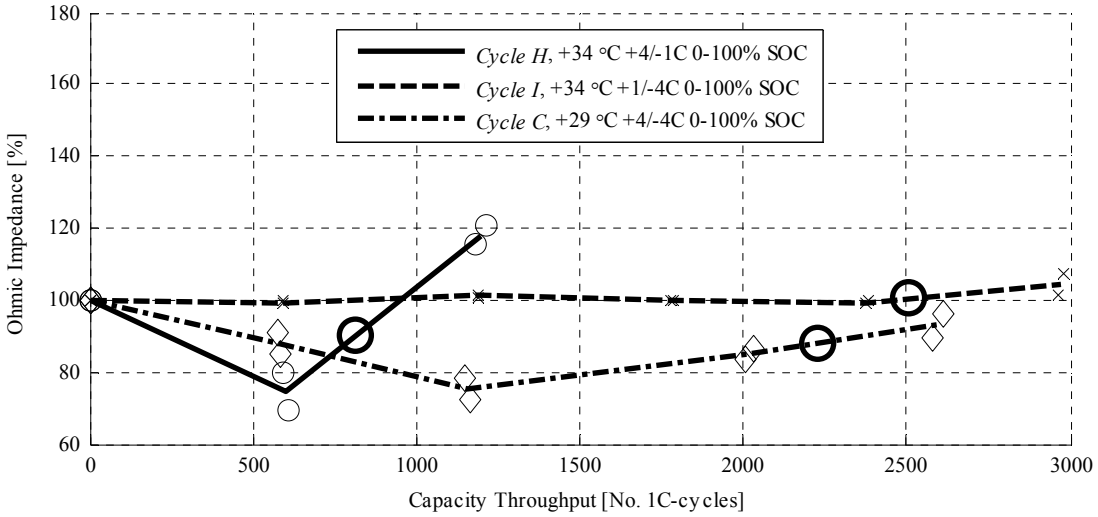

Figure 3.19 Normalised ohmic impedance for *Cycle H, I & C* at +29…+34 °C. Large circles: EOL; Other markers: measurements of individual cells; Lines: average.

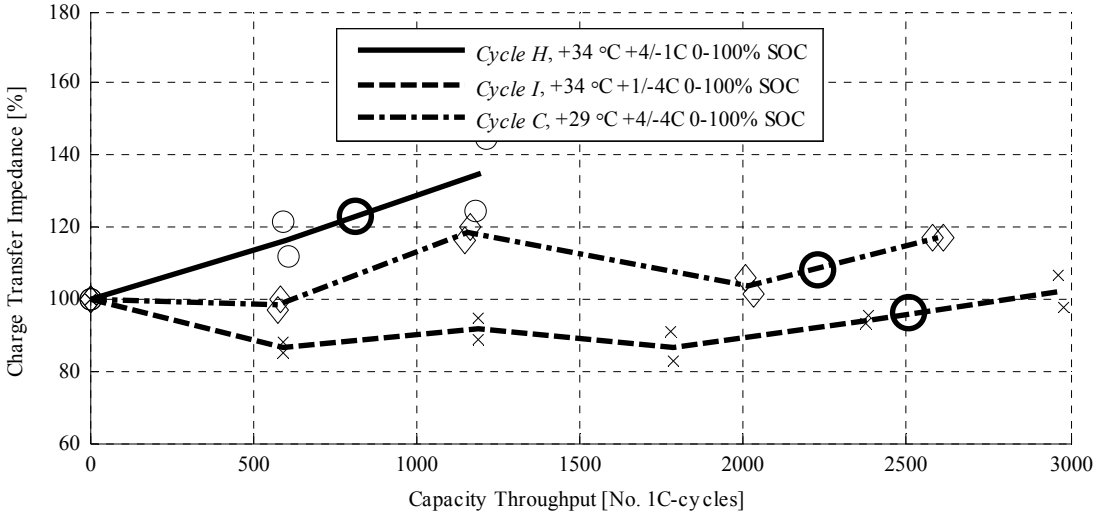

Figure 3.20 Normalised charge transfer impedance for *Cycle H, I & C* at +29…+34 °C. Large circles: EOL; Other markers: measurements of individual cells; Lines: average.

Furthermore, the differences between the trends are most apparent at low to medium temperatures, *i.e.* at high temperatures (Figure 3.21 and Figure 3.22) it is difficult to observe fundamentally different trends between the cycles except the average growth rate.

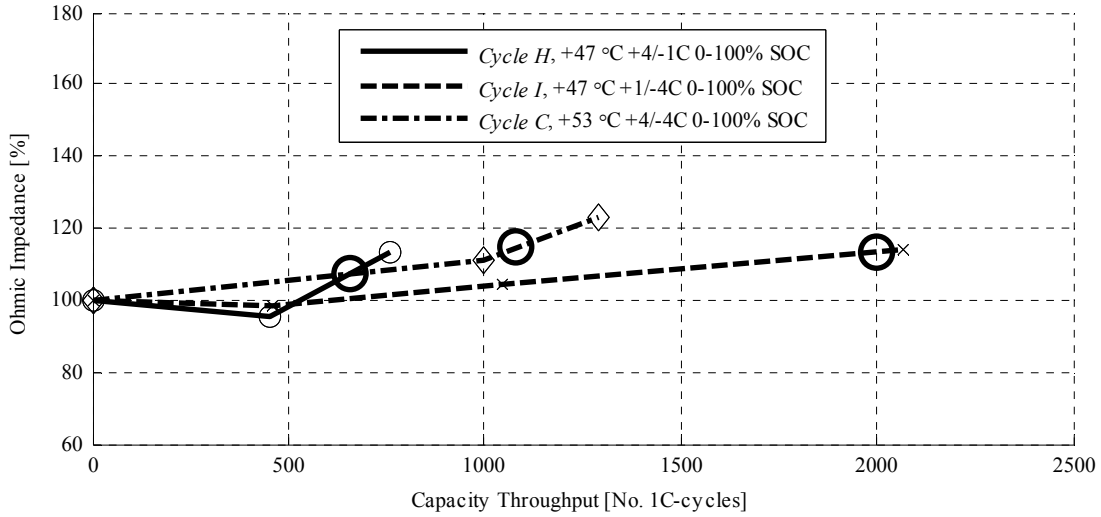

Figure 3.21 Normalised ohmic impedance for *Cycle H, I & C* at +47…+53 °C. Large circles: EOL; Other markers: measurements of individual cells; Lines: average.

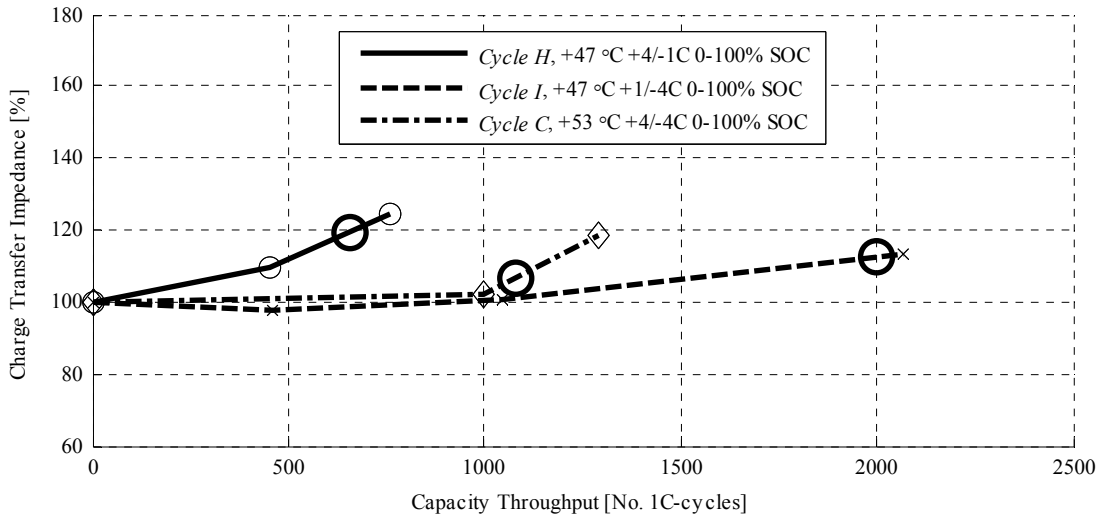

Figure 3.22 Normalised charge transfer impedance for *Cycle H, I & C* at +47…+53 °C. Large circles: EOL; Other markers: measurements of individual cells; Lines: average.

3.3 Calendar Ageing

High-power applications such as heavy-duty xEVs are normally used extensively with none or very short periods of rest. Consequently, the battery ageing is most likely caused by the cycling itself rather than storage / calendar ageing. Nevertheless, the calendar ageing must still be considered as a factor, at least in a general sense.

Two cells were stored at 30% SOC and +22 °C (here denoted *Cycle G*) for about 2.5 years with RPTs performed on a regular basis. The capacity fade (Figure 3.23) is

marginal and slow, less than 5% after two years of storage, indicating that the calendar ageing effect is marginal compared to all cycle life tests performed in the present work.

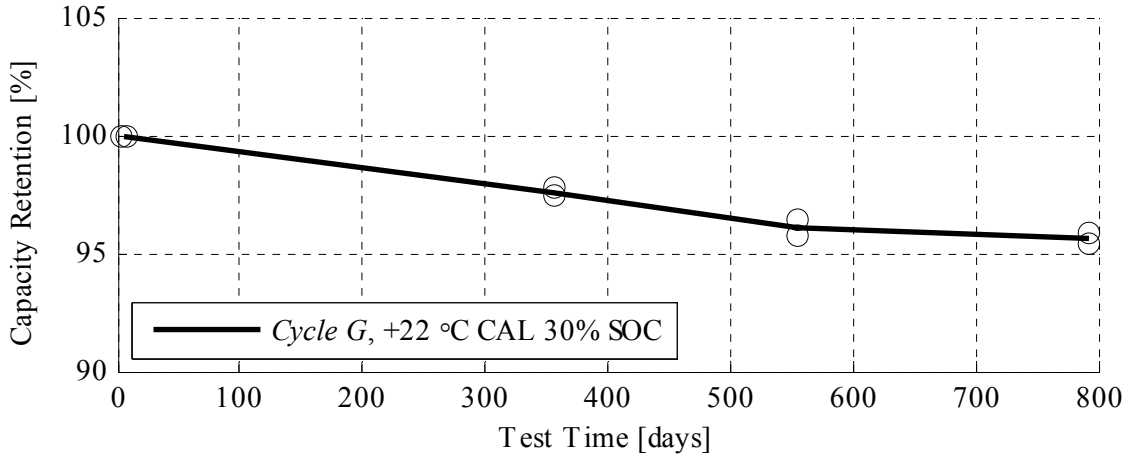

Figure 3.23 Capacity retention for calendar aged cells at +22 °C and 30% SOC. Markers indicate the measurements of individual cells and the lines indicate the average.

Interestingly, the ohmic impedance (Figure 3.24) and the charge transfer impedance (Figure 3.25) are actually decreasing for the calendar aged cells. It is very likely, however, that this decrease will be followed by an increase after further storage time, and such trend is also seen for the charge transfer impedance. It shall, however, be noted that the changes in impedance are small and therefore difficult to determine with certainty.

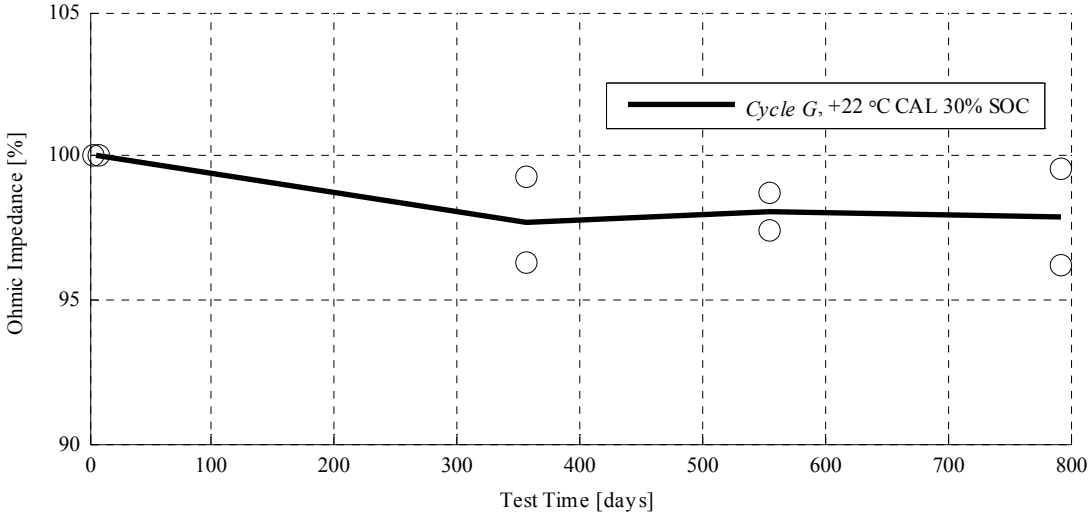

Figure 3.24 Normalised ohmic impedance of calendar aged cells at +22 °C and 30% SOC. Markers indicate the measurements of individual cells and the lines indicate the average.

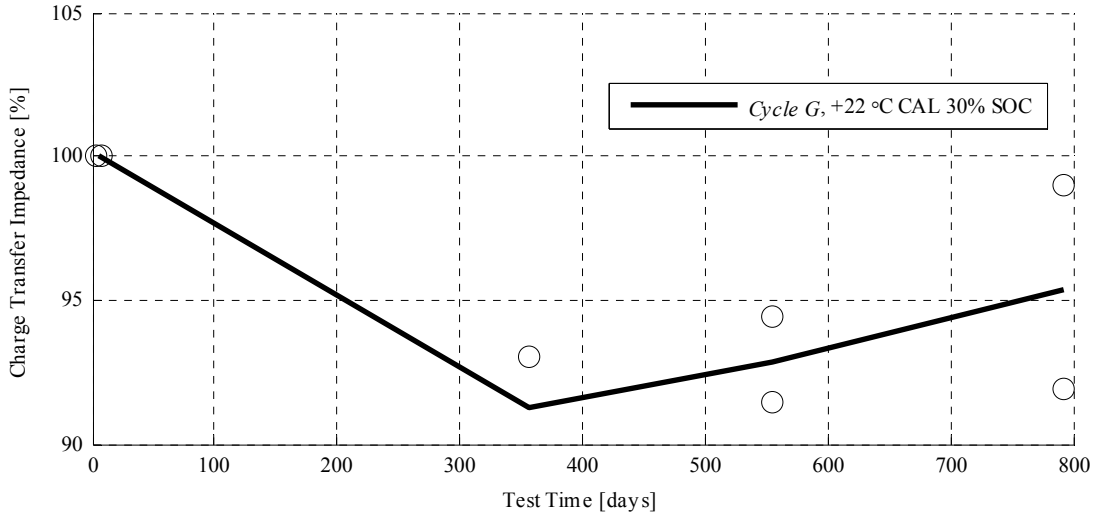

Figure 3.25 Normalised charge transfer impedance of calendar aged cells at +22 °C and 30% SOC. Markers indicate the measurements of individual cells and the lines indicate the average.

Chapter 4 Cell Degradation Analysis

As previously reviewed in Chapter 1, there are several ageing mechanisms that lead to a decrease in available cell capacity. Incremental capacity analysis (ICA) [43] and differential voltage analysis (DVA) [44]-[47] have successfully been demonstrated as valuable tools to quantify and distinguish between some of these mechanisms. These methods were also presented in previous work [1] together with a case study with simulated responses for some of the most important ageing mechanisms such as loss of cyclable lithium and loss of active electrode material.

This chapter presents a refined cell response model based on half-cells built from disassembled Li-ion cells after being aged, discussed in detail in *Paper IV*. Also, ICA profiles are presented to enable a qualitative analysis of the dominating ageing processes.

4.1 Identification of Capacity Fade Mechanisms

A simple half-cell model was used to simulate and estimate electrode capacities and loss of cyclable lithium corresponding to the observed ageing of the tested cells. Electrode parameters (Table 4) for this model was retrieved from [21] and measured half-cell voltages from the work behind *Paper IV* enabled a full-cell simulation and optimisation to fit the model to the performance of tested cells, thereby identifying capacity fade mechanisms.

Table 4 Electrode parameters for half/full cell model [21]

Component / property	Symbol	Value	Unit
Active material volume fraction, cathode	e_{sc}	0.374	-
Active material volume fraction, anode	e_{sa}	0.580	-
Electrode thickness, cathode	d_c	8.0e-5	m
Electrode thickness, anode	d_a	3.4e-5	m
Electrode area, cathode	A_c	1.8e-1	m^2
Electrode area, anode	A_a	1.8e-1	m^2
Maximum solid phase concentration, cathode	$CS_{max,c}$	22806	mol/m^3
Maximum solid phase concentration, anode	$CS_{max,a}$	30555	mol/m^3
Stoechimetry at 100% SOC, cathode	$\alpha_{c,100}$	1[1]	-
Stoechimetry at 100% SOC, anode	$\alpha_{a,100}$	0.7978[1]	-
Stoechimetry at 0% SOC, cathode	$\alpha_{c,0}$	0.2950[1]	-
Stoechimetry at 0% SOC, anode	$\alpha_{a,0}$	0[1]	-
Electrode capacity, cathode	Q_c	3.29[2]	Ah
Electrode capacity, anode	Q_a	2.91[2]	Ah
Cell capacity	$Q_{cell,c}$ / $Q_{cell,a}$	2.32[2]	Ah
Offset	Q_{offset}	0.97[2]	Ah

1. **Adjusted value to fit measured BOL voltage profile**
2. **Valid for a typical cell at BOL**

The initial electrode capacities are calculated using

$$Q_c = e_{sc} \cdot F \cdot d_c \cdot A_c \cdot CS_{max,c} \tag{4.1}$$

and

$$Q_a = e_{sa} \cdot F \cdot d_a \cdot A_a \cdot CS_{max,a} \tag{4.2}$$

with the available cell capacity according to

$$Q_{cell,c} = Q_c\left(\alpha_{c,100} - \alpha_{c,0}\right) \tag{4.3}$$

and

$$Q_{cell,a} = Q_a\left(\alpha_{a,100} - \alpha_{a,0}\right) \tag{4.4}$$

Subsequently, the electrode mismatch offset is calculated using

$$Q_{offset} = Q_c \cdot \alpha_{c,0} = Q_c - Q_{cell,c} \tag{4.5}$$

Based on these simple relations the characteristic voltage profile for a full cell with any combination of electrode capacities and loss of lithium can be simulated by adjusting the three parameters Q_c, Q_a and Q_{offset}, and the use of look-up tables V_c and V_a for the cathode and anode potential *vs.* Li/Li$^+$ respectively, according to

$$U_{cell} = V_c\left(SOC_{cell,c}, I\right) - V_a\left(SOC_{cell,a}, I\right) + U_{drop} \tag{4.6}$$

where U_{drop} is added to compensate for small changes in cell impedance. V_c and V_a are derived from half-cell measurements on electrodes from disassembled cells.

Then, depending on the sign of Q_{offset} the two different sets of relations

$$\left.\begin{aligned} Q_{cell} &= Q_{cell,c} - Q_{offset} \\ SOC_{cell,c} &= \left(SOC_c - Q_{offset}/Q_c\right) \cdot Q_c/Q_{cell} \\ SOC_{cell,a} &= SOC_a \cdot Q_a/Q_{cell} \end{aligned}\right\} Q_{offset} > 0 \tag{4.7}$$

and

$$\left.\begin{aligned} Q_{cell} &= Q_{cell,c} \\ SOC_{cell,c} &= SOC_c \cdot Q_c/Q_{cell} \\ SOC_{cell,a} &= \left(SOC_a + Q_{offset}/Q_a\right) \cdot Q_a/Q_{cell} \end{aligned}\right\} Q_{offset} < 0 \tag{4.8}$$

are used to calculate the SOC ranges of the electrodes for the resulting cell SOC as a function of the three variables Q_{offset}, Q_c and Q_a.

This simulation will however only be valid for full charge / discharge cycles at comparably low current rates since the electrochemical reactions are not taken into consideration.

Figure 4.1 shows the typical cell voltage profile at BOL and the corresponding half-cell potentials for the graphite anode and the $LiFePO_4$ cathode as a function of capacity. This typical case is valid for the cell studied in the present work and is calculated using the electrode data presented in Table 4 and equations (4.1) to (4.8).

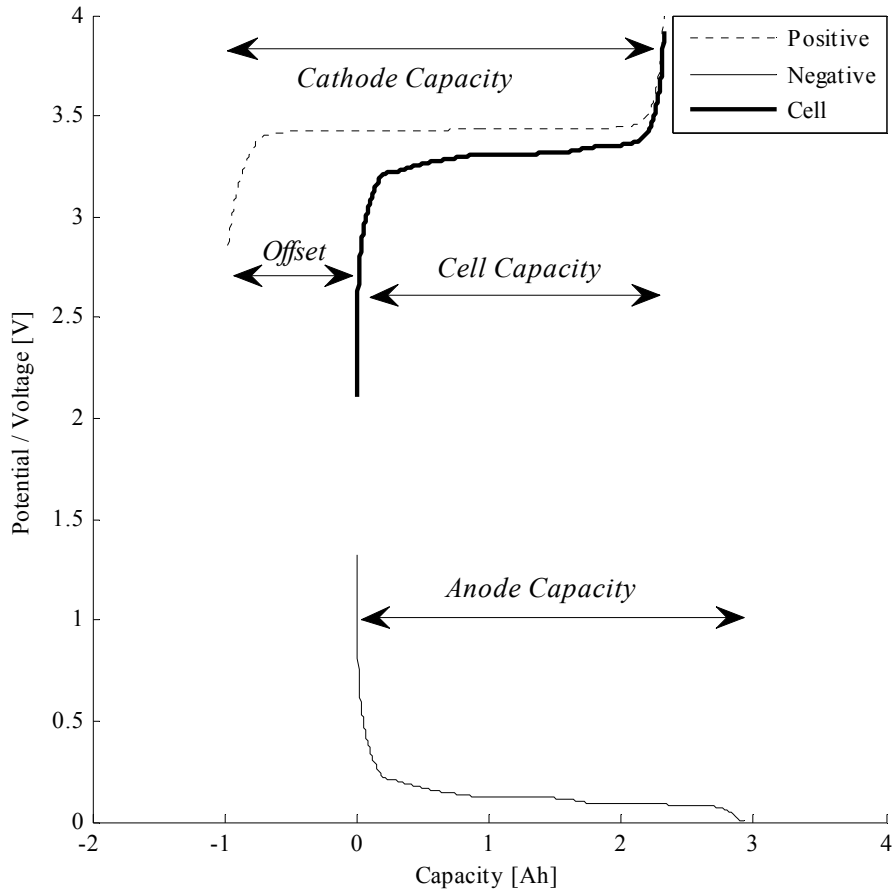

Figure 4.1 Cell capacity and cell potential *vs.* SOC together with half-cell potential profiles

Here, both electrodes have a capacity of approx. 3Ah and the irreversible capacity loss Q_{offset} due to initial SEI-formation is roughly 1Ah denoted as "*Offset*" in the figure.

Generally, (see Section 1.1), the capacity fade mechanisms can be categorised into two different groups: loss of cyclable lithium and loss of active electrode capacity, where the latter can be divided into four sub groups depending on electrode and charge state. Each of these five groups is presented with simulated cell response in the following Section 4.1.1 and 4.1.2.

4.1.1 Loss of Cyclable Lithium

Typically, loss of cyclable lithium is caused by parasitic reactions such as surface film formation, primarily on the anode. Regardless of the dominating reaction, any Li-ion that is released from electrode to the electrolyte but not reversibly inserted into the opposing electrode will lead to an increase in the electrode offset Q_{offset}, with no change in Q_a or Q_c, as shown in Figure 4.2.

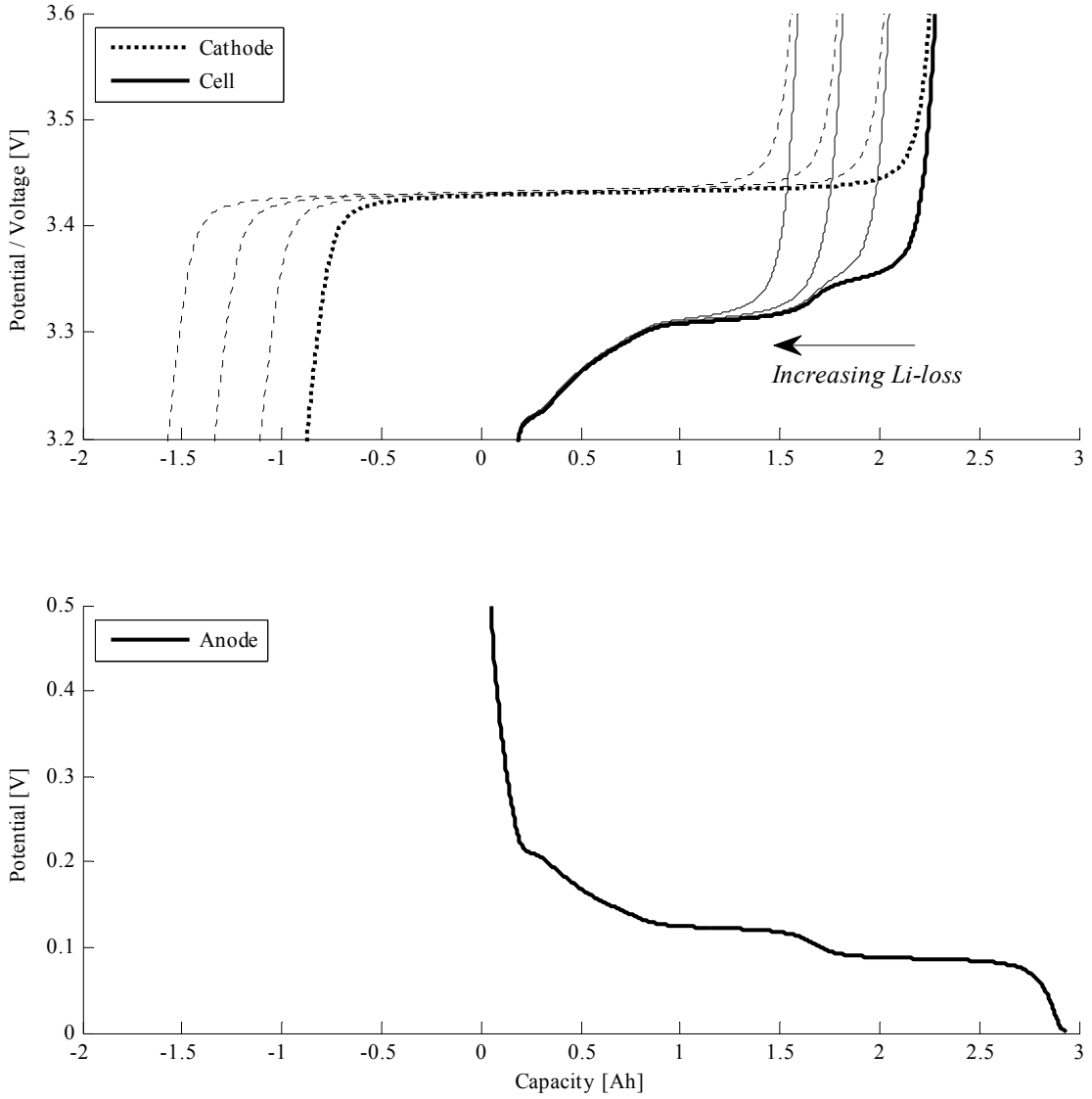

Figure 4.2 Simulated [0:10:30]% loss of cyclable lithium in addition to initial loss

At a cell level an increasing loss of cyclable lithium can be observed as a shortening, or disappearing, of the last voltage plateau in the cell voltage profile close to SOC 100%.

4.1.2 Loss of Active Electrode Area

Loss of active electrode area or mass may be caused by a large number of reactions, either by reducing the apparent electrode / electrolyte interface, by electrically isolating

electrode particles or by consuming electrode particles in unwanted reactions. Depending on the electrode charge level and the current direction these reactions result in different changes in active electrode material Q_a and Q_c and the offset Q_{offset}.

Loss of active anode material, from 100% SOC ($LAAM_{100}$)

Since the cathode generally limits cell capacity at high SOC (100% $FePO_4$), $LAAM_{100}$ will not affect available cell capacity until the total anode capacity is lower than the cell capacity. In such severe cases lithium plating may occur at cell SOC close to 100%, as is shown in Figure 4.3 where a 30% loss of anode material results in a new cell voltage plateau at about 3.4V corresponding to the difference between $LiFePO_4/FePO_4$ and Li/Li^+. Loss of anode material and lithium plating are generally comparably straightforward to detect using ICA or DVA.

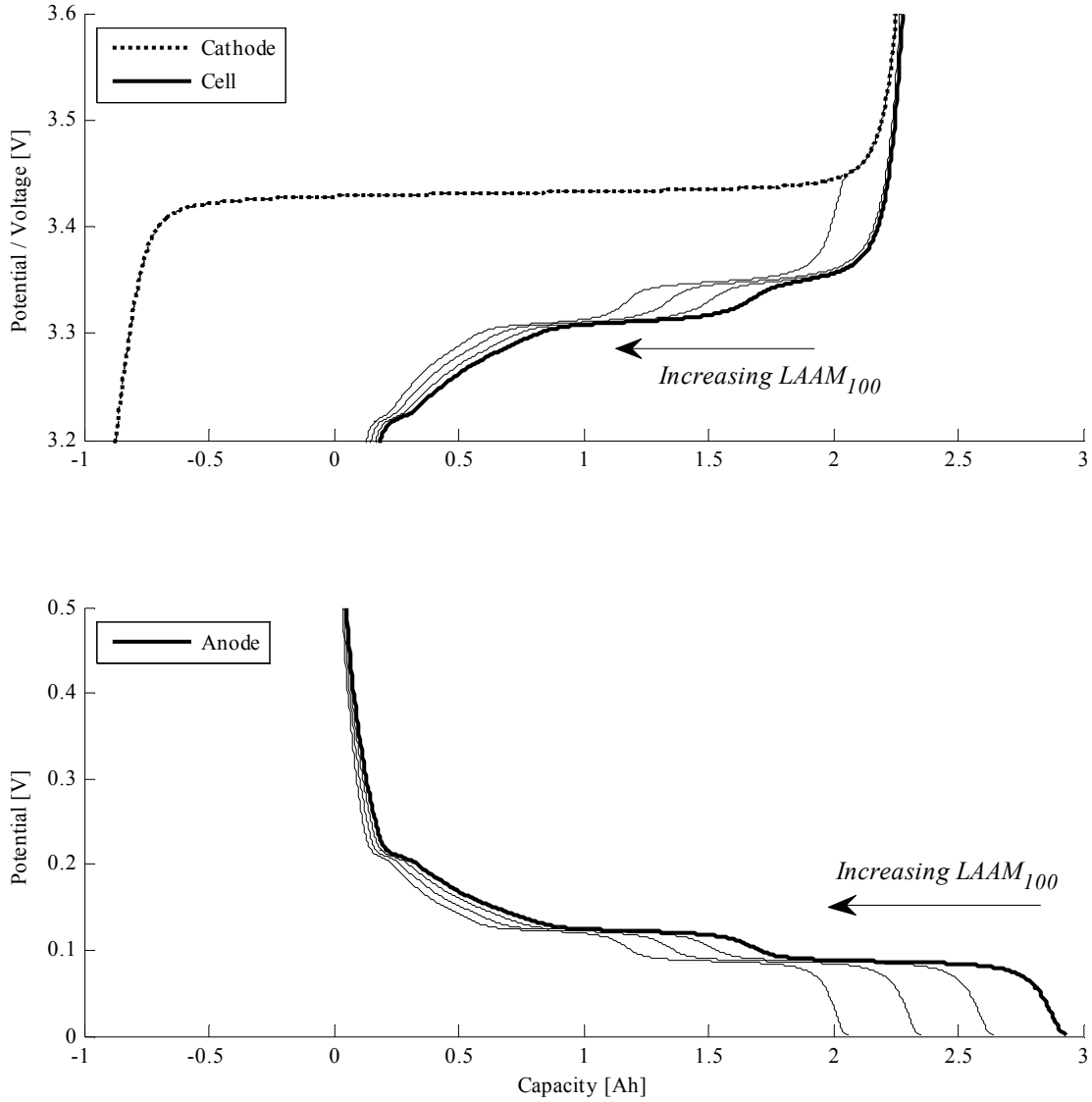

Figure 4.3 Simulated [0:10:30]% loss of active anode material from cell 100% SOC, $LAAM_{100}$

Loss of active anode material, from 0% SOC ($LAAM_0$)

When anode capacity is lost with reference to cell SOC 0% (fully de-lithiated graphite), the effect on cell capacity is pronounced and direct and will also increase the anode/cathode mismatch offset (Figure 4.4).

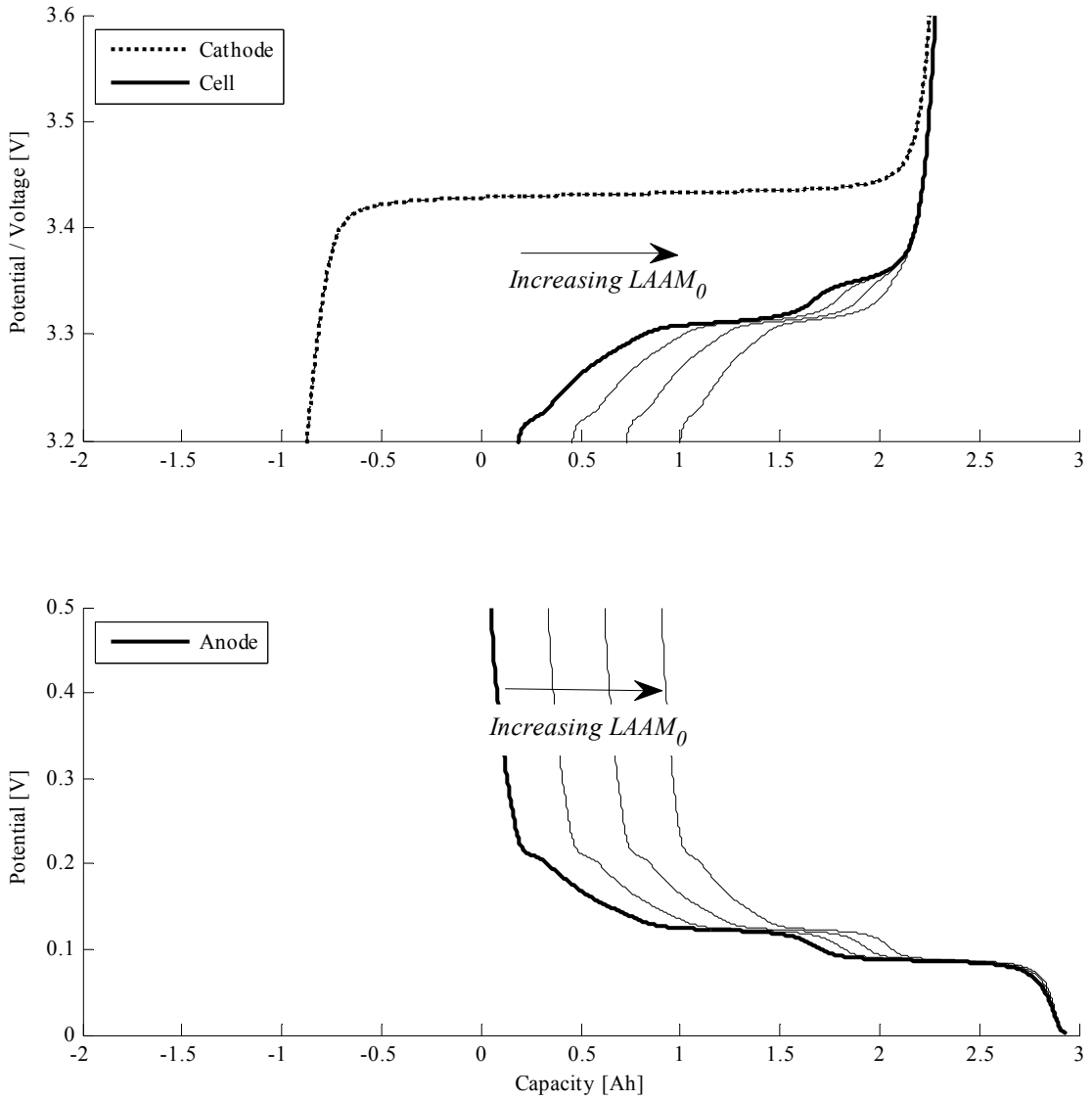

Figure 4.4 Simulated [0:10:30]% loss of active anode material from cell 0% SOC, $LAAM_0$

Loss of active cathode material, from 100% SOC ($LACM_{100}$)

Likewise to $LAAM_0$, loss of cathode material from cell SOC 100% will immediately cause cell capacity fade, but without affecting the electrode offset (Figure 4.5). In some cases $LACM_{100}$ is possible to detect using ICA or DVA, but since its signature is very similar to that of Li-loss (Figure 4.2) it is not straightforward and may also be complicated by an associated increase in cell impedance.

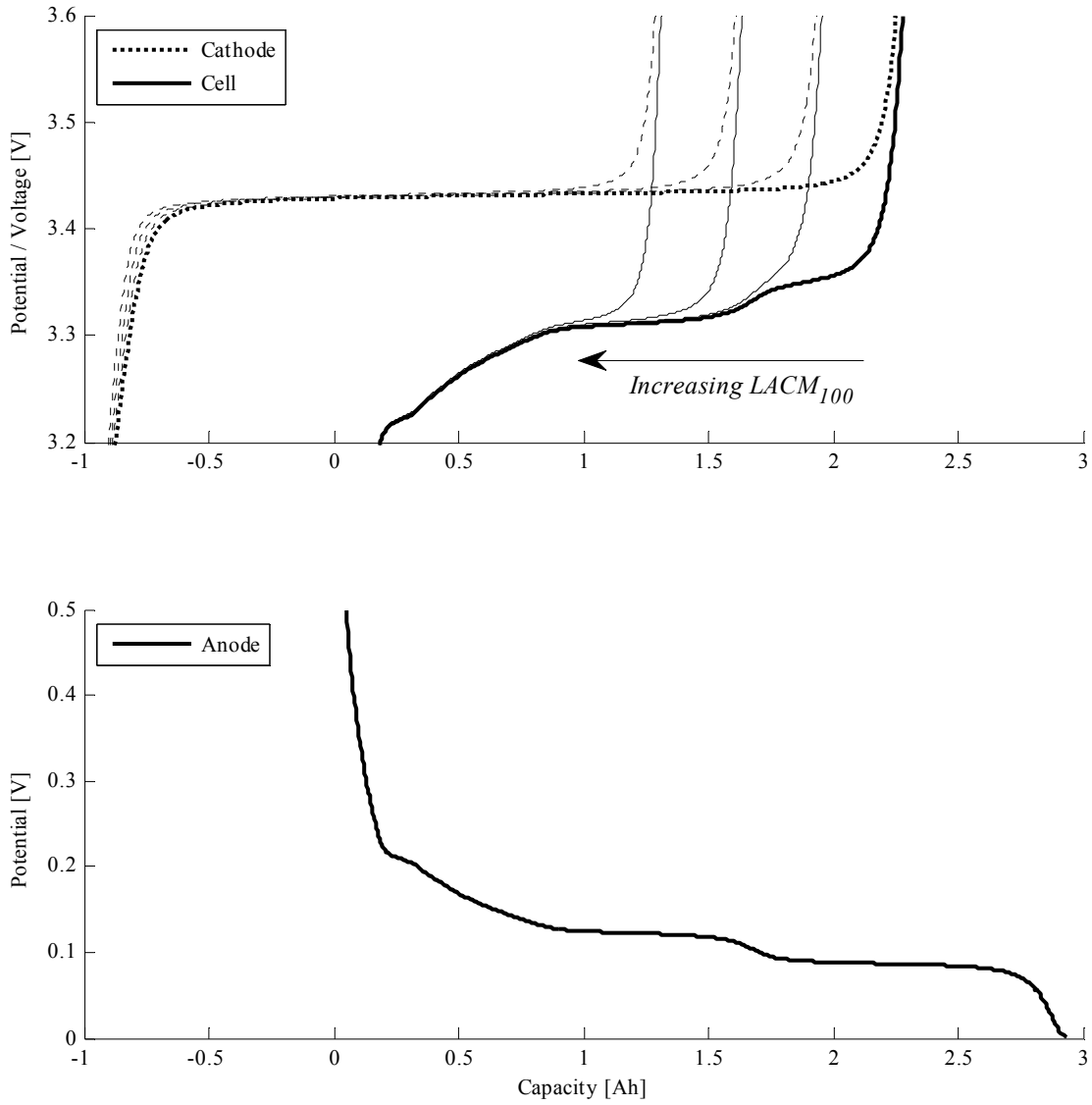

Figure 4.5 Simulated [0:10:30]% loss of active cathode material from cell 100% SOC, $LACM_{100}$

Loss of active cathode material, from 0% SOC ($LACM_0$)

The anode normally limits the cell capacity as the anode potential rises quickly towards the fully de-lithiated state. Hence, a loss of cathode material in this region will not limit cell capacity until the cathode capacity is lower than the initial cell capacity, analogously to the case of $LAAM_{100}$. As can be seen in Figure 4.6, the signature of $LACM_{100}$ in cell voltage is not pronounced unless for severe cases.

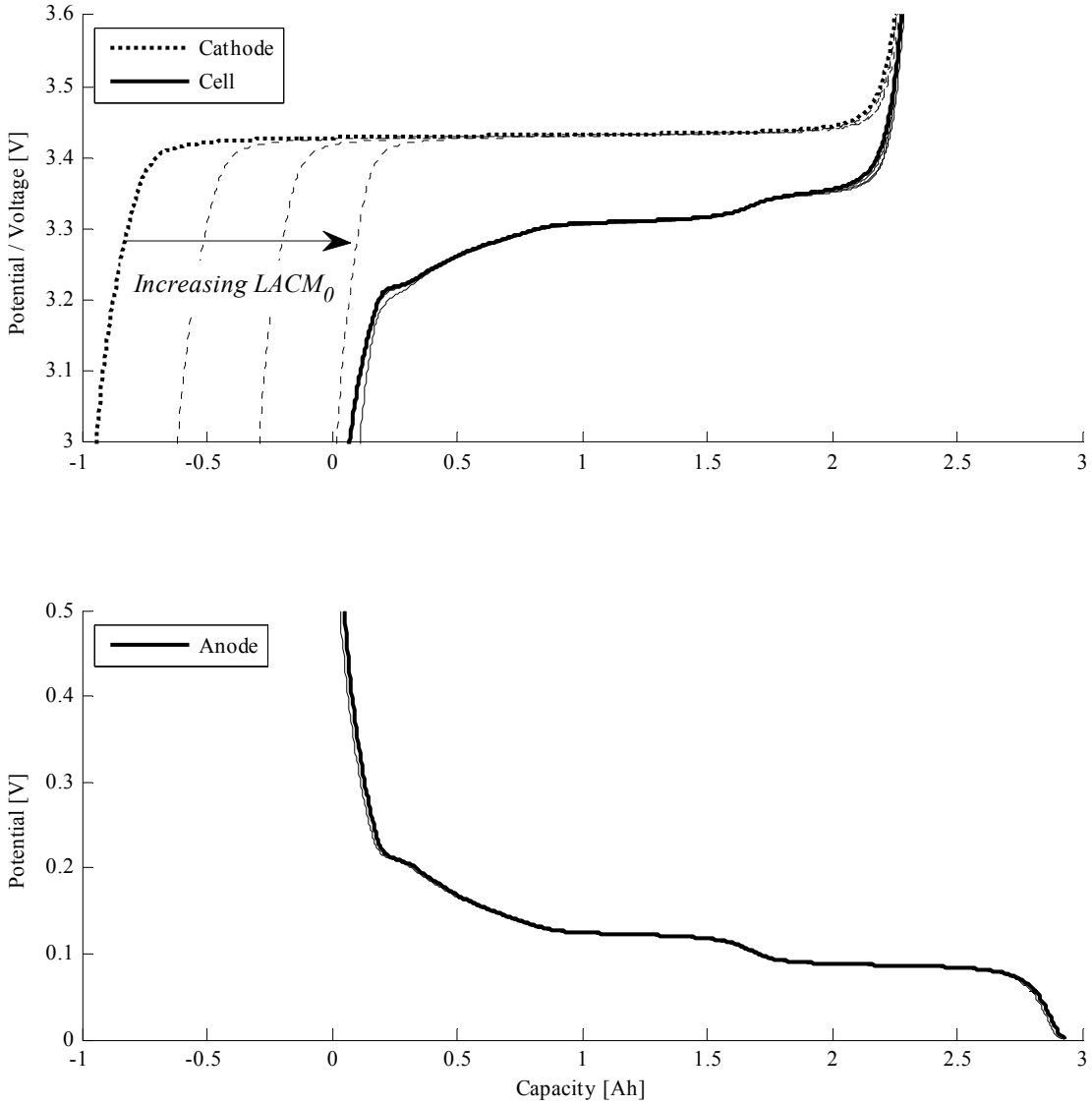

Figure 4.6 Simulated [0:10:30]% loss of active cathode material from cell 100% SOC, $LACM_0$

In summary, loss of cyclable lithium and $LAAM_0$ always lead to loss of cell capacity and an increase in Q_{offset}. In contrast, $LAAM_{100}$ and $LACM_{100}$ do not affect Q_{offset}, and where $LACM_{100}$ immediately leads to capacity loss, $LAAM_{100}$ will only affect cell capacity in severe cases. Lastly, $LACM_0$ only leads to capacity fade in severe cases but will always lead to a decrease in Q_{offset}. The above summary can be used as a qualitative analysis tool when analysing cell voltage profiles. However, $LACM_0$ has very small

effect on the cell voltage profile and $LACM_{100}$ may be difficult to distinguish from loss of lithium, hence cathode ageing is generally challenging to characterise without the use of very low current rates or by performing a *post mortem* analysis similar to what was done in *Paper IV*.

4.2 Characterisation of Capacity Fade

In the previous section a method for simulating various types of capacity fade was presented. This method, together with the use of ICA and DVA, was applied for all tested cells to enable a mapping of ageing modes to the load cycle conditions. Despite the application of C/10 charge and discharge cycles to obtain a detailed cell response, the aforementioned difficulties to distinguish between especially loss of cathode material and cyclable lithium forced a number of assumptions to be made:

- $LAAM_{100}$ was assumed to dominate the anode fading as indicated by previous work [9] and the confirmed occurrence of lithium plating for some cases.
- The cathode loss was not separated from loss of cyclable lithium. Instead, Q_{offset} and Q_a are used to characterise ageing with a fixed cathode capacity of 3Ah. This assumption is supported by the *post mortem* studies in *Paper IV* where no signs of significant loss of active cathode material were found.

These assumptions enabled a quantitative estimation of anode capacity for each RPT and test case. A few examples, showing the retention of cell capacity and estimated anode capacity *vs.* capacity throughput, are presented in Figure 4.7-Figure 4.9.

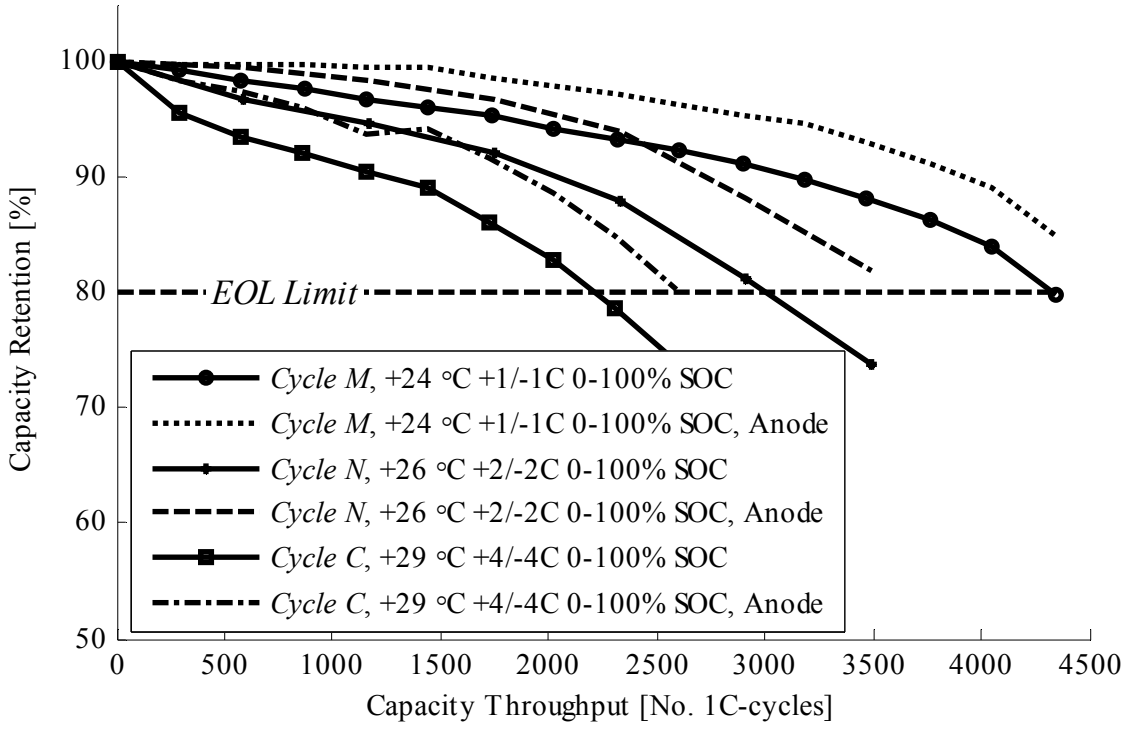

Figure 4.7 Retention of cell and anode capacity for *Cycle M, N & C* at temperatures below +30 °C

In contrast, *Cycle K* shows dramatic loss of anode capacity as can be seen in Figure 4.8 where this loss is compared to *Cycle D* & *L*.

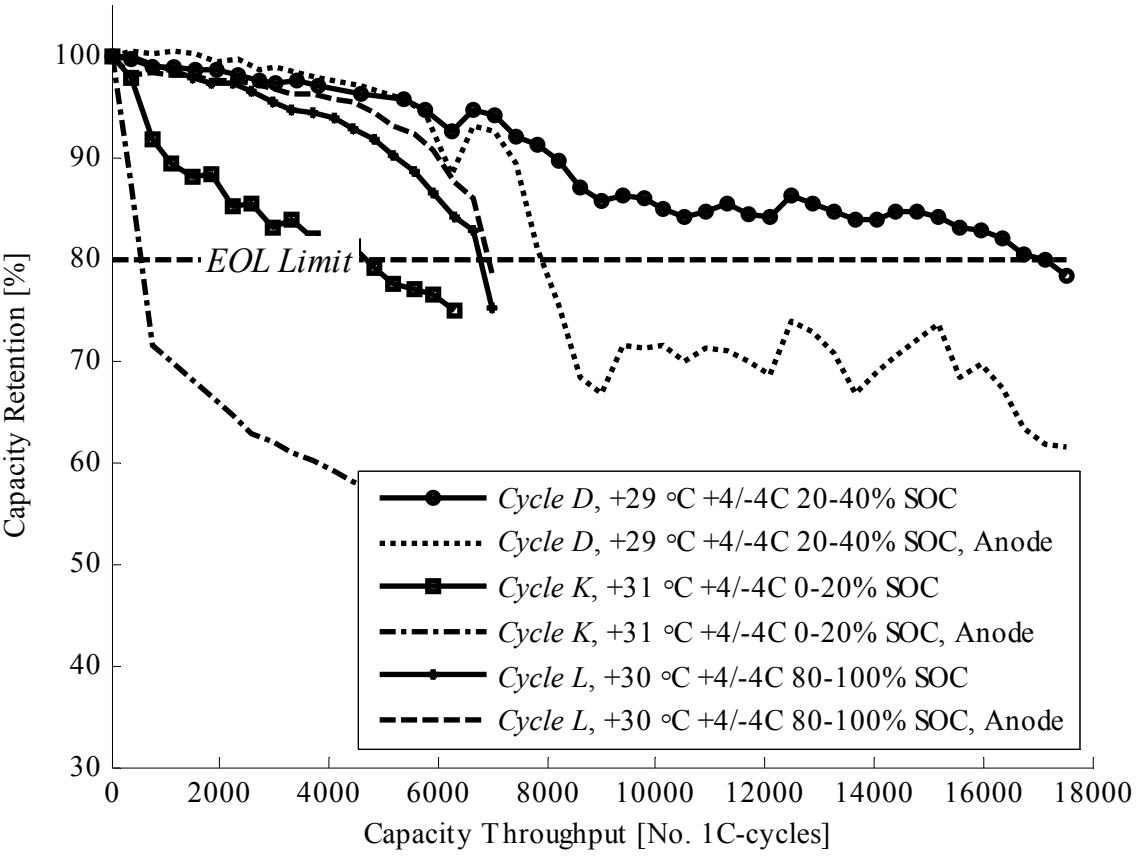

Figure 4.8 Retention of cell and anode capacity for *Cycle D, K* & *L* at temperatures below +31 °C

Likewise, there is a significant difference between *Cycle H*, *I* & *C* in terms of LAAM (Figure 4.9); whereas *Cycle C* and *I* show a slow degradation of the anode until the end of the cycle life test, *Cycle H* degrades the anode quicker than the cell capacity on a normalised scale.

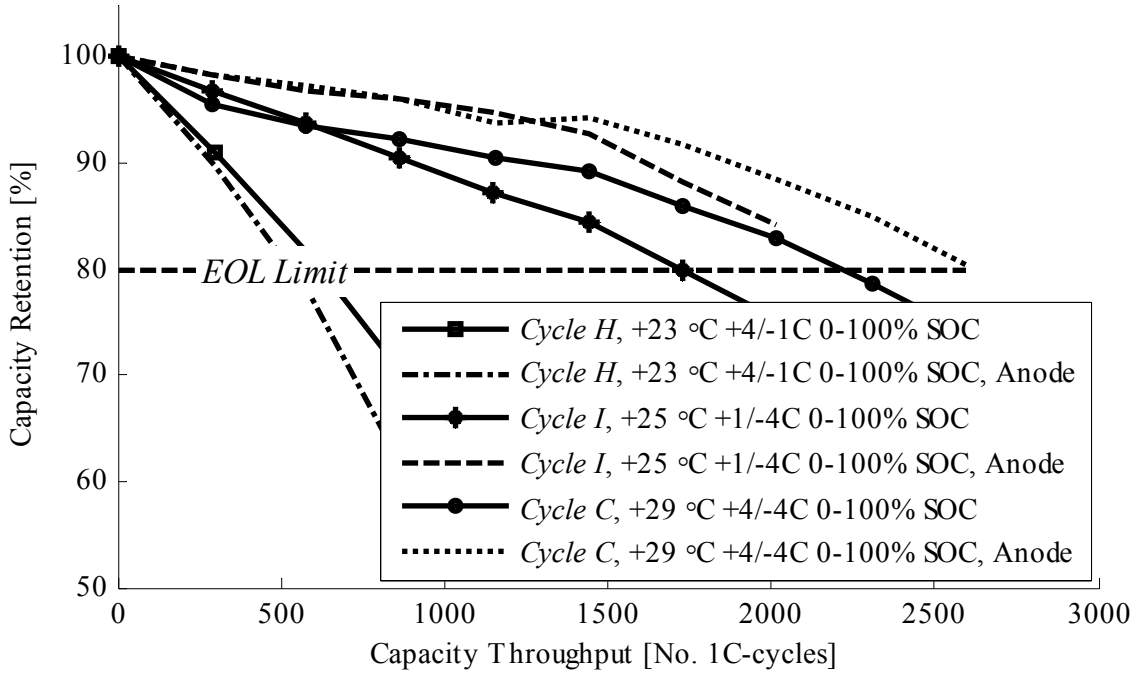

Figure 4.9 Retention of cell and anode capacity for *Cycle H, I* & *C* at temperatures below +30 °C

A selection of the results for all cycles is presented in Figure 4.10 for two middle-of-life (MOL) values (1/3 and 2/3 of EOL cycles) and EOL. Further details, such as measured and simulated voltage profiles as well as measured ICA, are given for some test cases in Section 4.2.1.

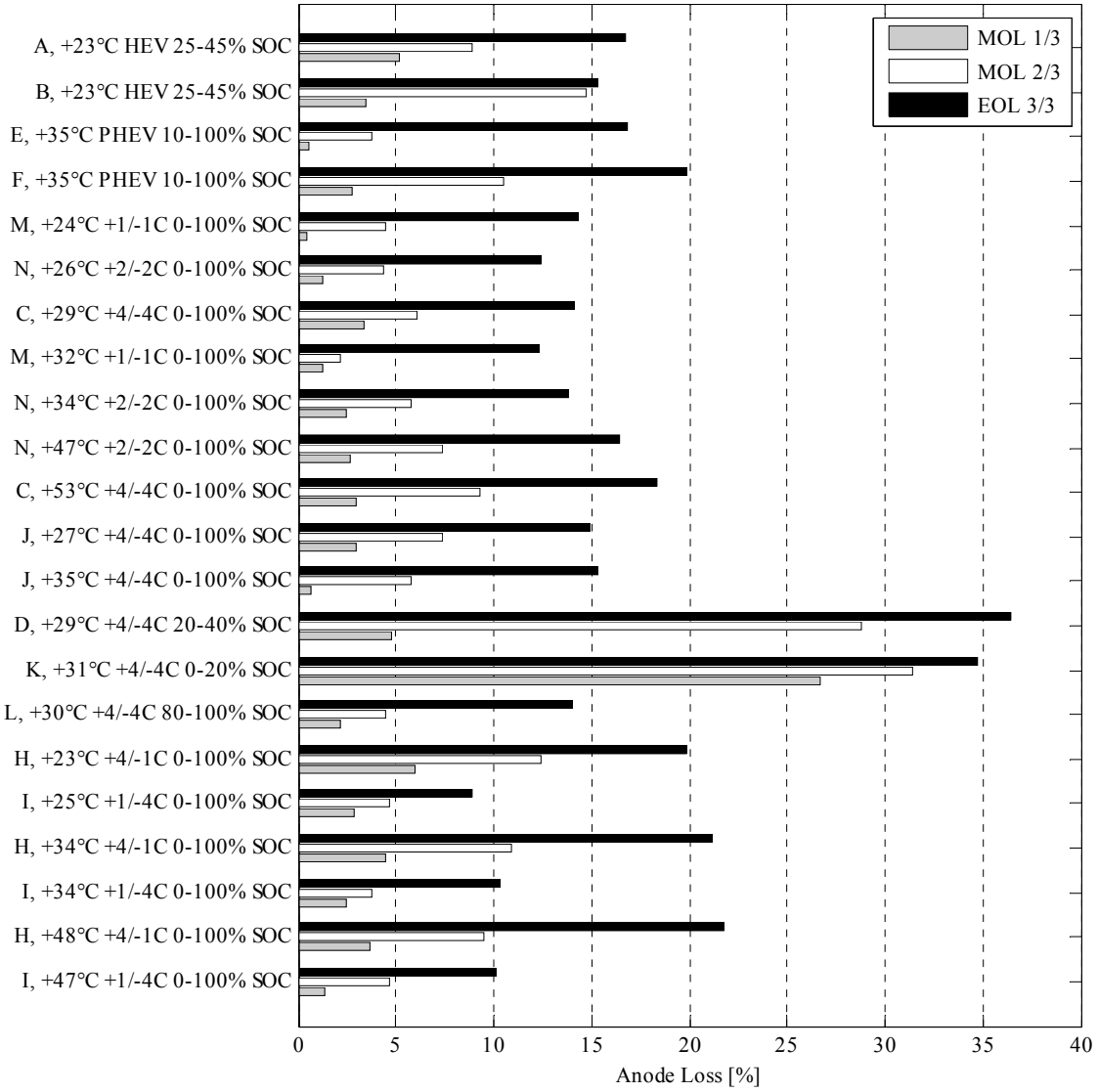

Figure 4.10 Estimated anode loss at MOL and EOL

Generally, all test cases show a marginal loss of anode capacity at MOL 1/3 except *Cycle K* that causes more anode loss at MOL 1/3 than most other cases show at EOL. In addition, the anode loss at EOL is higher than for all other test cases except *Cycle D*.

However, the anode loss observed for *Cycle D* may be caused by an undesired, and temporary, cycling at low SOC at approx. 50% of the EOL cycles (see Figure 4.11). Hence, the anode loss at MOL 2/3 and EOL for *Cycle D* would most probably be significantly lower if cycled with a better SOC control.

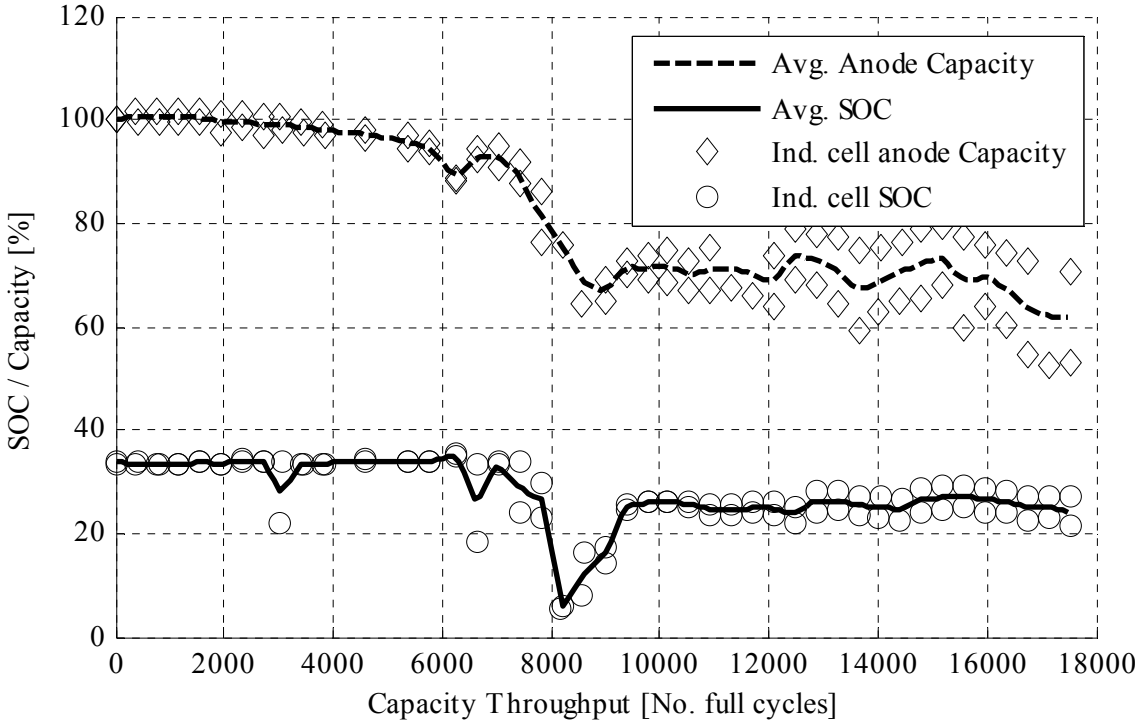

Figure 4.11 Average SOC and anode capacity for *Cycle D*

HEV Cycle A and *HEV Cycle B* show similar anode ageing figures as *Cycle C*, but there is a notable difference between the two; *Cycle B* causes a more substantial loss of anode material at MOL 2/3. Likewise, the *PHEV Cycle F* also shows a higher anode loss throughout the test than the similar *PHEV Cycle E*.

Moreover, all test cases show an acceleration of anode loss towards EOL. Yet, the anode loss at EOL is lower or equal to the total capacity loss (20%) for most cases, *i.e.* although the anode may affect the cell capacity, it is not limiting factor if $LAAM_{100}$ is assumed to dominate the anode ageing. Here, *Cycle D & K* represent exceptions with very high anode loss at EOL, indicating that Li-plating is likely to occur as the cell capacity is larger than the anode capacity. This was confirmed by the voltage profiles and the ICA/DVA signatures. There is also a small, but notable, correlation between anode loss and temperature for symmetric cycles.

In summary, the key ageing factors related to loss of both anode material and cyclable lithium seem to be operation at SOC below 30%, with high charging currents and at high temperatures.

4.2.1 Voltage & ICA Profiles

Cycle M, N, C and the calendar aged cells (*Cycle G*) all show similar ICA profiles at BOL and EOL (Figure 4.12). First and foremost the second capacity peak around 3.37 V for charge and 3.33 V for discharge is reduced, indicating loss of cyclable lithium as primary ageing mechanism. There is, however, also a reduction of other peaks, especially for *Cycle N & C*, also pointing at loss of active anode material.

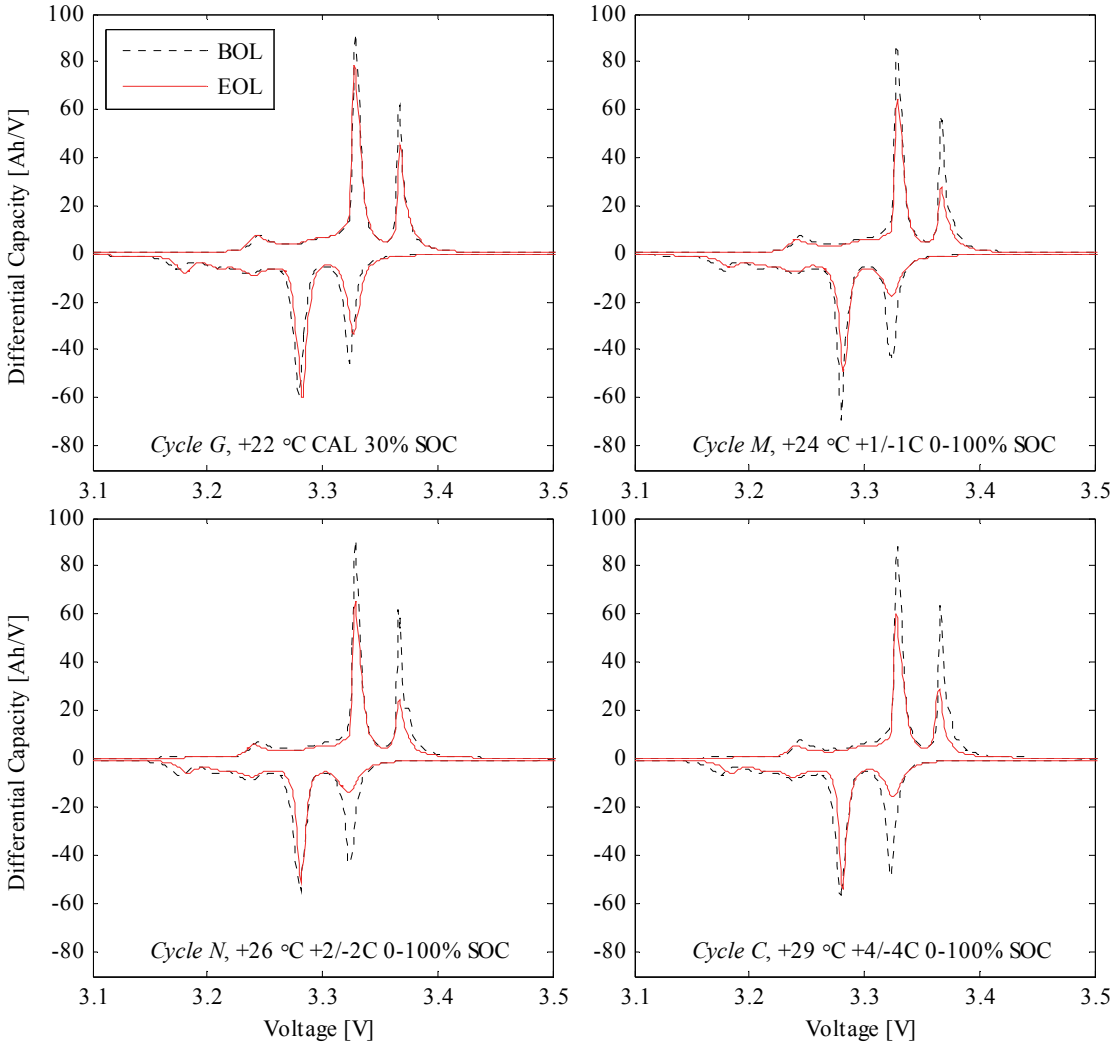

Figure 4.12 ICA profiles at BOL and EOL for *Cycle G, M, N & C* at temperatures below +30 °C. Dashed lines denote BOL and red lines denote EOL.

This is also indicated by the voltage profile model presented in Section 4.1 with simulation result presented in Figure 4.13 where a shortening of the last voltage plateau together with a slight compression of the curves can be seen for all cycles except *Cycle G*.

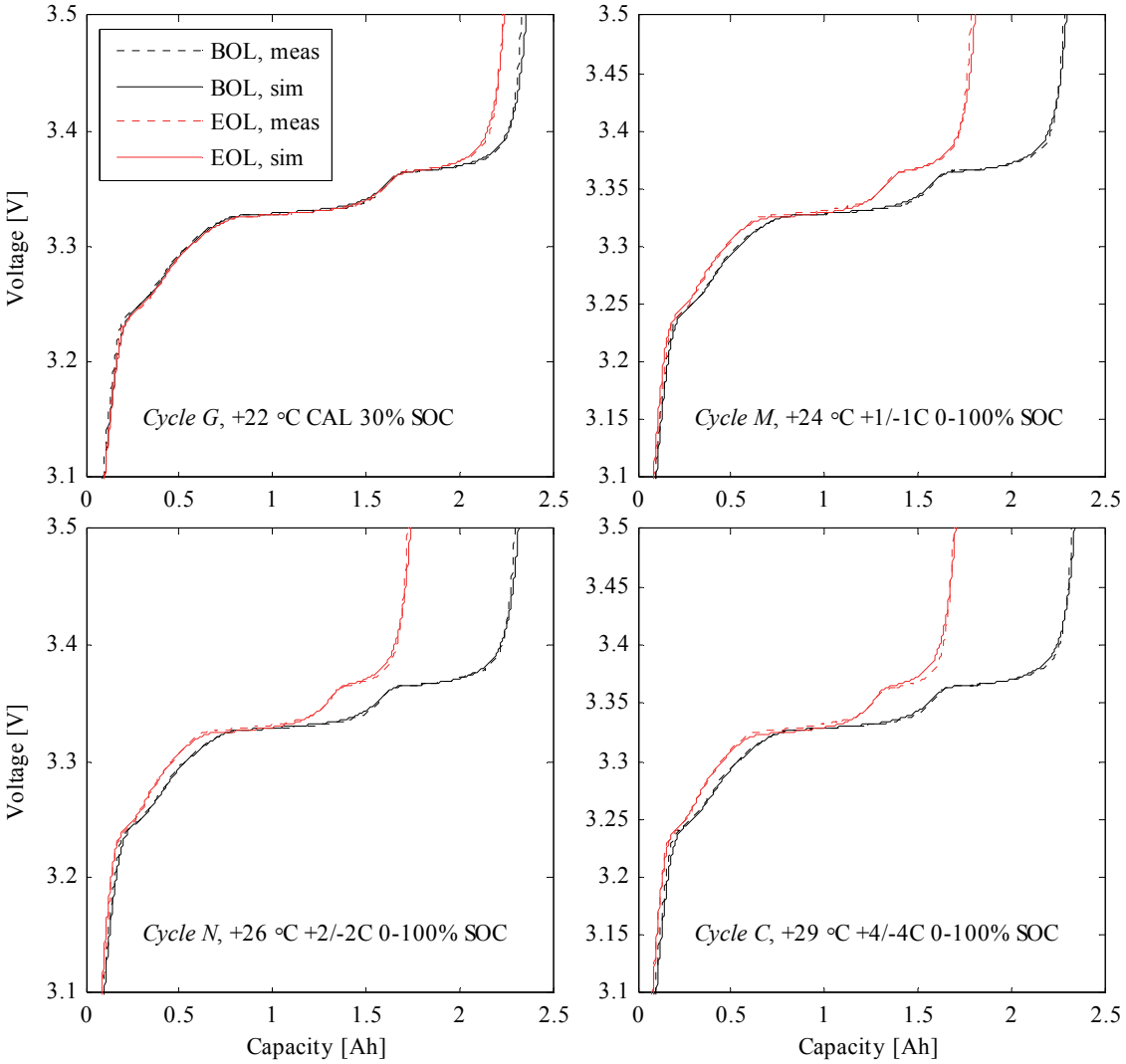

Figure 4.13 Voltage profiles at BOL and EOL for *Cycle G, M, N* & *C* at temperatures below +30 °C. Dashed lines denote BOL and red lines denote EOL.

In contrast to *Cycle M, N* & *C*, *Cycle H* causes significantly higher anode loss than all symmetric cycles and *Cycle I*, regardless of temperature. The opposite is apparent for *Cycle I*, with the lowest anode loss at EOL. The ICA of these two special cases is showed in Figure 4.14.

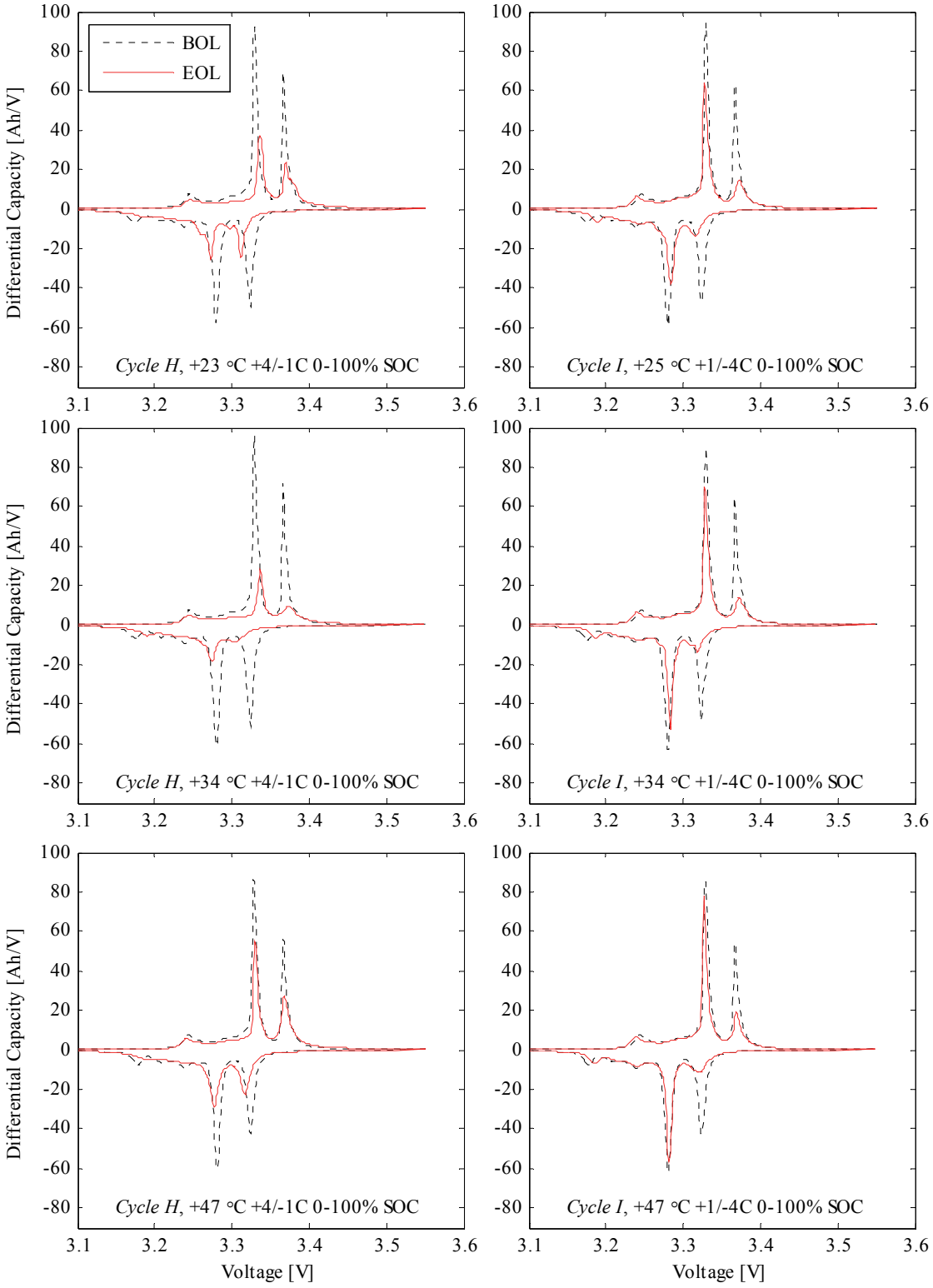

Figure 4.14 ICA profiles at BOL and EOL for *Cycle H & I* for temperatures between +23 °C and +47 °C. Dashed lines denote BOL and red lines denote EOL.

Chapter 5 Ageing Model

As previously discussed in this thesis there exists a wide variety of ageing models in literature ranging from complex first-principles models to empirical models. A simplified 1D lumped parameter model of electrode and electrolyte was designed in MATLAB®Simulink® to investigate and quantify the distribution of currents, SOC and subsequently SOH in this comparably simple model structure. All parameter values were determined by a combination of data sets found in literature and parameter fitting based on measured cell behaviour. The purpose was to find a compromise with enough accuracy to reflect actual full cell performance at a complexity level that permits integration into full vehicle simulation models.

5.1 Design

At the top level the cell was modelled as three separate and independent parts: cathode, separator and anode; in turn consisting of both solid and liquid phases (see Figure 5.1).

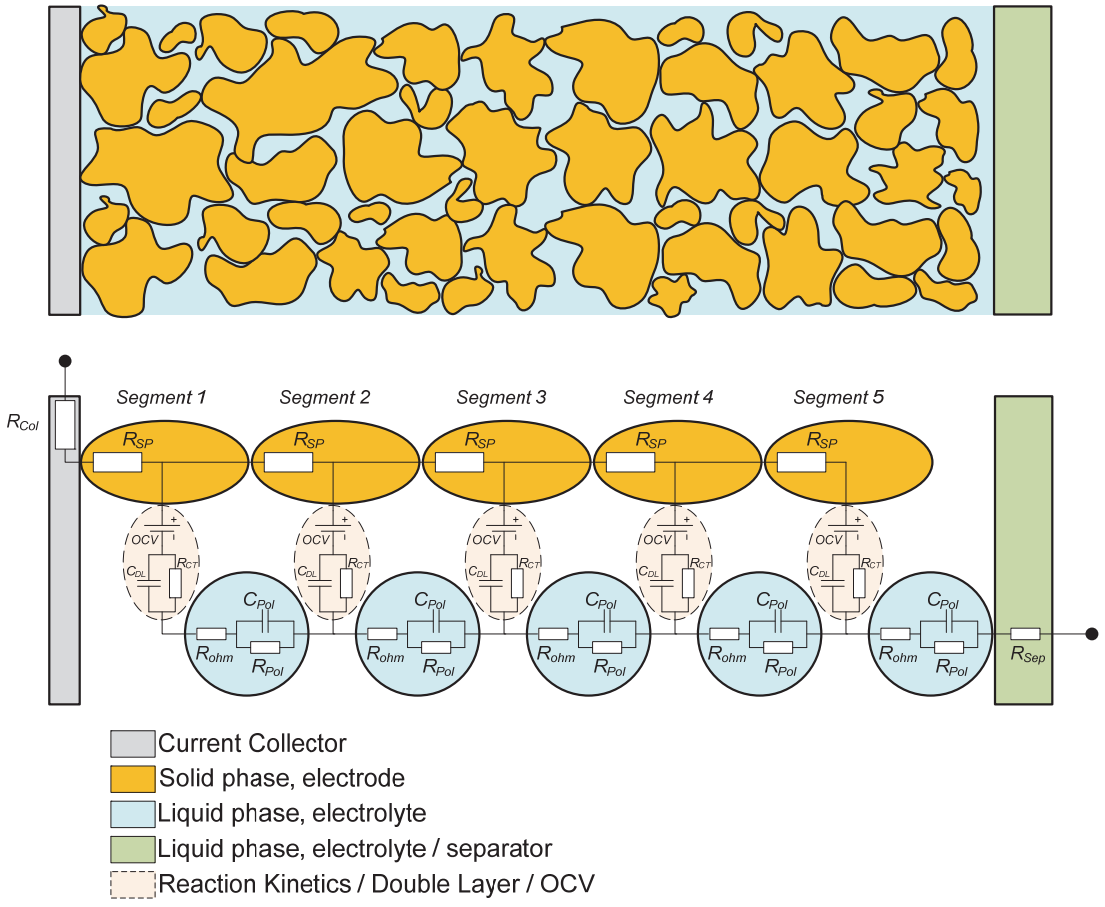

Figure 5.1 Overview of electrode / electrolyte sub-model. Top: Physical model. Bottom: 5-segment lumped parameter model

At this second level each electrode consists of five identical parts (see Figure 5.1) very similar to the simplified electrode and cell models developed by [48] and [38]. Here, each part is modelled as a simple network of linear electrical components forming the third, and lowest, level of the model. Although the electrodes and the separator are modelled and simulated separately, they are directly dependent as the same current flows in all three models.

In principle, the electrodes in this model design can be divided in any number of segments. Initial tests indicated that five segments represented a good compromise between accuracy and computational effort.

The solid phase of the electrode is modelled as a constant and ideal resistance connected both to adjacent electrode sections and to a circuit network representing the actual electrochemical reaction. This simplified reaction is defined with a minimum of parameters (Table 5) and described further in the following sub-sections.

Table 5 Electrode model parameters (origin given in table foot note)

Component / property	Label	Description / value	Dependencies
Open circuit voltage	OCV^1	Equilibrium voltage vs. Li/Li^+	SOC (local)
Current collector resistance	$R_{Col}{}^2$	Collector & tab conductivity	-
Electrode ohmic resistance	$R_{SP}{}^2$	Solid phase conductivity	Temperature
Double layer capacitance	$C_{DL}{}^2$	Reaction kinetics; time constant	Temperature
Charge transfer resistance	$R_{CT}{}^3$	Reaction kinetics; magnitude	SOC (local) & Temperature
Electrolyte ohmic resistance	$R_{ohm}{}^3$	Solid phase conductivity	Temperature
Electrolyte polarisation resistance	$C_{Pol}{}^3$	Polarisation; time constant	Fixed
Electrolyte polarisation resistance	$R_{Pol}{}^3$	Polarisation; magnitude	Temperature
Electrolyte bulk resistance	$R_{Sep}{}^2$	Free electrolyte / separator conductivity	Temperature
State-of-Charge	SOC^4	Local electrode segment SOC	Current (local)
State-of-Health	SOH^5	Local electrode segment SOH	Current & SOC (local)

1. **Half-cell measurement**
2. **Assumption / fitting towards measured full cell voltage response**
3. **Fitting towards galvanostatic intermittent titration technique (GITT) tests**
4. **Integration of local segment current**
5. **Separate SOH algorithm described in the following sections**

5.2 Parameterisation

Ideally, all parameters described in Section 5.1 should be either given by material properties or measured directly for the studied cell. This is however not possible as it would require a full cell specification and extensive sub-electrode disassembly and characterisation. Instead, a combination of half-cell measurements, full-cell characterisations, literature data and parameter fitting was used to optimise the cell model performance in a relatively limited operating range. The aim of this method was

not to optimise cell performance for a specific cycle, rather to enable sufficient accuracy for all studied cases, in turn providing insight to the current, SOC and SOH distribution within each electrode.

The following sub-sections provide a brief description of each of the model parameters in Table 5.

5.2.1 Open Circuit Voltage

The OCV of each electrode segment was modelled with a 1D look-up table based on a close-to-equilibrium OCV at C/10 measured on half-cells built from a mildly calendar aged sample cell (*Paper IV*). This OCV is presented in Section 4.1 where it is used to quantify the overall cell ageing.

5.2.2 Cell Impedance

Whereas the conductivity in the solid phase and the collector were modelled using temperature dependent resistances R_{SP} and R_{Col} a slightly more complex relation based directly on the *Butler-Volmer* relation

$$i = \frac{A}{2}\left(e^{\alpha B\eta} - e^{-(1-\alpha)B\eta}\right) = \left[\alpha = \frac{1}{2}\right] = \frac{A}{2}\left(e^{\frac{B\eta}{2}} - e^{-\frac{B\eta}{2}}\right) = A\sinh\left(\frac{B\eta}{2}\right) \tag{5.1}$$

was used for the charge transfer resistance

$$R_{CT(DC)} = \frac{\eta}{i} = \frac{2}{AB}\cdot\frac{\sinh^{-1}\left(i/A\right)}{i/A} \tag{5.2}$$

$$R_{CT(AC)} = \frac{2}{AB}\cdot\frac{1}{\sqrt{\left(1+\left(\frac{i}{A}\right)^2\right)}} \tag{5.3}$$

where constants A and B are electrode specific and in turn depending on SOC and temperature through a look-up table and polynomial fit respectively. These parameters were calculated using

$$R_X = f\left(R_{Col}, R_{SP}, R_{Ohm}, R_{Pol}, R_{Sep}\right) \tag{5.4}$$

and

$$Z_{Tot} = R_{CT} + R_X \tag{5.5}$$

and through fitting towards cell measurements using galvanostatic intermittent titration technique (GITT) at three current rates: 1, 5 and 10 C-rates respectively, presented with

voltage *vs.* SOC in Figure 5.2. Note that although the charge current is reduced below the respective set value for a wide SOC range, the polarisation of the cell is still large, and hence so also the total measured impedance.

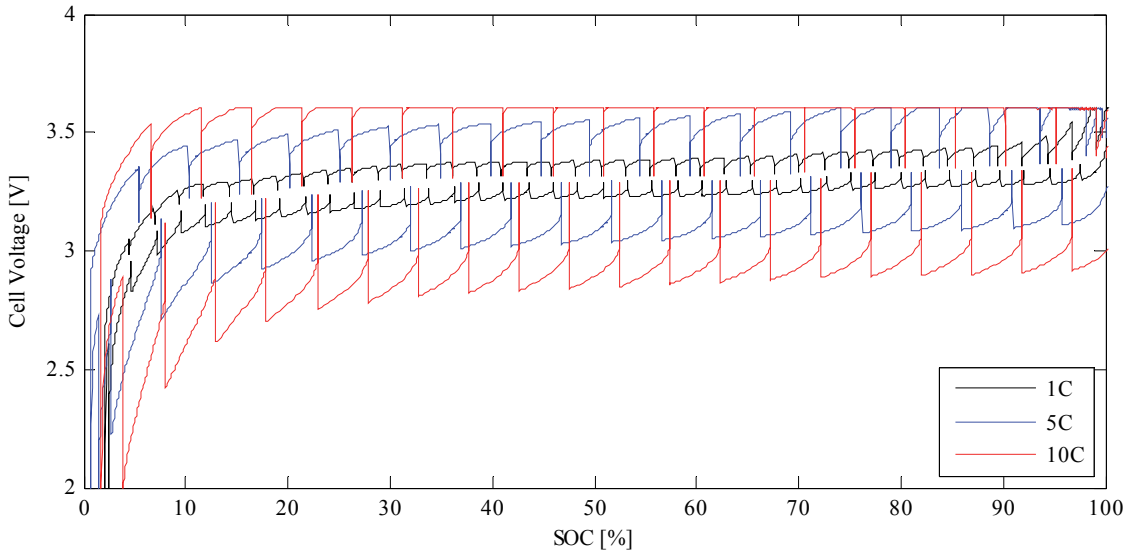

Figure 5.2 Voltage *vs*. SOC for the GITT tests at 1, 5 and 10 C-rate at +22 °C

Here, all the equivalent cell resistance components except R_{CT} were treated as a single fixed value R_X (5.4), in turn calculated using a least-square fitting to minimize the error between the simulated R_{CT} according to (5.2) and the GITT measurements. Once R_{CT} was calculated, the individual components of R_X were calculated or estimated as described later in this section. GITT measurements at charge and discharge currents were taken separately and combined to form a single current direction independent impedance vector, only depending on current rate and Li-content in each electrode. In other words, the high impedance observed for high or low cell SOC was assumed to be symmetric with respect to SOC, and directly related to low Li-content X in either the anode (Li_XC_6) or cathode (Li_XFePO_4). Thus, high impedance will be observed at high cell SOC since the Li-content in the cathode is low, and likewise for low cell SOC where the Li-content in the anode is low. This method does also to some extent compensate for the lack of true measurement of charge impedance at high current rates (current limitation due to CCCV operation).

The relation between cell SOC and electrode Li-content was calculated using the electrode capacities and offset at BOL presented in Section 4.2. Both anode and cathode were assumed to have the same charge transfer impedance at BOL as indicated in *Paper IV*.

The resulting parameter values of *A* and *B* are presented in Figure 5.3 and the resulting total cell impedance according to (5.2, 5.4 & 5.5) is shown in Figure 5.4 together with the measured values.

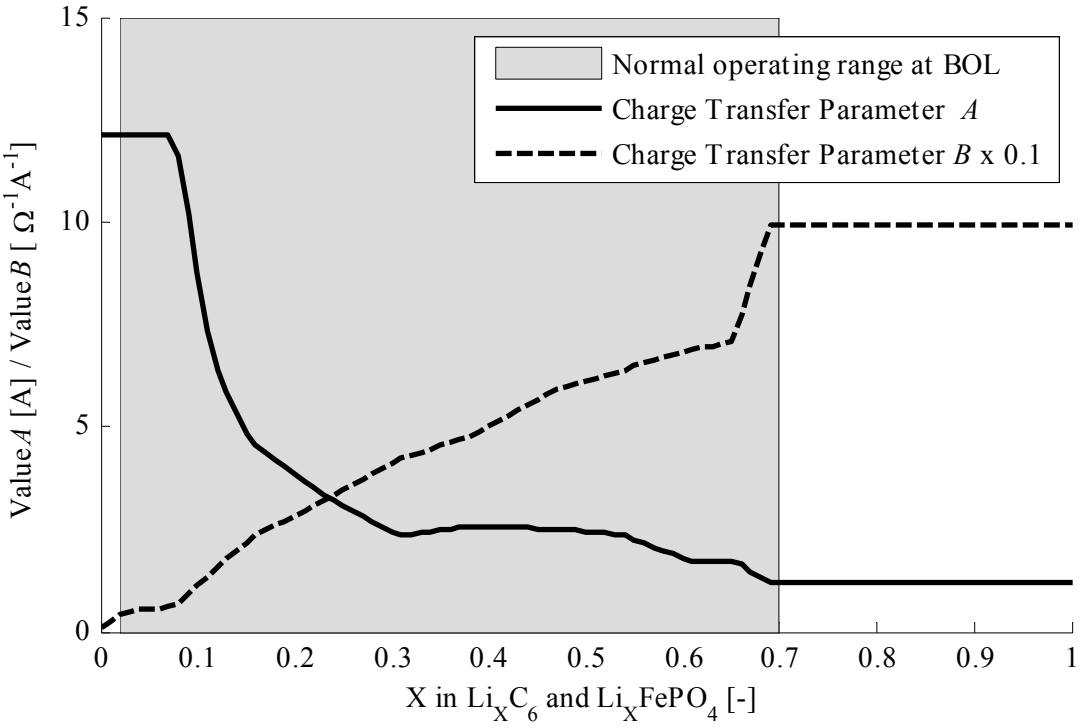

Figure 5.3 Fitted values of charge transfer parameters *A* and *B*

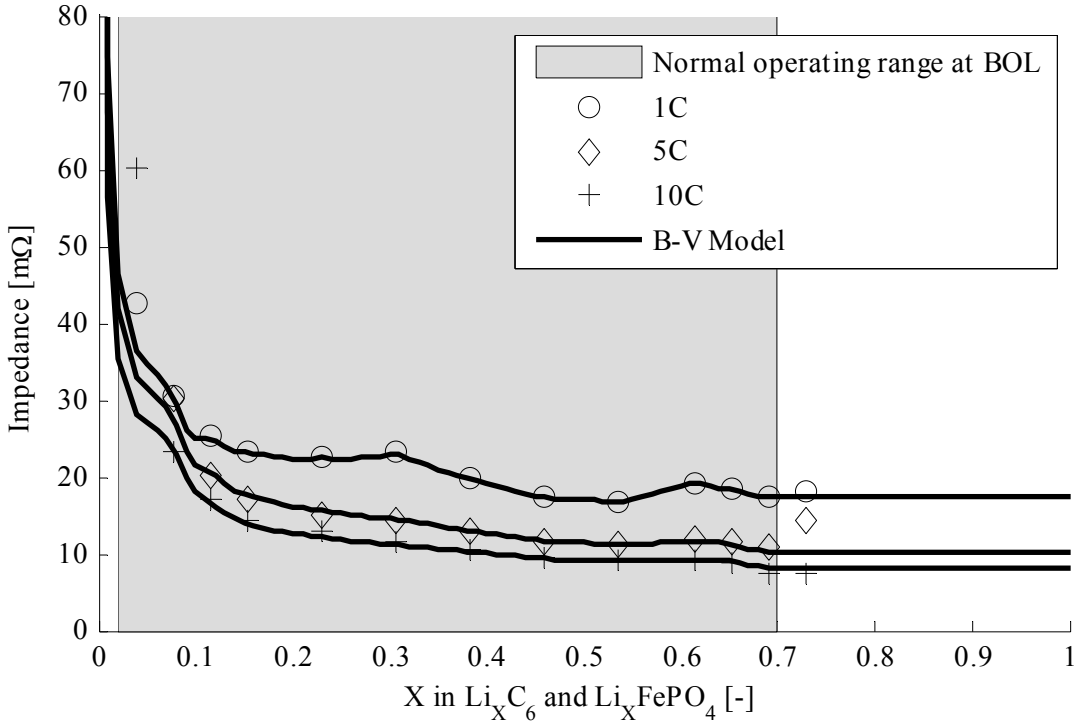

Figure 5.4 Measured cell impedance from GITT experiments using 1, 5 and 10 C-rate together with model response using fitted values for *A*, *B*, and R_X

Note that the parameter values were extrapolated using end values to regions outside the cell's operational range in terms of individual electrode SOC values to at least allow simulation in this range, since an expanded range is expected at severe cell degradation. In general, a good agreement between measurements and simulated impedance was achieved for low to medium SOC. This is expected since mass transport in the solid phase is not accounted for in this model. In summary, sufficient accuracy is achieved in the normal operating range at BOL.

The double-layer capacitance was initially modelled as a constant and linear capacitance, but simulations showed that its effect on overall cell model behaviour at the studied operating conditions was relatively small; as expected, accuracy was merely improved during transient operation since the time constant is comparably short. Hence, a simplified model without double layer capacitance was used for the majority of the test cases to enable shorter computational times. On the other hand, since the surface properties of the electrodes, especially for the graphite anode, changes with degradation, the double-layer should ideally be included in the model to the cost of computational complexity.

Polarisation Resistance

The use of a resistance-capacitance couple is commonly used in battery equivalent circuits to model the overall time dependence and to some extent the limited mass transport. Several RC-couples can be used to capture dynamics with different time constants and the parameterisation is relatively straight-forward. Naturally, the actual cell resistance due to polarisation is significantly more complex; different polarisation is apparent in different parts of the cell and strongly depending on cell design, local concentration gradients, distribution of current and temperature as well as ageing. Nonetheless, accurate modelling at such low level requires both a complex model and precise knowledge of the electrolyte which generally is not available for commercial cells. Moreover and as already discussed in the scope of this work, a complex low level model does not permit fast operation in full vehicle simulations. Hence, a model with two time constants was considered to be adequate to model concentration polarisation R_{Pol} in the liquid phase. While the two time constants were fixed and selected using fitting towards the GITT measurements, the polarisation resistance R_{Pol} was made temperature dependent based on EIS measurements performed at three temperatures.

Ohmic Resistances

All ohmic resistances (5.4) were modelled as temperature dependent only, *i.e.* with no dependence on time, local SOC or other internal states. Since no detailed data were available on the relation between them, fitting towards measured cell data and assumptions were used to find relevant parameter values. The following assumptions were made and used in the subsequent fitting algorithms:

R_{Col}: small contribution to overall cell impedance, therefore assumed to be zero.

R_{SP}: fixed value, temperature dependence

R_{Sep}: fixed value, temperature dependence, magnitude same as R_{SP}

R_{ohm}: fixed value, temperature dependence, magnitude same as R_{SP}

R_{Pol}: fixed value, temperature dependence, magnitude significantly larger than R_{SP}

Table 6 Fitted values of model parameters

Parameter	Value	Description / value	Estimation principle	Dependencies
R_{Col}	0 mΩ	Collector & tab conductivity	Assumption / fitting	-
R_{SP}	1.5 mΩ	Solid phase conductivity	Assumption / fitting	Temperature
C_{DL}	-	Reaction kinetics; time constant	-	Temperature
R_{CT}	~4-32mΩ	Reaction kinetics; magnitude	Based on GITT	SOC (local) & Temperature
R_{ohm}	1 mΩ	Solid phase conductivity	Assumption / fitting	Temperature
τ_{Pol}	10s & 200s	Polarisation; time constant	Assumption / fitting	Fixed
R_{Pol}	3.5 mΩ	Polarisation; magnitude	Assumption / fitting	Temperature
R_{Sep}	1.5 mΩ	Free electrolyte / separator conductivity	Assumption / fitting	Temperature

Temperature Dependence

The temperature dependence was determined based on EIS performed on a sample cell at various SOC levels and three temperatures: +22 °C, +33 °C and +41 °C. Typical spectra (Figure 5.5) at 40-60% SOC were fitted towards the impedance model described in Chapter 3 and in [1] and the resulting values in turn fitted to a low-order polynomial relation for the three different temperatures. In this equivalent circuit model the polarisation impedance is represented by a constant phase element with a complex and frequency dependent impedance, here denoted as the *Warburg* impedance. To extract a relevant value for the polarisation resistance R_{pol} for the use with the electrode model in the present work, the real part of the *Warburg* impedance at 10Mhz was used.

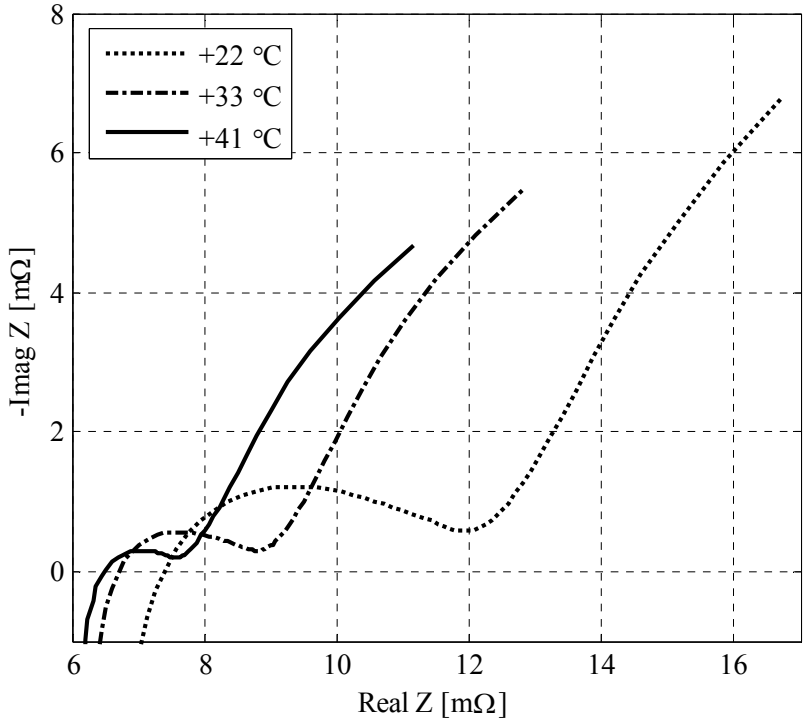

Figure 5.5 Typical EIS spectrums for three different temperatures

The polynomial expressions, with results shown in Figure 5.6, were then applied as weight factors for model parameters; all ohmic resistances (R_{SP}, R_{ohm}, R_{Sep}) with the relation for R_{ohm}, parameters A and B for charge transfer impedance according to R_{CT} and polarisation resistance according to R_{Pol}.

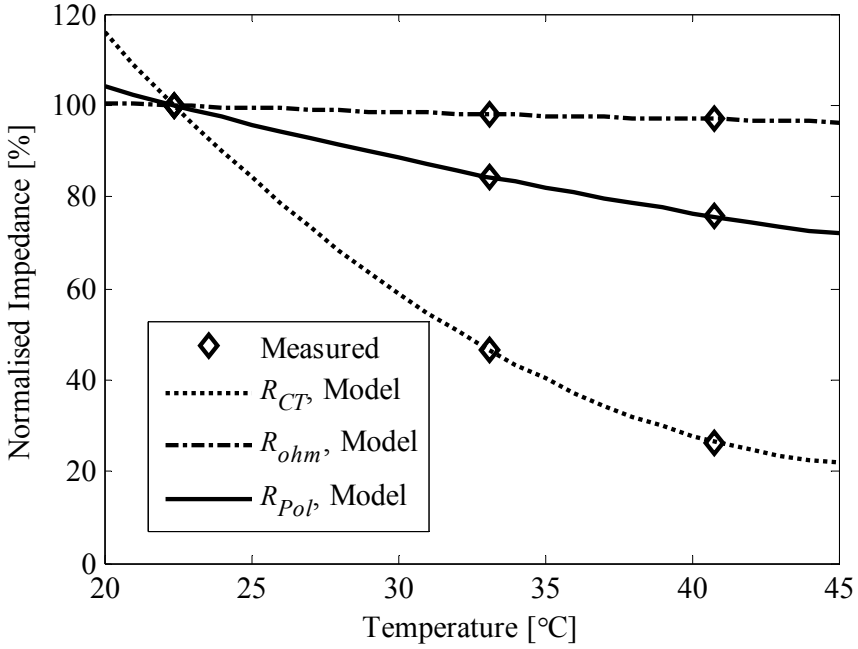

Figure 5.6 Fitted values with polynomial temperatures dependence

The relations in Figure 5.6 show several important characteristics of the studied cell: Firstly, all resistances show noteworthy temperature dependence which hence must be included in the electrode model. Secondly, the most pronounced temperature dependence is seen for the charge transfer impedance, followed in magnitude by the polarisation resistance. These two parameters, together with the choice of cell design, directly affect the current distribution in the cell and thereby performance.

As previously presented in Chapter 3 and *Paper V* all these impedance values change as the cell is degrading. Unfortunately, each parameter undergoes different ageing trends although the fundamental change most frequently is an increase over time and/or number of cycles. Hence, several simplifications to these relations were made in order to enable model simulation at different states of degradation. Generally, the average values of the observed trends were used together with empirical findings as described below.

In general, the total ohmic resistance R_{ohm} of the cell was found to be approximately proportional to the inverse capacity loss. However, an assumption was made that the resistance growth mainly occurred at the electrode surface rather than in the electrolyte, therefore a stronger relation for the solid phase resistance R_{SP} was used in the model. Likewise, the charge transfer impedance was assumed to follow the inverse of the cell SOH, and the polarisation resistance the inverse square root of the SOH. All these relations are presented schematically *vs.* cell SOH in Figure 5.7.

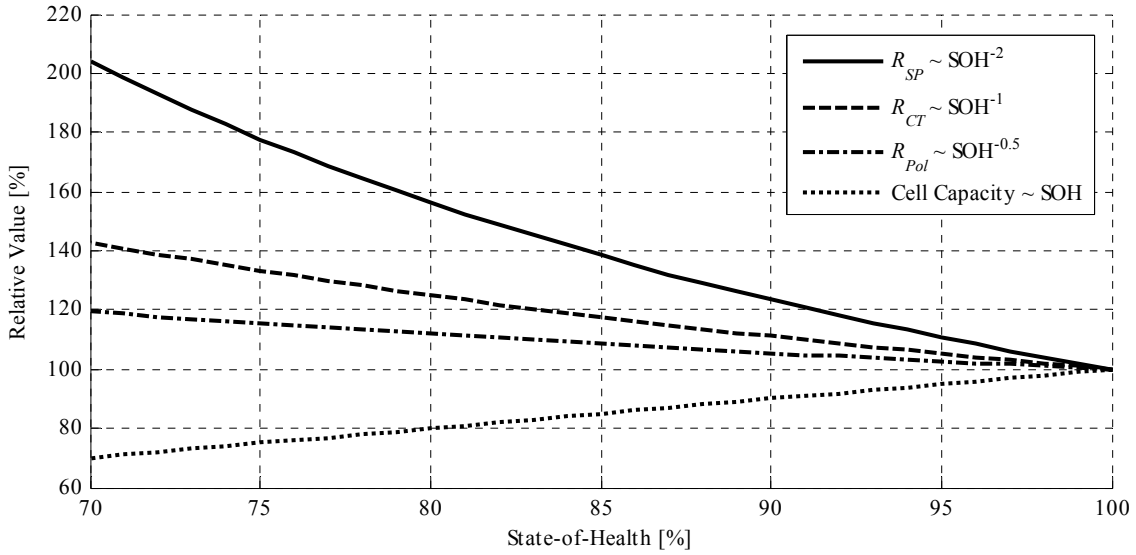

Figure 5.7 Schematic representation of the relations between resistances and cell SOH

5.2.3 State-of-Charge and State-of-Health

Each segment of the electrode contains a rudimentary SOC calculation algorithm solely based on local current integration and an ideal columbic efficiency of 100%. The SOH algorithm on the other hand is more complex, although still comparably simple to avoid stretching the algorithm into a purely empirical design.

Since the idea behind the segmented electrode model is to capture, and characterise, the uneven current/SOC distribution it was considered to be of great importance to keep the actual SOH algorithm as simple as possible, relying on the model structure itself to indicate how different parts of the electrode(s) are likely to age at different conditions. Nevertheless, since the SOH of the segments, and subsequently the electrode and the full cell, changes very slowly compared to current distribution and SOC, the SOH expressed as degradation rate was calculated offline using the simulated segment SOH and currents. In this way, a further development of the SOH algorithm is possible without changing the model. Also, the model may be initialised with different SOH in different segments to study behaviour at various stages of ageing and with different distribution. Nevertheless, a semi-continuous simulation of SOH during a cycle life test was still simulated in a step-wise manner where the estimated degradation over a small part of the cycle life is used to re-initialise the model and to re-estimate degradation. In other words, complete cycle life simulations were split up in a low number of simulations where the degradation rate is estimated. The estimated degradation after a defined number of cycles in terms of capacity retention and impedance change per electrode segment was then used to re-initialise the model and to estimate a new degradation rate as presented schematically in Figure 5.8.

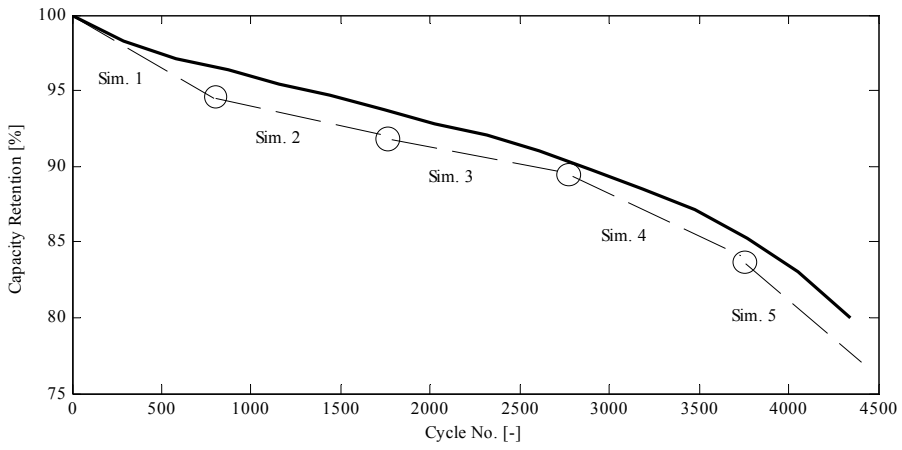

Figure 5.8 Schematic representation of a step-wise method for simulation a complete cycle life test based on five steps. Circles mark re-initialisation and start of simulation.

This step-wise method was used in the test and validation of the ageing model, see Section 5.4.

The general ageing model is based on the cumulative loss function

$$C = C_{BOL} \cdot \left(1 - \kappa_{Loss,A/L}\right)^{CT} \tag{5.6}$$

where C is the cell or anode capacity, C_{BOL} is the capacity at BOL, $\kappa_{Loss,A/L}$ is the LAAM (loss of anode material see Section 4.1.2) or cyclable lithium loss per complete capacity throughput and CT is the total capacity throughput.

The loss function $\kappa_{Loss,A/L}$ is in turn consisting of the base function

$$\kappa_{TI,A/L} = f\left(T, I\right) \tag{5.7}$$

with weight functions

$$\kappa_{SOC,A/L} = f\left(SOC, SOI\right), \tag{5.8}$$

$$\kappa_{SOH,A/Cell} = f\left(SOH_{A/Cell}\right) \tag{5.9}$$

and

$$\kappa_{CT} = f\left(Capacity\ throughput\right) \tag{5.10}$$

according to

$$\kappa_{Loss,A/L} = \kappa_{TI,A/L} \cdot \kappa_{SOC,A/L} \cdot \kappa_{CT} \cdot \kappa_{SOH,A/Cell} \tag{5.11}$$

The aim of this choice of ageing function is to account for the general ageing observed for simplified cycles such as *M*, *N* and *C* over the complete temperature range, the specific ageing observed for partial SOC, *i.e.* with cycles *D*, *K* and *L*, and the distribution of total capacity throughput between segments.

Firstly, the base function for ageing is similar to the empirical cycle life model presented in *Paper V*, but instead of an exponential function a two-dimensional second-order polynomial function

$$\kappa_{TI,A/L} = k_{1,A/L} + k_{2,A/L} \cdot T + k_{3,A/L} \cdot I + k_{4,A/L} \cdot T^2 + k_{5,A/L} \cdot T \cdot I + k_{6,A/L} \cdot I^2 \tag{5.12}$$

with parameter values $k_{1\text{-}6,A/L}$ based on a least-square fitting towards measured anode loss and cell capacity loss for cycles *M*, *N* and *C*. This relation was found to provide a reasonably good fit for both LAAM (Figure 5.9) and loss of cyclable lithium (Figure 5.10).

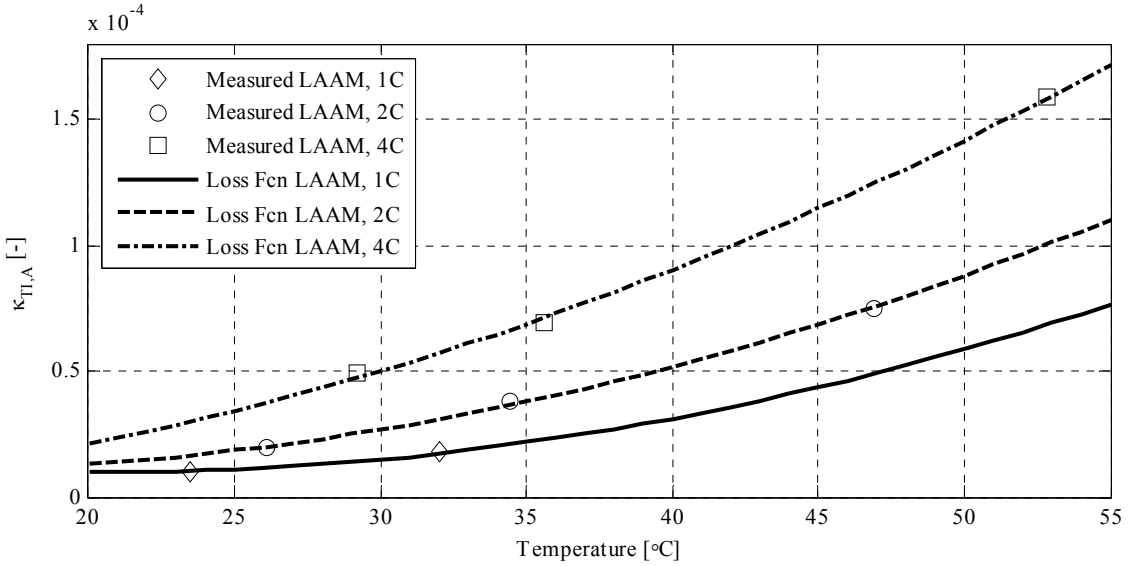

Figure 5.9 Ageing functions $\kappa_{TI,A}$ and measured values calculated for *Cycle M, N & C*

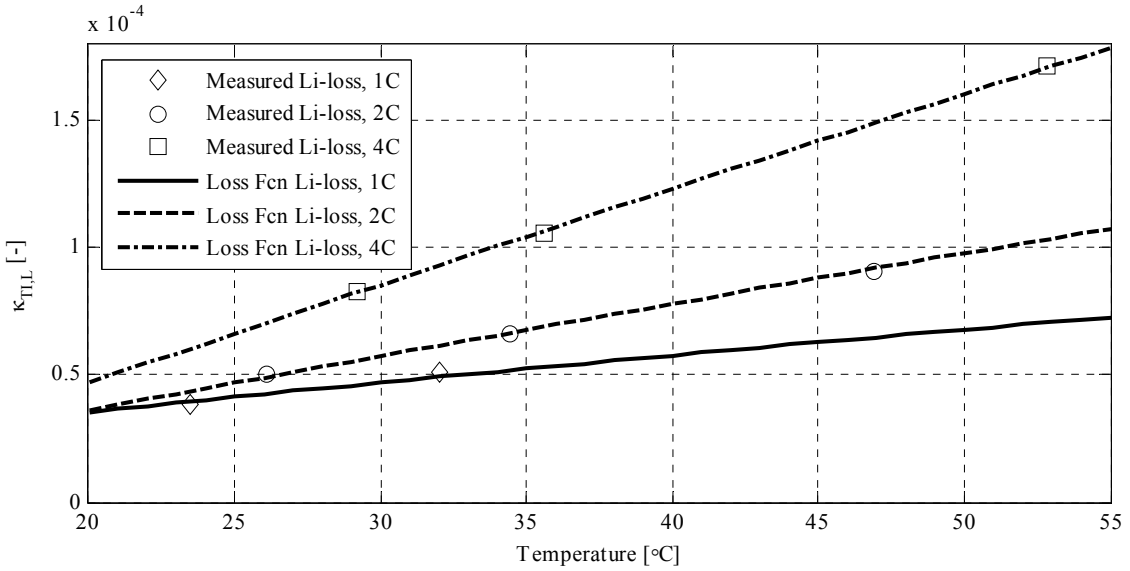

Figure 5.10 Ageing functions $\kappa_{TI,L}$ and measured values calculated for *Cycle M, N & C*

Here, both measurements and functions $\kappa_{TI,A/L}$, suggest a rather strong correlation between current rate and loss per cycle. Also, the loss of cyclable lithium has an almost linear dependence towards temperature whereas the LAAM shows a more progressive relation. It should however be pointed out that several more measurement points are needed to fully parameterise the two relations, especially for *Cycle M* at higher temperatures and in general for cycles with higher currents than 4 C-rate.

Secondly, the weight function $\kappa_{SOC,A/L}$ for SOC range was calculated as a simple function of SOC based on the estimated LAAM and loss of lithium for the *Cycles D, K & L*, all operating in different SOC ranges. These three cycles were tested in a narrow

temperature range and with almost identical load cycles and a SOC window of approximately 20%. Hence, most of the resulting difference in degradation rate was assumed to be attributed to the SOC range. The resulting values of $\kappa_{SOC,A/L}$ was here empirically found to follow the exponential relation

$$\kappa_{SOC,A} = k_7 e^{-k_8 \cdot SOC} + k_9 \tag{5.13}$$

for the anode loss and

$$\kappa_{SOC,L} = k_{10} e^{-k_{11} \cdot SOC} + k_{12} e^{-k_{13} \cdot SOC} + k_{14} \tag{5.14}$$

for the total loss of cyclable lithium.

In order to use these two functions as scale factors they were normalised so that the cumulative value over one complete cycle is equal to 1. That is, the function $\kappa_{SOC,A/L}$ will, when multiplied with the other loss functions, scale the degradation rate depending on actual SOC range. Both SOC weight functions are presented in Figure 5.11 together with the measured values (normalised).

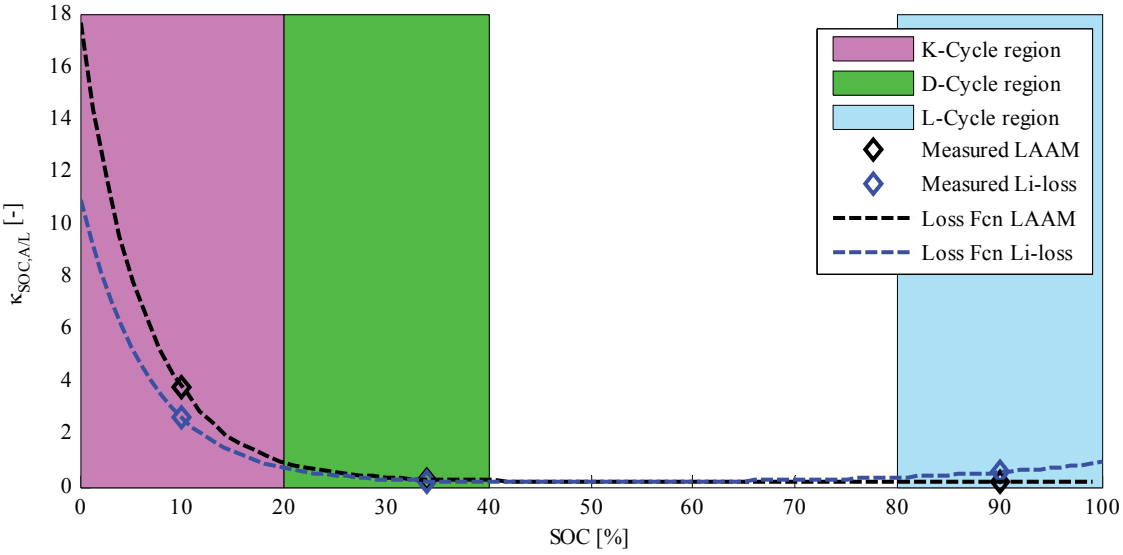

Figure 5.11 Ageing weight functions $\kappa_{SOC,A/L}$ and measured values calculated for *Cycle D, K & L*

Again, additional measurements would undoubtedly increase the accuracy of the relations, especially for very low and very high SOC levels.

Thirdly, the total degradation is a direct function of capacity throughput and this property varies over the electrode surface as supported by *Paper IV*. In the presented model, the capacity throughput is distributed over the different electrode segments and a separate weight function

$$\kappa_{CT} = CT_{segment} \big/ CT_{cell} \tag{5.15}$$

is used where $CT_{segment}$ is normalised according to

$$CT_{segment} = 5 \cdot \int_0^{t_{end}} \left| I_{segment} \right| dt \Big/ 2 \cdot Q_{ref,cell} \tag{5.16}$$

and

$$CT_{cell} = \int_0^{t_{end}} \left| I_{cell} \right| dt \Big/ 2 \cdot Q_{ref,cell} \tag{5.17}$$

and where $Q_{ref,\,cell}$ is the total cell capacity in As.

In other words, κ_{CT} is one for a cell with perfectly uniform capacity throughput. Note that no additional weight functions are used here, thus a non-uniform distribution will yield a linear degradation effect which may be an underestimation of actual degradation.

Lastly, an empiric relation was added to account for the acceleration of degradation observed over the complete duration of any cycle life test, *i.e.* the ageing rate increases for the vast majority of cycle life tests more than what can be expected from the linearly increasing current rate due to reduced capacity. It was found that the simple empirical relation

$$\kappa_{SOH,A/Cell} = 1 \big/ \left(SOH_{A/Cell} \right)^2 \tag{5.18}$$

where SOH_A is the state-of-health of the anode defined as

$$SOH_A = Q_{Anode} \big/ Q_{Anode,BOL} \tag{5.19}$$

and SOH_{Cell} is the state-of-health of the cell defined as

$$SOH_{Cell} = Q_{Cell} \big/ Q_{Cell,BOL} \tag{5.20}$$

provided a reasonably good fit to the experimentally observed acceleration of ageing rate with decreasing SOH. These two relations have a minor effect on the ageing rate until the overall ageing is already severe (*e.g.* a 23% increase at 90% capacity retention of anode or cell).

All ageing functions except κ_{CT} and $\kappa_{SOH,A/Cell}$ are continuously calculated to form a time dependent function that can be applied on the model output. These functions are subsequently used to calculate an average value per segment using the capacity as base instead of time since it was assumed that utilised capacity was more important than time. That is, it is more important to consider the capacity throughput at a certain SOC

or temperature than the test time. Hence, the average of the weight factors $\kappa_{TI,A/L}$ and $\kappa_{SOC,A/L}$ were calculated using

$$\overline{\kappa_{TI,A/L}} = \frac{\int_0^{Q_{end}} \left(\kappa_{TI,A/L}\right) dQ}{Q_{electrode}}, \tag{5.21}$$

$$\overline{\kappa_{SOC,A}} = \frac{\int_0^{Q_{end}} \left(k_7 e^{-k_8 \cdot SOC} + k_9\right) dQ}{Q_{electrode}}, \tag{5.22}$$

and

$$\overline{\kappa_{SOC,L}} = \frac{\int_0^{Q_{end}} \left(k_{10} e^{-k_{11} \cdot SOC} + k_{12} e^{-k_{13} \cdot SOC} + k_{14}\right) dQ}{Q_{end}} \tag{5.23}$$

where Q_{end} is a monotonically increasing absolute capacity vector according to

$$Q_{end} = \int_0^{t_{end}} \left| I_{segment} \right| dt, \tag{5.24}$$

$Q_{electrode}$ is the actual electrode capacity and $I_{segment}$ is the segment current.

In order to reduce the risk for overestimating degradation, the input values for the ageing functions $\kappa_{TI,A/L}$ were limited; to 1…10 C-rate and to +25…+55 °C respectively.

With the complete ageing factors parameterised, the expression

$$EOL_{est,A/L} = \frac{\ln(0.8)}{\ln\left(1 - \kappa_{Loss,A/L}\right)} \tag{5.25}$$

was used to provide an estimated cycle life considering $LAAM_{100}$ and loss of lithium and defining EOL at 80% capacity retention. Note that this relation is true only when starting from BOL.

All fitted coefficients for the ageing functions are given in Table 7. Note that the value for $\kappa_{SOC,A}$ is scaled for the lithium intercalation ratio SOI (state of intercalation) of the anode rather than the cell SOC.

Table 7 Ageing function coefficients obtained through fitting

Parameter	Value	Unit	Ageing Function	Cycles used for parameterisation
$k_{1,A}$	$4.78*10^{-5}$	-	$\kappa_{TI,A}$: current rate / T ageing function for LAAM	*M, N & C* at +23.5…+53 °C
$k_{2,A}$	$-3.14*10^{-6}$	$°C^{-1}$	$\kappa_{TI,A}$: current rate / T ageing function for LAAM	*M, N & C* at +23.5…+53 °C
$k_{3,A}$	$-1.55*10^{-5}$	A^{-1}	$\kappa_{TI,A}$: current rate / T ageing function for LAAM	*M, N & C* at +23.5…+53 °C
$k_{4,A}$	$5.58*10^{-8}$	$°C^{-2}$	$\kappa_{TI,A}$: current rate / T ageing function for LAAM	*M, N & C* at +23.5…+53 °C
$k_{5,A}$	$8.65*10^{-7}$	$[°CA]^{-1}$	$\kappa_{TI,A}$: current rate / T ageing function for LAAM	*M, N & C* at +23.5…+53 °C
$k_{6,A}$	$4.86*10^{-7}$	A^{-2}	$\kappa_{TI,A}$: current rate / T ageing function for LAAM	*M, N & C* at +23.5…+53 °C
$k_{1,L}$	$3.40*10^{-5}$	-	$\kappa_{TI,L}$: current rate / T ageing function for Li loss	*M, N & C* at +23.5…+53 °C
$k_{2,L}$	$-3.31*10^{-7}$	$°C^{-1}$	$\kappa_{TI,L}$: current rate / T ageing function for Li loss	*M, N & C* at +23.5…+53 °C
$k_{3,L}$	$-2.53*10^{-5}$	A^{-1}	$\kappa_{TI,L}$: current rate / T ageing function for Li loss	*M, N & C* at +23.5…+53 °C
$k_{4,L}$	$-3.45*10^{-9}$	$°C^{-2}$	$\kappa_{TI,L}$: current rate / T ageing function for Li loss	*M, N & C* at +23.5…+53 °C
$k_{5,L}$	$9.85*10^{-7}$	$[°CA]^{-1}$	$\kappa_{TI,L}$: current rate / T ageing function for Li loss	*M, N & C* at +23.5…+53 °C
$k_{6,L}$	$2.06*10^{-6}$	A^{-2}	$\kappa_{TI,L}$: current rate / T ageing function for Li loss	*M, N & C* at +23.5…+53 °C
k_7	17.4	-	$\kappa_{SOC,A}$: SOC region scale factor for anode loss	*D, K & L* at approx. +30 °C
k_8	20.7	SOI^{-1}	$\kappa_{SOC,A}$: SOC region scale factor for anode loss	*D, K & L* at approx. +30 °C
k_9	0.206	-	$\kappa_{SOC,A}$: SOC region scale factor for anode loss	*D, K & L* at approx. +30 °C
k_{10}	10.8	-	$\kappa_{SOC,L}$: SOC region scale factor for lithium loss	*D, K & L* at approx. +30 °C
k_{11}	14.7	SOC^{-1}	$\kappa_{SOC,L}$: SOC region scale factor for lithium loss	*D, K & L* at approx. +30 °C
k_{12}	$1.35*10^{-3}$	-	$\kappa_{SOC,L}$: SOC region scale factor for lithium loss	*D, K & L* at approx. +30 °C
k_{13}	-6.37	SOC^{-1}	$\kappa_{SOC,L}$: SOC region scale factor for lithium loss	*D, K & L* at approx. +30 °C
k_{14}	0.141	-	$\kappa_{SOC,L}$: SOC region scale factor for lithium loss	*D, K & L* at approx. +30 °C

In summary, the SOH function described in this section consists of a collection of simple relations comprising five ageing factors; average cell temperature, local current, local SOC, local capacity throughput and local SOH. Note specifically that no specific ageing factor is included for operation at partial SOC or narrow SOC widows, often reported in literature as a general ageing factor for capacity or power fade [49] and [50]. Although other ageing mechanisms, such as cathode material loss (LACM), can be estimated in a similar way, the lack of stable characterisation techniques for these ageing mechanisms (see Section 4.1) prohibited sufficient validation. Here, similar relations as those used for the anode ageing (5.6-5.25) may be used for the cathode as well, assuming full symmetry between electrodes. Nevertheless, the profound differences in material properties and ageing characteristics will in such case introduce uncertainties and significant lack of validation. Consequently, the ageing estimation treated in the remainder of this chapter will only treat anode aging resolved on segment level and cell capacity loss expressed as an average value of cyclable lithium loss.

5.3 Implementation

The focus in this section is to describe the background to and the design of the lumped parameter model. Therefore, a detailed description of the actual implementation in MATLAB®Simulink® will not be presented here. However, a brief description with key properties of the implementation and the simulation settings are given to aid further development. It shall be noted that this model environment is not intended for

simulation of physical systems with mixed time constants since they often contain several algebraic loops.

5.3.1 Electrode Model

Each electrode was modelled according to Figure 5.1 with five subsystems for each segment. These segments are identical from an algorithm point of view, but their internal implementation differs between middle segments and the end segment closest to the current collection in order to mitigate issues with the inherent algebraic loops. All segments are connected to each other with both inputs and outputs – potentials and currents – to create a fully dependent system where each segment will affect the system response immediately. Again, the algebraic loops that this design includes will inherently result in stability issues. However, these issues can be handled by carefully choosing feedback paths for the signals between the segments, disabling zero-crossing detection and reducing the tolerance of the solver to create a semi-stable model capable of working for all studied cases. In other words, feedback signals must be chosen so that they do not have an immediate effect on the receiving block, or being the output of a state function such as an integrator or filter with initial output.

An overview of the electrode model is presented in Figure 5.12 where the signal paths are highlighted to show the interconnections between segments. Note that all internal signals in the model are removed in this figure to enhance visibility. The main input is the current to/from the current collector. This current is distributed between the five segments directly depending on the internal states of the segments and the electrical network that connects them. Further details, with naming conventions and reference directions for each segment, are given in Figure 5.13.

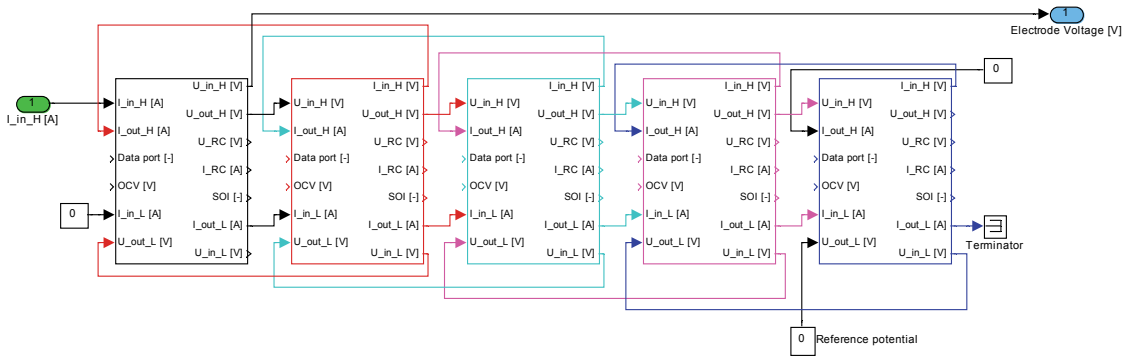

Figure 5.12 Electrode model in MATLAB®Simulink® showing the five segments.
Note: this figure only shows the interconnections between segments, neither all inputs nor outputs to the electrode model are included

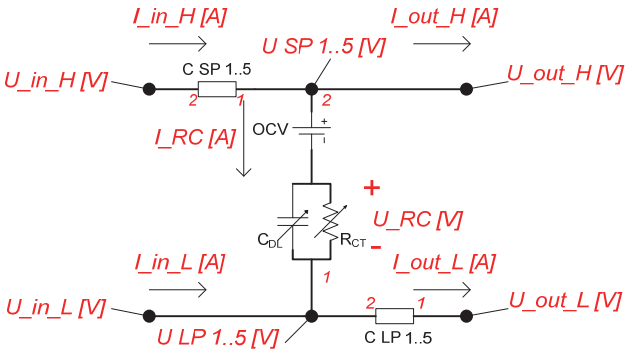

Figure 5.13 Electrode segment overview with signal interface

Naturally, all internal states and signal such as SOC, current and potentials can be extracted from the model and treated offline, enabling a qualitative analysis of the performance from an ageing perspective, as is described in the following section.

5.4 Simulation Results – Cycle Life Tests

This section presents simulation results for a collection of the studied test cases at BOL, focusing on distribution of SOC and current in each electrode. In the first part, the model output for some reference cases are discussed to provide an overview of the model functionality and performance. In the last part, the model is used to simulate the cell behaviour during the tested HEV and PHEV cycles as well as some specific test cases of interest.

5.4.1 Model Performance at Symmetric Cycle with Low Current Rate

The +1C/-1C symmetric *Cycle M* served as a reference cycle life test and was also partly used for parameterisation of the ageing model in the present work. When studying the current distribution (Figure 5.14 & Figure 5.15) it can be concluded that the model, with its present parameterisation, suggests a surprisingly uneven distribution with significantly higher current in the electrode segments closest to the separator (segment no. 5). In all figures with representation of current distributions, the segment currents are scaled to C-rates, *i.e.* the average of the five curves is exactly equal to the total cell current (also plotted in C-rate) for every given point in time.

In addition, it is shown that the high initial current is reduced as the SOC of these segments are reduced, in turn leading to a more even current distribution towards the end of charge and end of discharge. In addition, it can be concluded that an initially high

current in one segment is strongly related to the OCV of the electrode; in areas where the OCV is flat (low SOC for cathode, high SOC for anode) the distribution of segment currents is wide. This is expected since the electrolyte impedance is larger than the electrode impedance, thus favouring high currents at the surface as long as the change in OCV with SOC is smaller than the voltage drop over the segments.

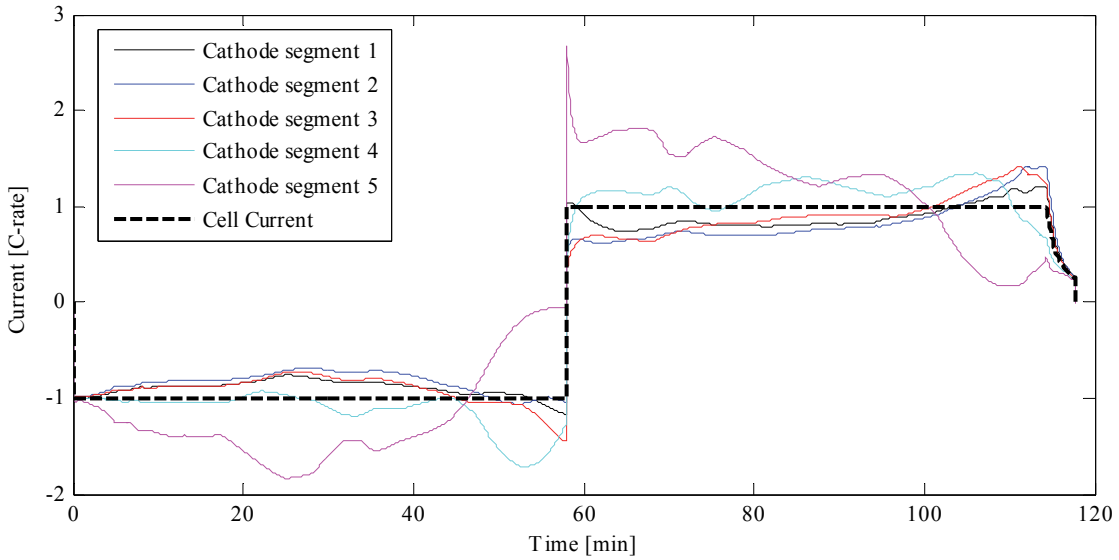

Figure 5.14 Cathode segment current and total cell current vs. time for *Cycle M* at +24 °C

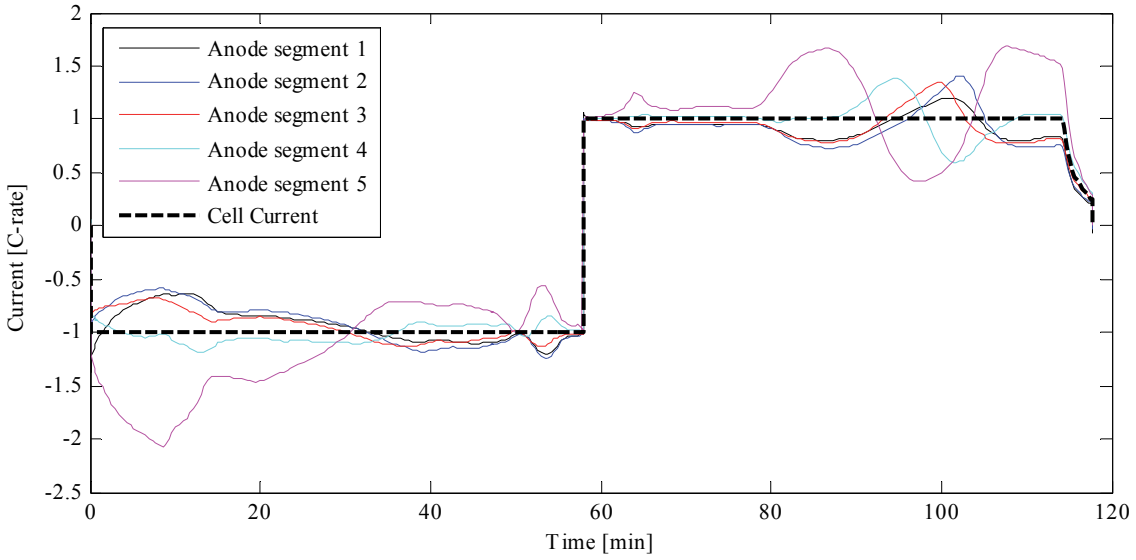

Figure 5.15 Anode segment current and total cell current vs. time for *Cycle M* at +24 °C

In addition to the electrode current distribution, the SOC distribution also reveals interesting differences between segments and electrodes. Naturally, this is directly a function of the current distribution as the SOC reflects the integrated current over time. In general, this distribution of currents and local SOC shows the same characteristics as the more advanced models presented by [15] and [25].

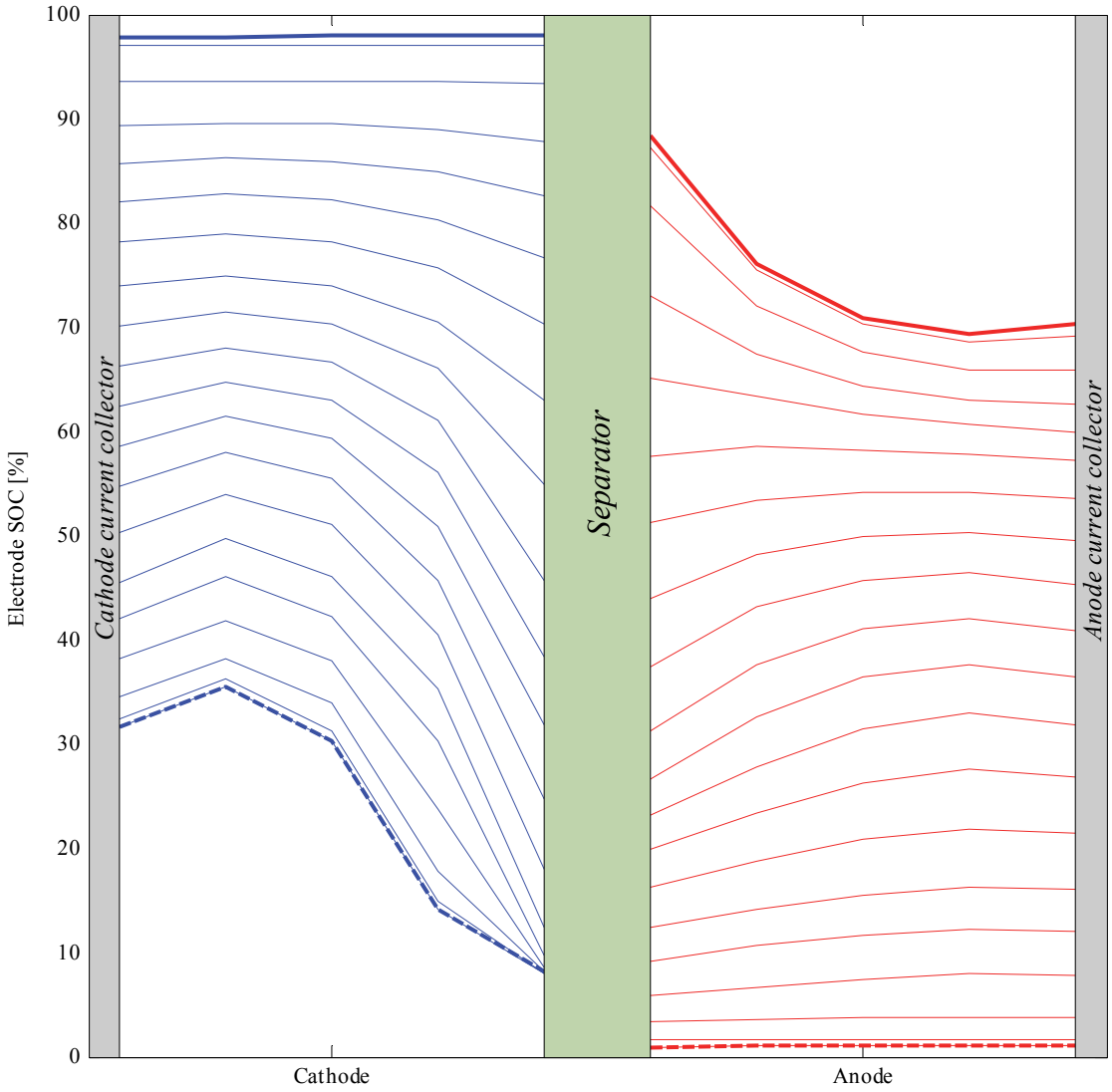

Figure 5.16 Electrode SOC distribution scaled to cell SOC vs. time during a complete discharge at 1 C-rate and +24 °C. The upper thick solid lines mark the start of discharge and the thick dashed lines mark the end of discharge. Thin lines represent the segment SOC at fixed time intervals between start and end of discharge.

Firstly, during the discharge at 1 C-rate (Figure 5.16), both segments close to the separator show SOC ranges significantly larger than the average cell SOC of each electrode. However, since the electrodes are larger in absolute capacity, the segment SOC stays within the valid operational area of each electrode. Also, since the current is gradually re-distributed to other segments towards end of discharge, there is no apparent risk of over-discharge.

Secondly, anode and cathode here show quite different behaviour, again directly due to the difference in OCV; whereas the cathode has a flat curve, permitting large imbalance in SOC (difference between segment SOC and average electrode SOC), the gradually

increasing anode potential results in an overall less imbalance. Also, note that the result in Figure 5.16 was recorded in the middle of a longer simulation. Thus, the cell did not start at equilibrium and the initial SOC distribution is therefore not even.

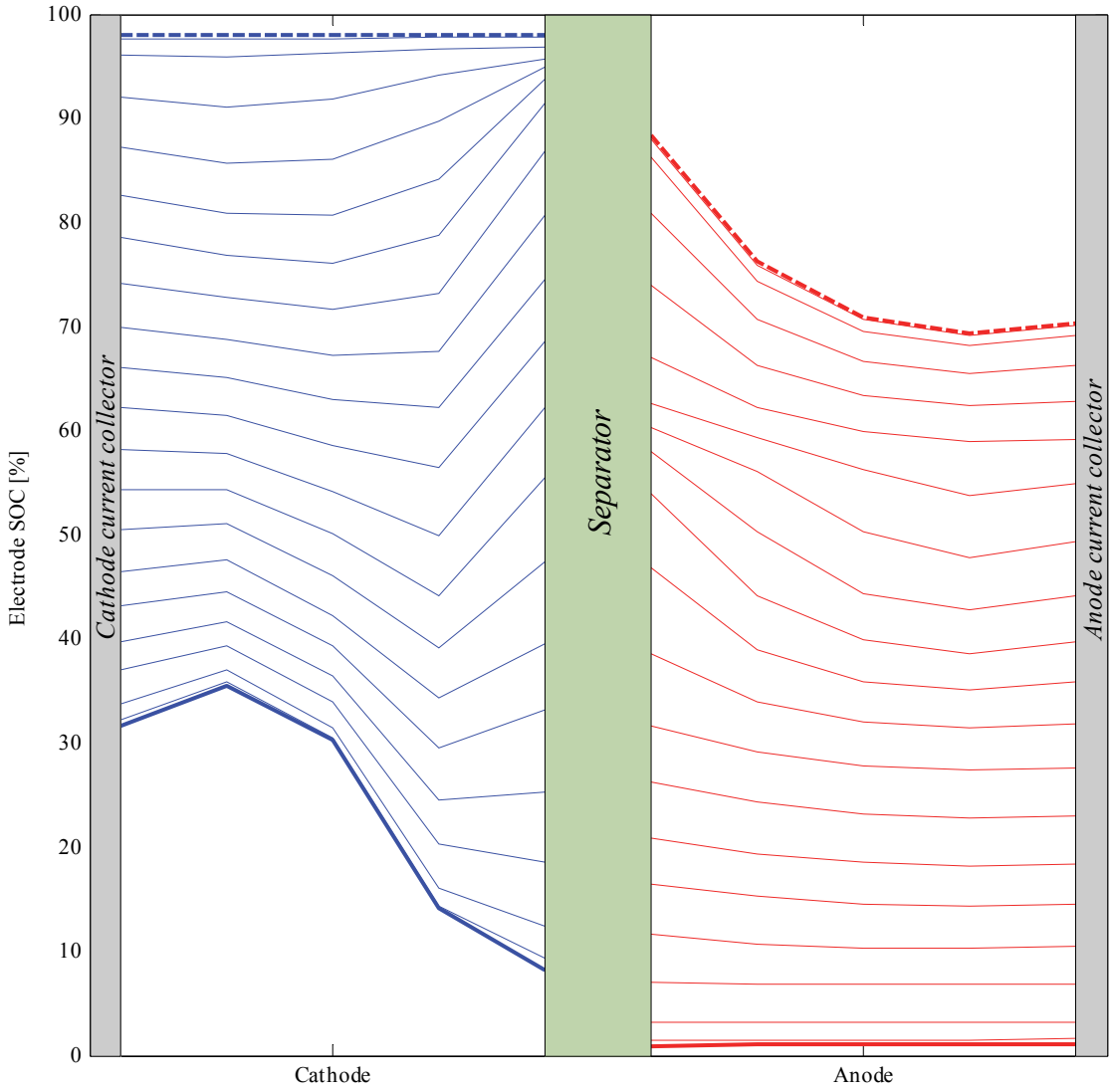

Figure 5.17 Electrode SOC distribution scaled to cell SOC vs. time during one complete charge at 1 C-rate and +24 °C. The lower thick solid lines mark the start of charge and the thick dashed lines mark the end of charge. Thin lines represent the segment SOC at fixed time intervals between start and end of charge.

Similar behaviour as for the discharge can be seen for the charge step shown in Figure 5.17. Here, the cell starts at 0% SOC and most of the electrode current is carried by the segments closest to the separator, effectively equalising the SOC imbalance. However, the imbalance (see Figure 5.18), here defined as the difference between maximum and minimum segment SOC, is not levelled out completely except for the cathode towards end of charge, again indicating that segment five experiences the largest SOC range in this cycle.

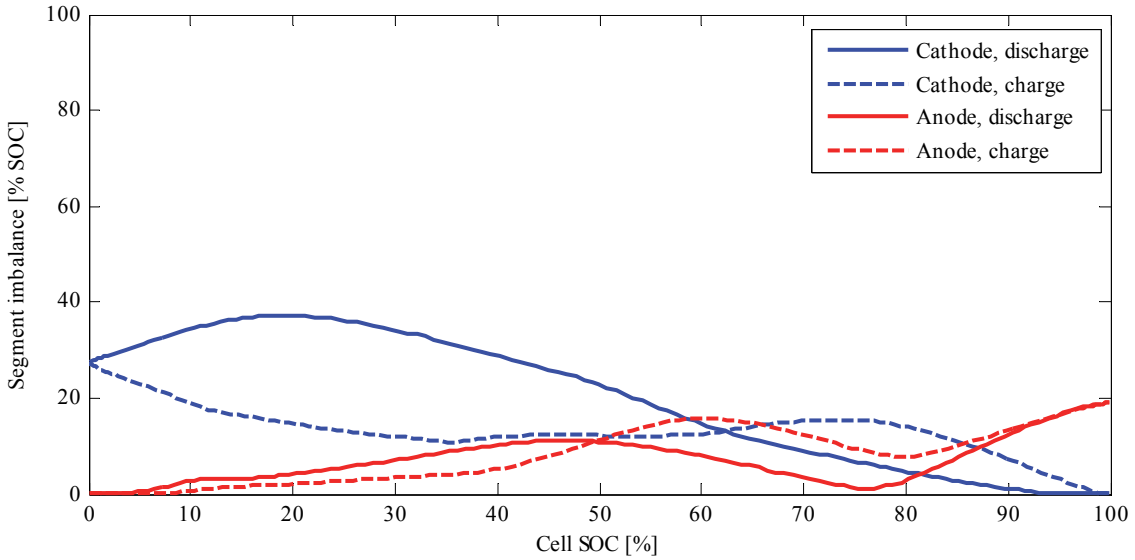

Figure 5.18 Segment imbalance in per cent vs. cell SOC, *Cycle M* at +24 °C.

The uneven current distribution can also be quantified as differences in capacity throughput per segment as shown in Figure 5.19. The largest differences are again shown for the cathode, where the two segments closest to the separator show significantly higher throughput than the other segments. As previously discussed, this is due to the flat OCV curve of $LiFePO^4$ *vs.* Li/Li^+.

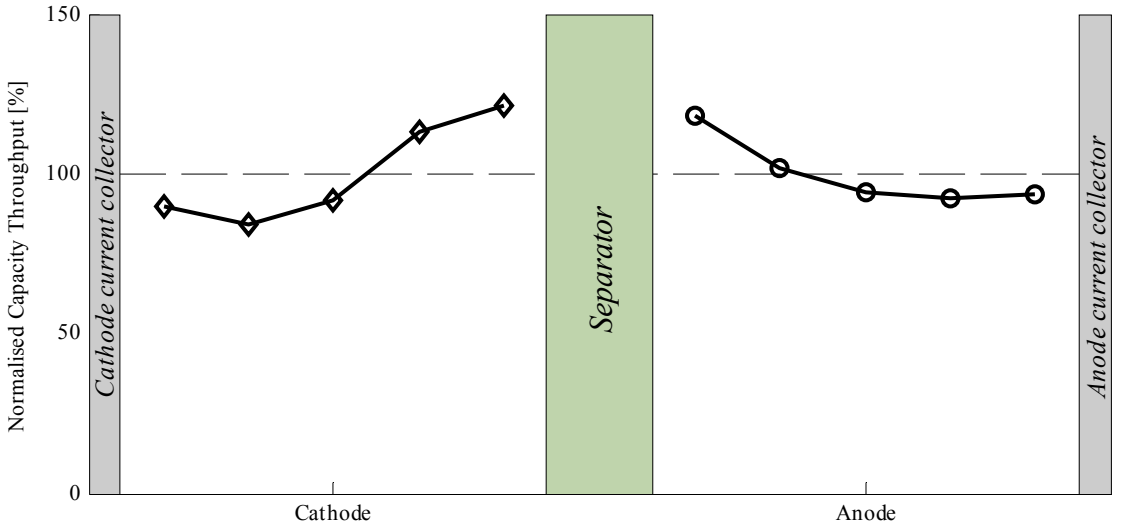

Figure 5.19 Capacity throughput per segment for *Cycle M* normalised to cell capacity throughput at +24 °C

A consequence of the distribution of currents and capacity throughput is that the resulting ageing factors $\kappa_{TI,A/L}$ (5.12) and κ_{CT} (5.15) are slightly different for the electrode segments, which in turn affects the cycle life. These ageing factors are,

however, changing over the cycle life of the cell as localised degradation affects the impedance and thus the current distribution. A stepwise simulation shows that although the ageing is uneven at BOL, the changing impedance of the segments yields a comparably flat and even ageing at EOL. This is presented in Figure 5.20 where the ageing factor for loss of cyclable lithium ($\kappa_{Loss,L}$) is shown as a function of SOH.

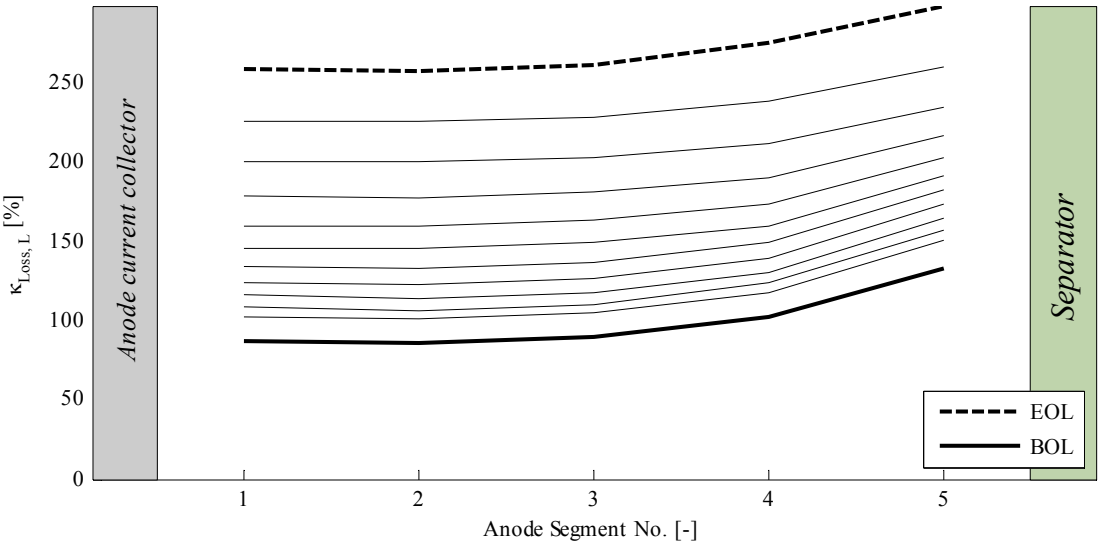

Figure 5.20 Normalised ageing factor $\kappa_{Loss,L}$ at the anode from BOL to EOL for *Cycle M* at +24 °C. Thin lines represent values between BOL and EOL at fixed interval.

The estimated cycle life for *Cycle M* (Figure 5.21) reflects the above presented distributions and corresponds well to the measured cycle life. Yet, it overestimates the ageing at the first stages of ageing and underestimates the ageing close to EOL. Nevertheless, this estimation is, as discussed previously, based on the assumption that the loss of cyclable lithium dominates the overall ageing.

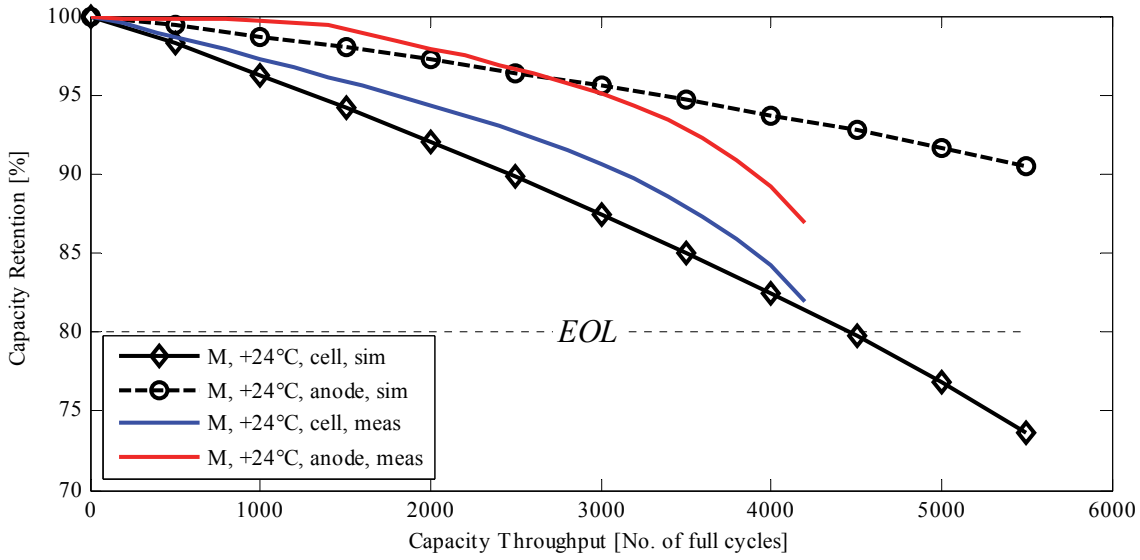

Figure 5.21 Estimated and measured cycle life of anode and cell for *Cycle M* at +24 °C

At higher temperatures the behaviour is almost identical to the reference case at +24 °C. However, the lowered charge transfer impedance results in a slightly larger maximum segment current and also a larger spread in SOC and current distribution. On the other hand, this is to some extent counteracted by the lower polarisation resistance. To sum up, the ageing rate in this cycle is mostly influenced by the temperature as a general ageing factor resulting in the lowered overall cycle life indicated in Figure 5.22, providing reasonably good estimation accuracy.

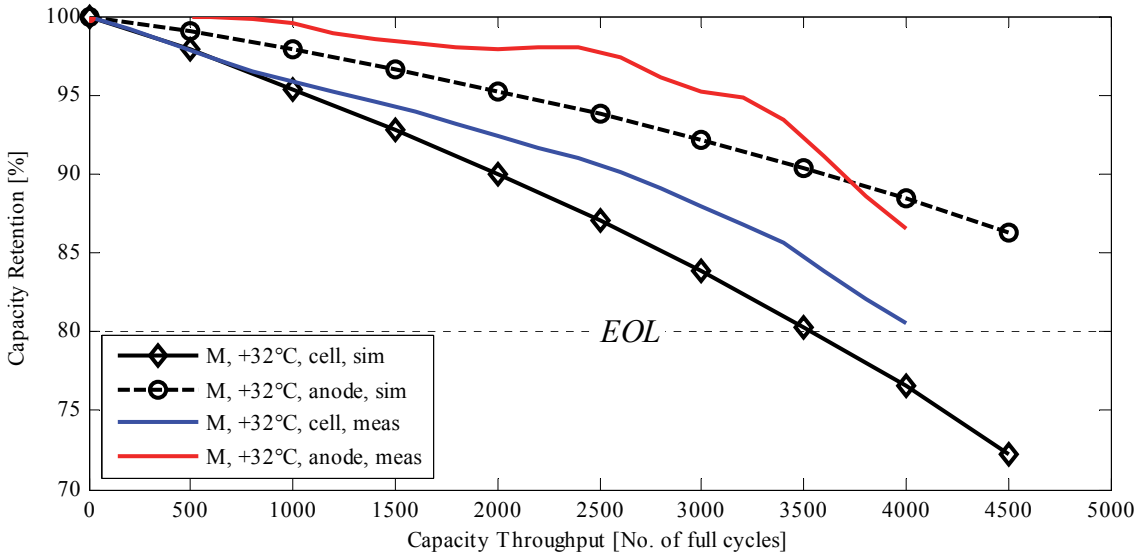

Figure 5.22 Estimated and measured cycle life of anode and cell for *Cycle M* at +32 °C

5.4.2 Model Performance at Symmetric Cycles with High Current Rates

When *Cycle N* with 2 C-rate is simulated the SOC segment imbalance (Figure 5.23) increases compared to the *Cycle M* with 1 C-rate, especially for the anode.

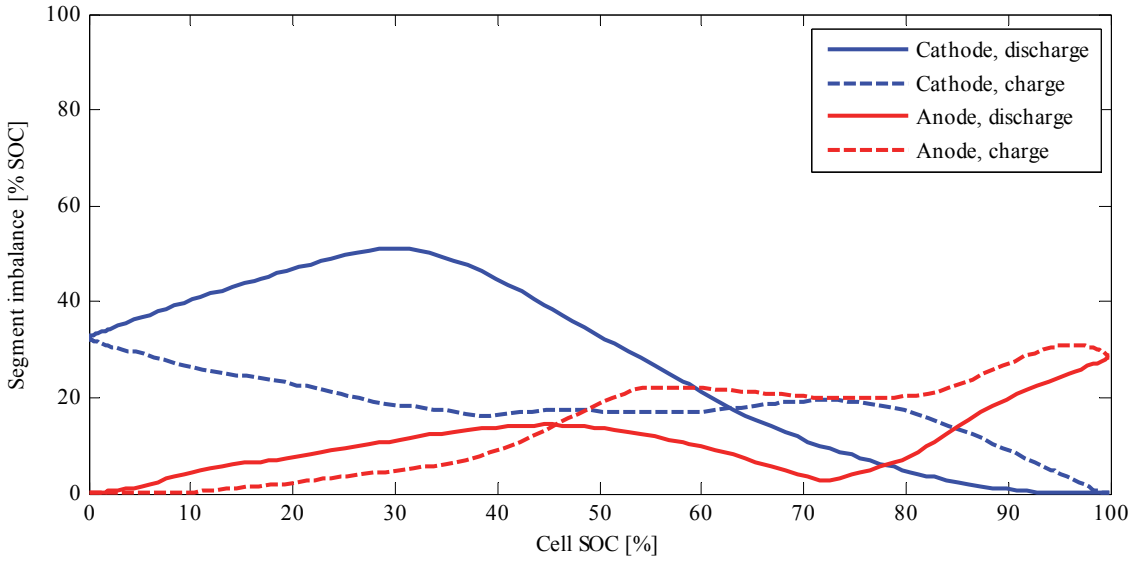

Figure 5.23 Segment imbalance in per cent vs. cell SOC, *Cycle N* at +26 °C

In addition, the capacity throughput for the anode segments (Figure 5.24) shows a broader distribution. In other words, segments closer to the separator are cycled significantly more than those close to the current collector.

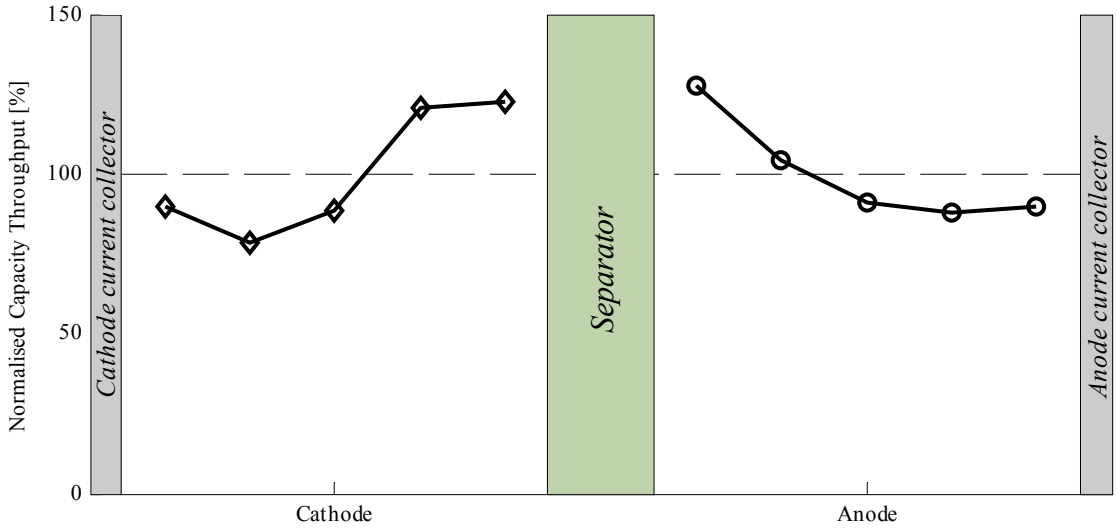

Figure 5.24 Capacity throughput per segment for *Cycle N* normalised to cell capacity throughput at +26 °C

The resulting ageing factors (Figure 5.25) are also less evenly distributed over the segments compared to the simulation of *Cycle M*.

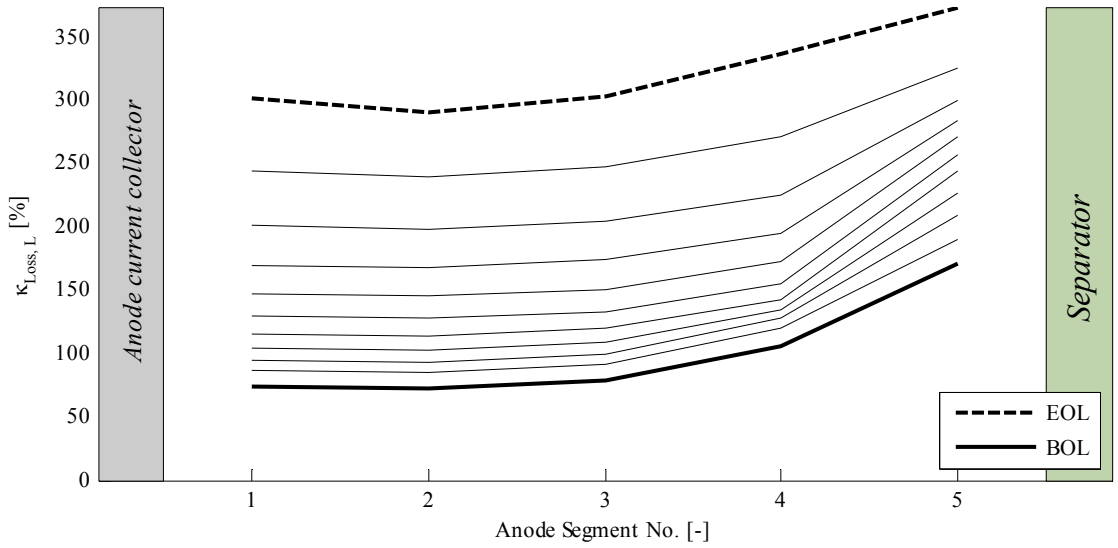

Figure 5.25 Normalised ageing factor $\kappa_{Loss,L}$ at the anode from BOL to EOL for *Cycle N* at +26 °C. Thin lines represent values between BOL and EOL at fixed interval.

This is also reflected in the estimation of cycle life (Figure 5.26) that indicates a shorter cycle life than for *Cycle M* with 1 C-rate.

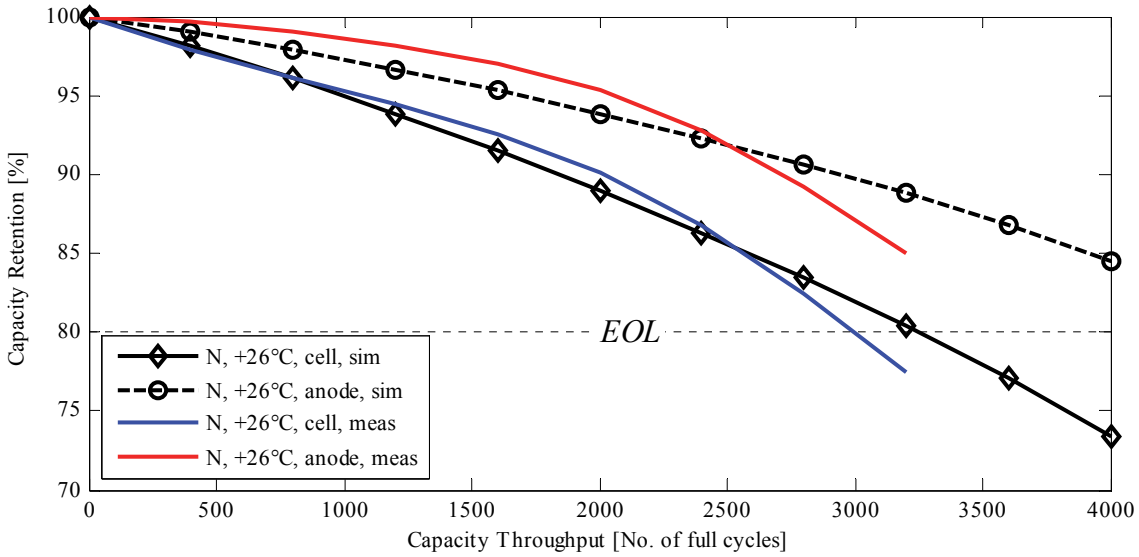

Figure 5.26 Estimated and measured cycle life of anode and cell for *Cycle N* at +26 °C

At higher temperatures; +34 °C (Figure 5.27) and +47 °C (Figure 5.28), the distribution of currents and SOC becomes more uniform, partly due to reduced charge transfer impedance, but the ageing factor of the increased temperature clearly dominates the overall ageing rate, resulting in a noteworthy reduction in cycle life as is also observed experimentally.

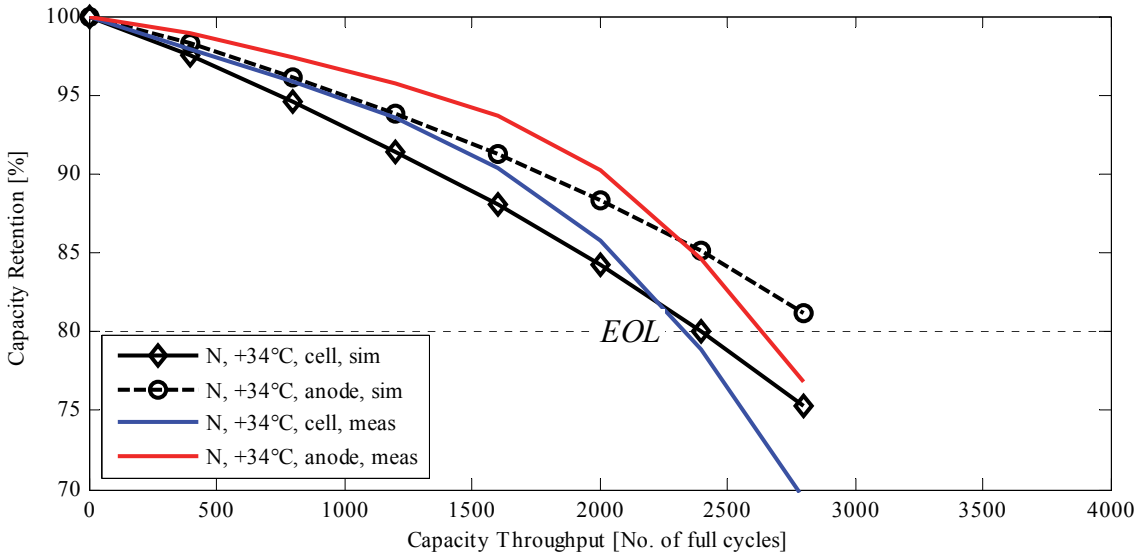

Figure 5.27 Estimated and measured cycle life of anode and cell for *Cycle N* at +34 °C

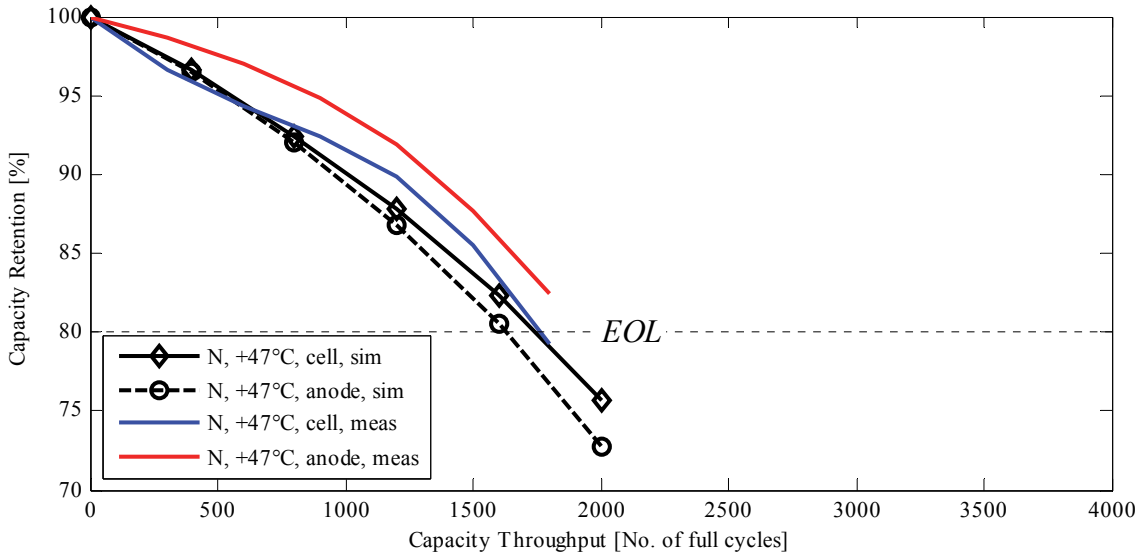

Figure 5.28 Estimated and measured cycle life of anode and cell for *Cycle N* at +47 °C

At 4 C-rate the model indicates that the imbalance between segments is severe (Figure 5.29); up to 40% for the anode and almost 60% for the cathode. Despite that these values are the result of a model parameterised solely on parameter fitting and assumptions, it is still likely that the imbalance at high current rates is increasing significantly, and thus, accelerating ageing.

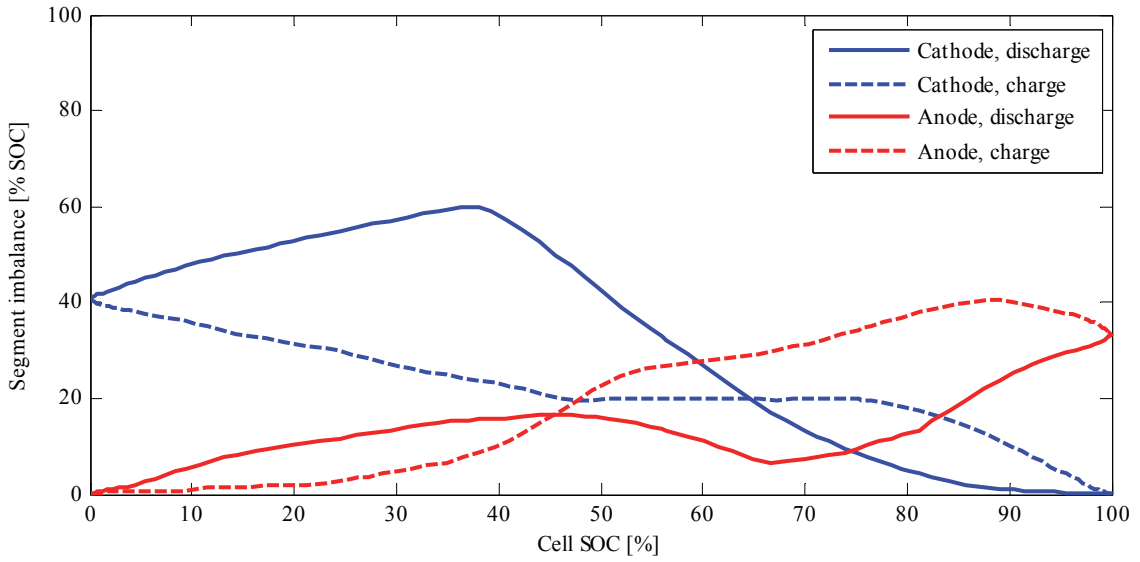

Figure 5.29 Segment imbalance in per cent vs. cell SOC, *Cycle C* at +29 °C

The segment imbalance is also clearly shown in the distribution of capacity throughput (Figure 5.30) where the segments of especially the cathode see very different throughput.

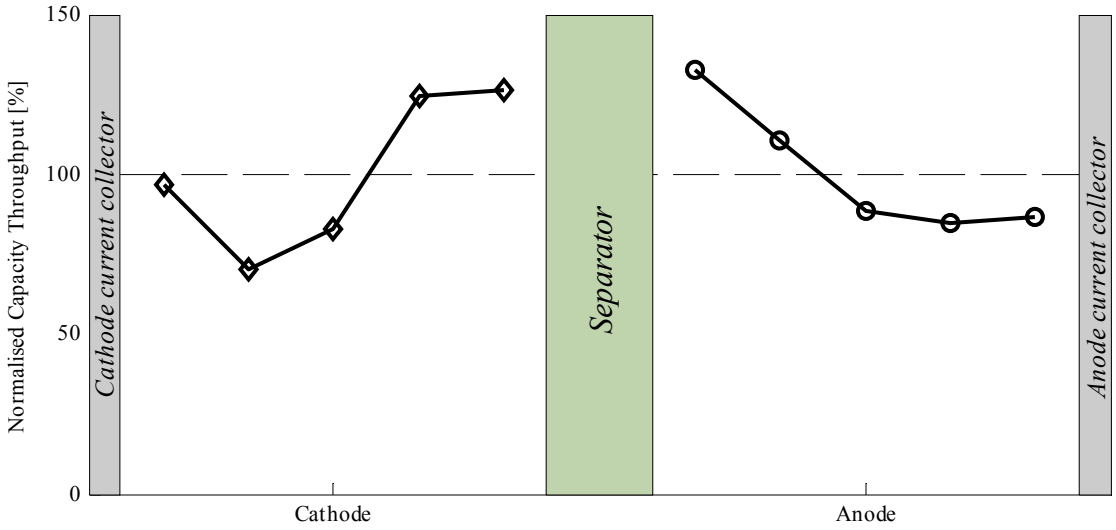

Figure 5.30 Capacity throughput per segment for *Cycle C* normalised to cell capacity throughput at +29 °C

The distribution of capacity throughput is directly correlated to the distribution of currents, here shown for the anode in Figure 5.31. The peak current is especially high during discharge, most probably due to the flat voltage profile of the anode at high cell SOC.

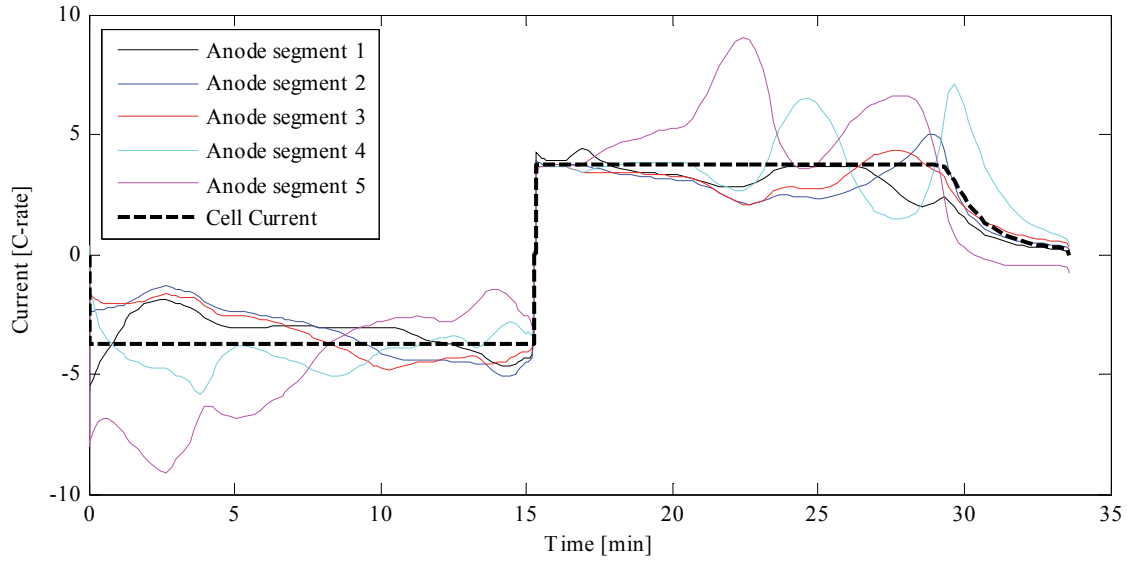

Figure 5.31 Anode segment current and total cell current vs. time for *Cycle C* at +29 °C

Furthermore, the actual SOC range of the electrodes have increased to almost 100% for both electrodes as can be seen in Figure 5.32, where the segments close to the separator at both cathode and anode are utilised to their full capacity whereas segments close to the current collectors merely are used to about 50%.

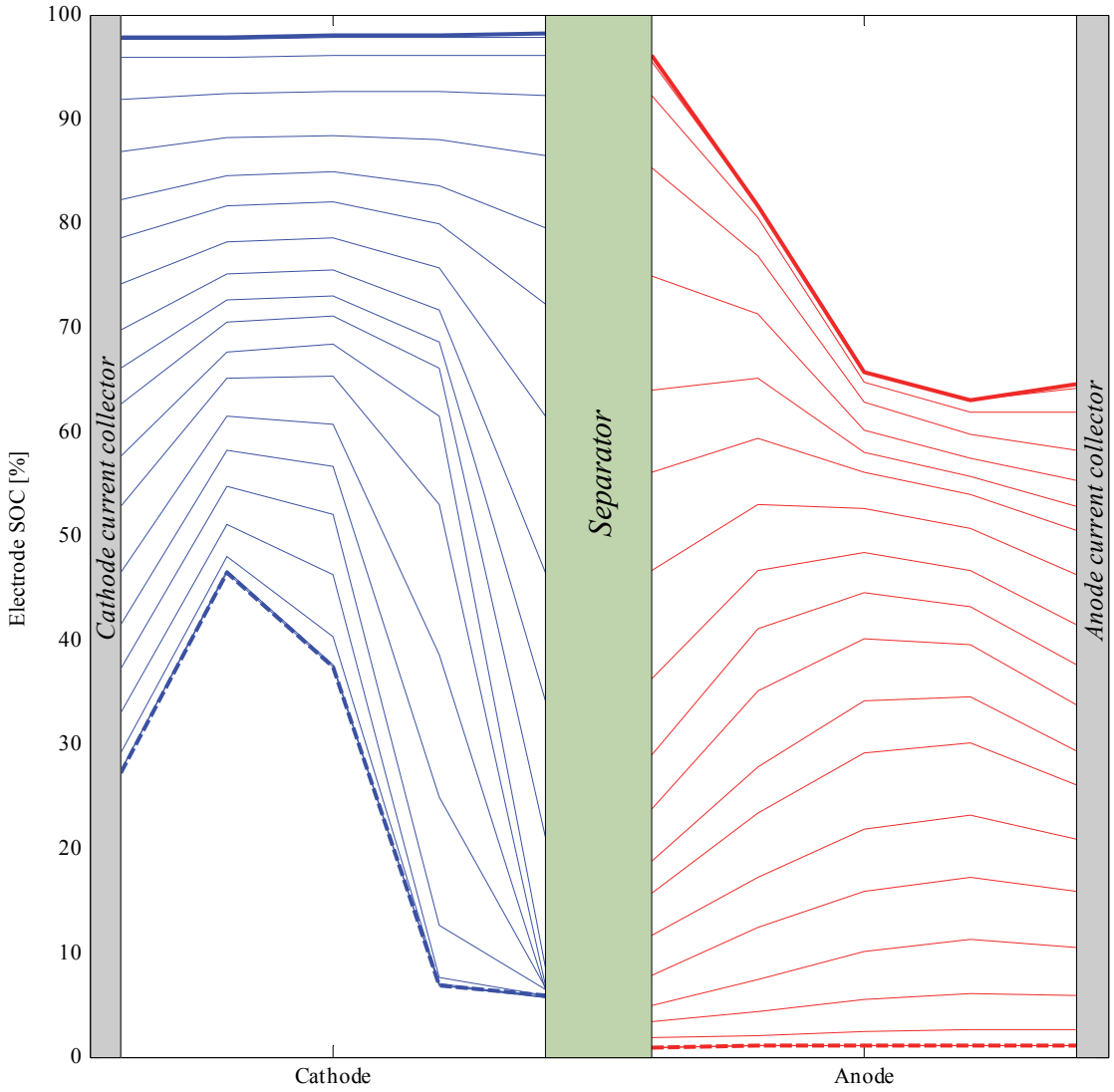

Figure 5.32 Electrode SOC distribution scaled to cell SOC vs. time during one complete discharge at 4 C-rate and +29 °C. The upper thick solid lines mark the start of discharge and the thick dashed lines mark the end of discharge. Thin lines represent the segment SOC at fixed time intervals between start and end of discharge.

The increase in current, and the segment imbalance in terms of SOC and capacity throughput, result in severely unevenly distributed ageing factors (Figure 5.33). The imbalance is nevertheless levelled out towards EOL where the increased impedance of the most degraded segments counteracts further degradation.

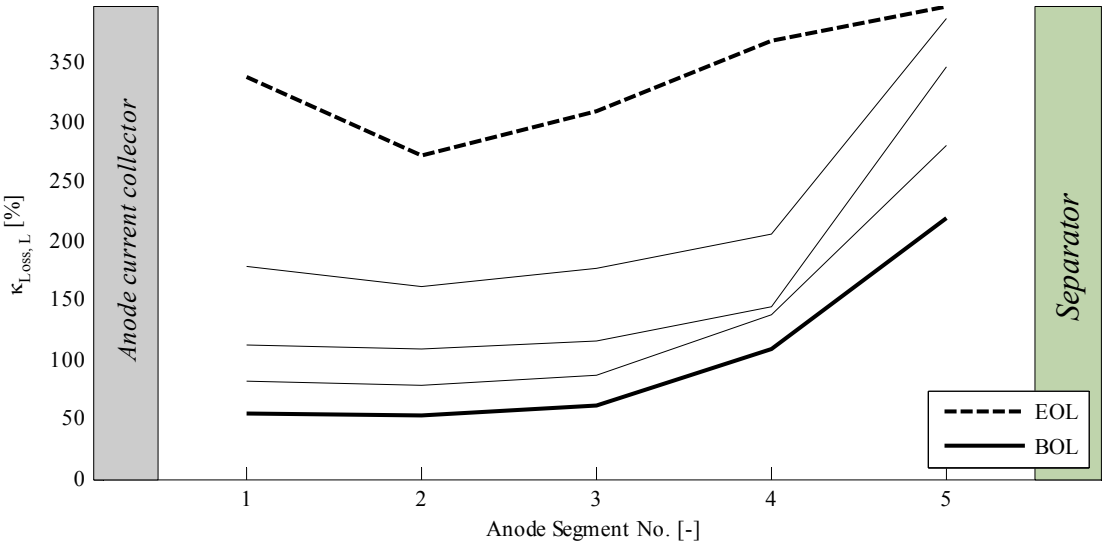

Figure 5.33 Normalised ageing factor $\kappa_{Loss,L}$ at the anode from BOL to EOL for *Cycle C* at +29 °C. Thin lines represent values between BOL and EOL at fixed interval.

The estimated cycle life (Figure 5.34) is underestimated but at least in line with measured values.

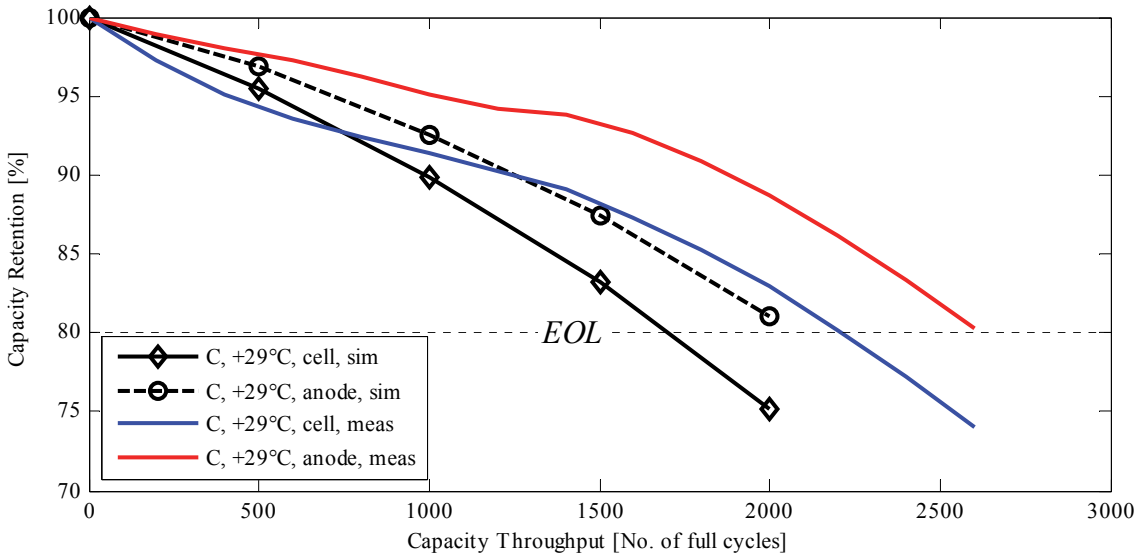

Figure 5.34 Estimated and measured cycle life of anode and cell for *Cycle C* at +29 °C

5.4.3 Model Performance at Asymmetric Cycles with High Current Rates

None of the asymmetric cycles were used in the parameterisation of the ageing model and the asymmetric *Cycle H*, with high charge rate and low discharge rate, resulted in a surprisingly low cycle life compared to *Cycle C*. This can neither be explained by the anode segment current (Figure 5.35) nor an increase in SOC imbalance (Figure 5.36); both figures show very similar characteristics compared to *Cycle C*. Clearly, further work to isolate or combine different ageing factors is needed to obtain better accuracy.

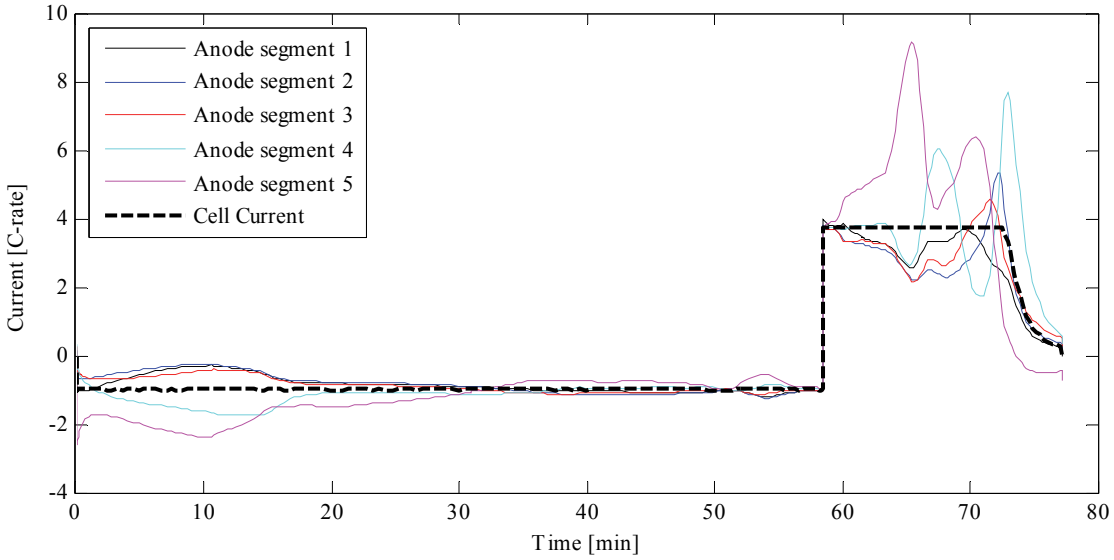

Figure 5.35 Anode segment current and total cell current vs. time for *Cycle H* at +23 °C

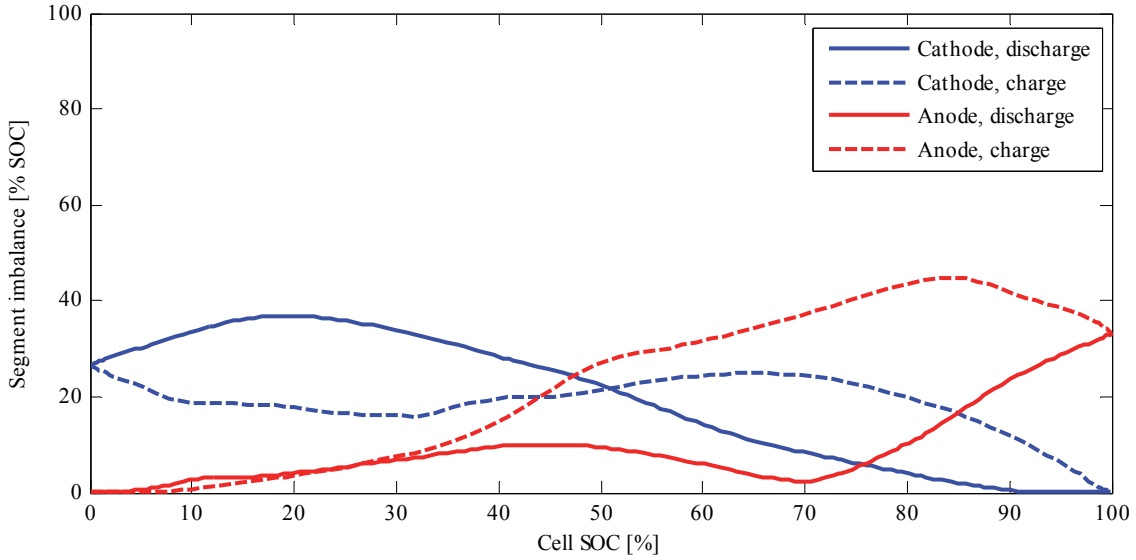

Figure 5.36 Segment imbalance in per cent vs. cell SOC, *Cycle H* at +23 °C

The resulting ageing factors do show severely uneven distribution (Figure 5.37), but still similar to that of the symmetrical cycles at the same current rate. Slight differences are observed but not significant, and in a direct comparison to *Cycle C* at +29 °C the temperature itself appears to be the most important factor causing the differences.

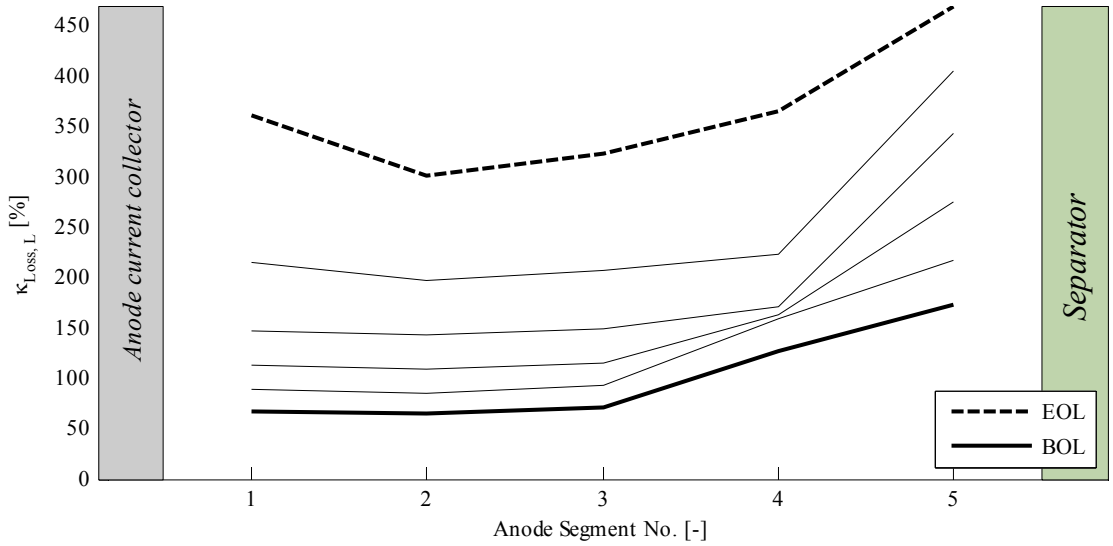

Figure 5.37 Normalised ageing factor $\kappa_{Loss,L}$ at the anode from BOL to EOL for *Cycle H* at +34 °C. Thin lines represent values between BOL and EOL at fixed interval.

Not surprisingly, the estimated cycle life of *Cycle H* (Figure 5.38) is far from accurate; in turn indicating that the model fails to capture, or to estimate, the ageing factors correctly for this cycle. Possibly, further laboratory tests may be utilised to characterise the cause of this rapid degradation.

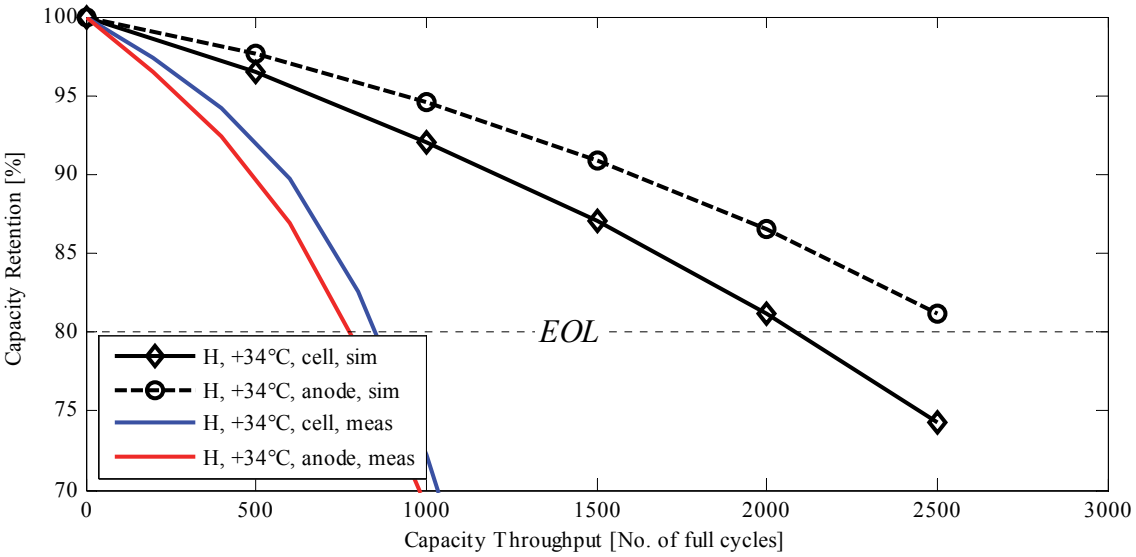

Figure 5.38 Estimated and measured cycle life of anode and cell for *Cycle H* at +34 °C

All tests with *Cycle H*, regardless of temperature, show the same results; a rapid degradation that the SOH function in the model cannot forecast.

In comparison with *Cycle H & C*, the asymmetric *Cycle I* with low charge rate and high discharge rate should, based on general guidelines, result in a longer cycle life. As already reviewed in Chapter 3, this is not the case at lower temperatures where *Cycle I* results in a shorter cycle life than both *Cycle H & C*. The ageing factors for Cycle I (Figure 5.39) are also rather evenly distributed.

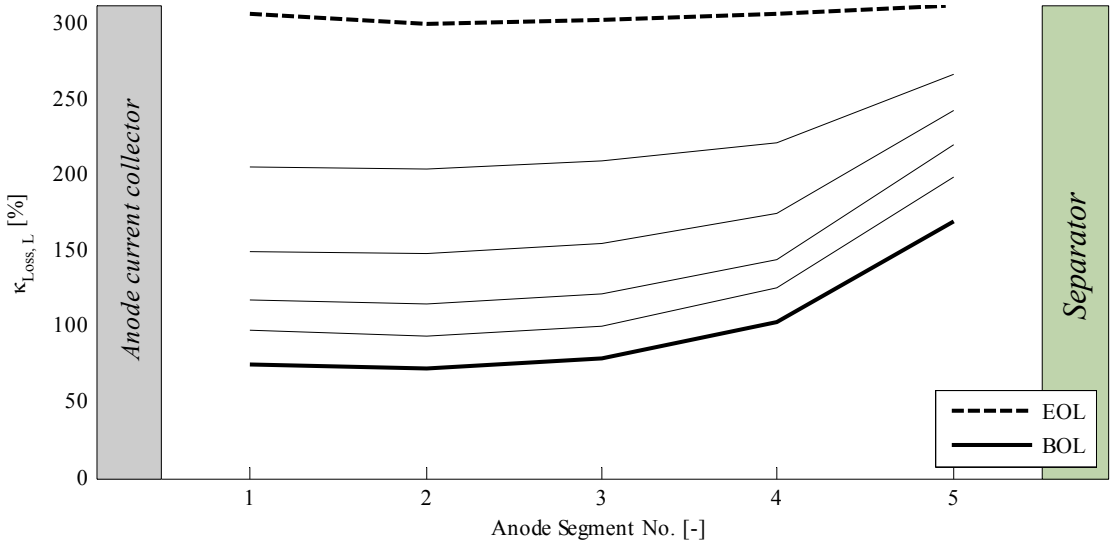

Figure 5.39 Normalised ageing factor $\kappa_{Loss,L}$ at the anode from BOL to EOL for *Cycle I* at +34 °C. Thin lines represent values between BOL and EOL at fixed interval.

Consequently, this results in a significantly longer estimated cycle life (Figure 5.40) than for *Cycle H* but still lower than the measured cycle life. Likewise to the reasoning for the other asymmetrical cycles this may indicate a need for an improved SOH function, especially for the initial ageing rate.

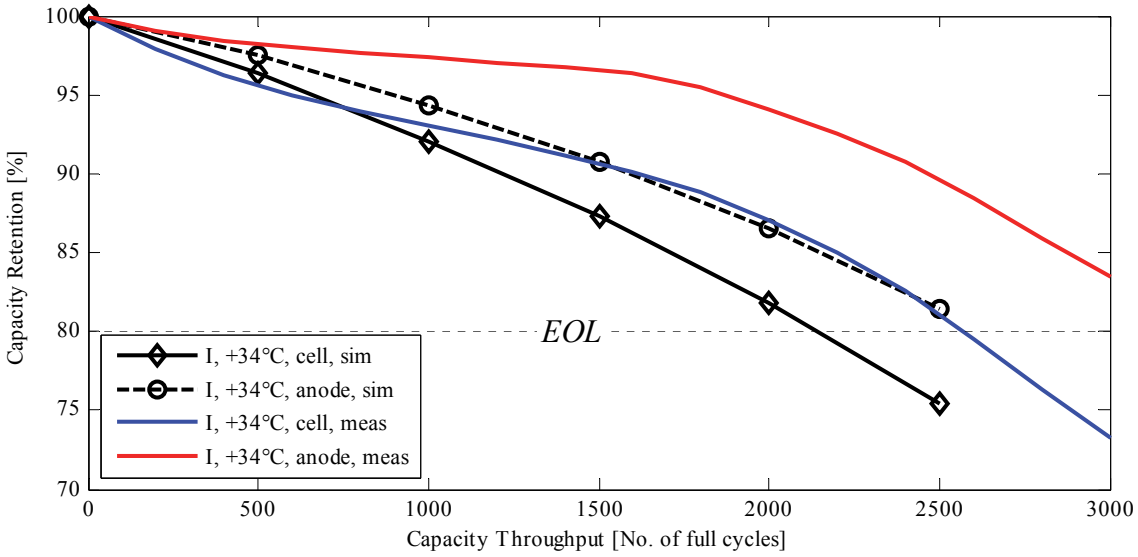

Figure 5.40 Estimated and measured cycle life of anode and cell for *Cycle I* at +34 °C

Lastly, *Cycle J*, a symmetric cycle with 4 C-rate and pauses introduced between steps, showed a very rapid ageing in laboratory tests compared to *Cycle C* regardless of temperature (see Figure 3.4). The ageing factors (Figure 5.41) are less uniform but this may in part be explained by the different average temperature, here the results from +35 °C are presented whereas *Cycle C* is measured at +29 °C.

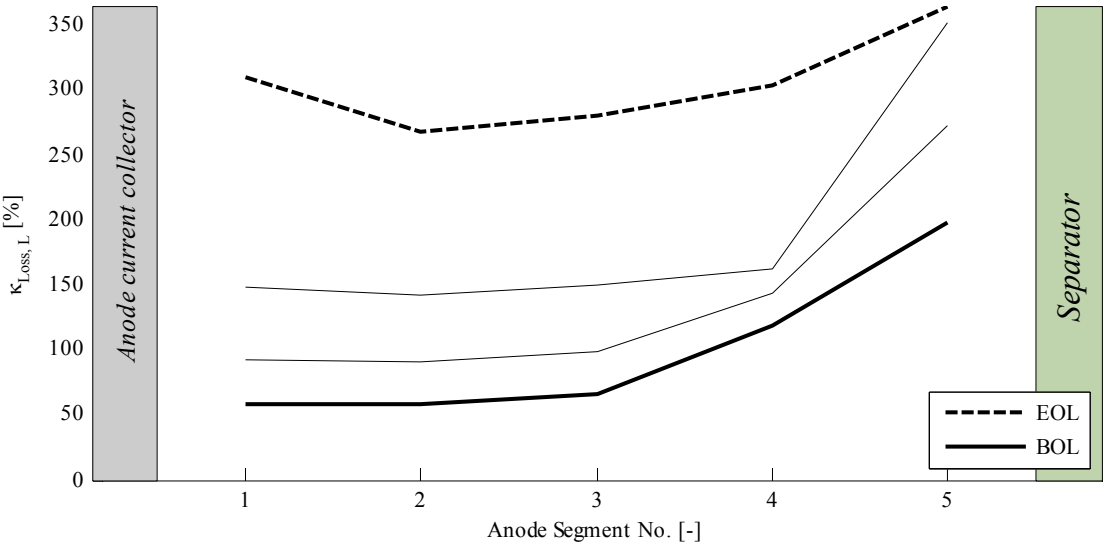

Figure 5.41 Normalised ageing factor $\kappa_{Loss,L}$ at the anode from BOL to EOL for *Cycle J* at +35 °C. Thin lines represent values between BOL and EOL at fixed interval.

Despite a shorter estimated cycle life (Figure 5.42) than for *Cycle C*, the accuracy of the model is not sufficient although a part of the additional stress *Cycle J* evidently causes is forecasted.

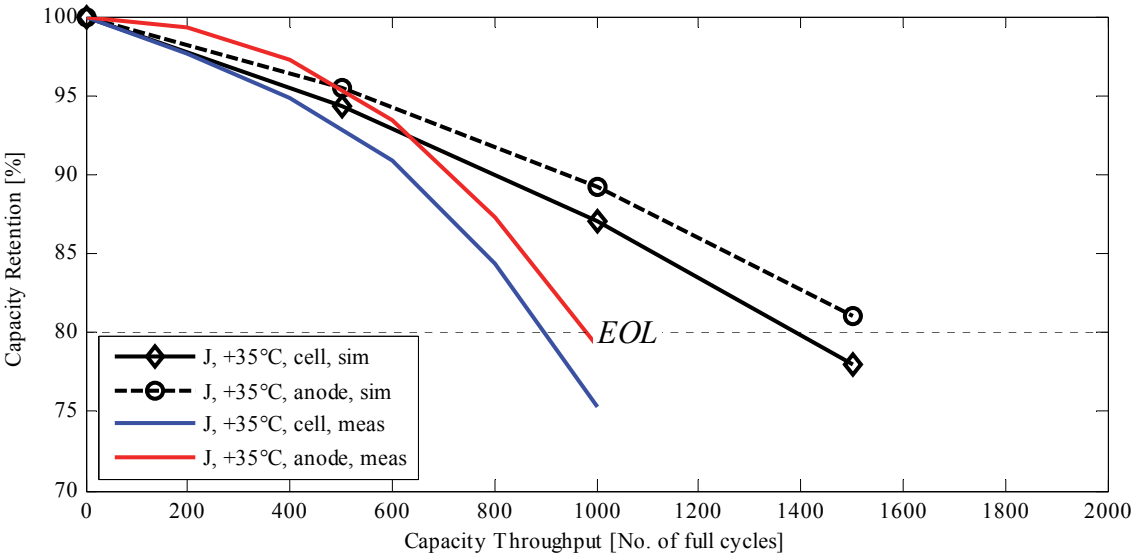

Figure 5.42 Estimated and measured cycle life of anode and cell for *Cycle J* at +35 °C

5.4.4 Model Performance at HEV and PHEV Cycles

Several HEV and PHEV cycles were designed and used in cycle life tests in the present work (see Section 2.6). The first one, *Cycle A*, is based on a logged load cycle for a HEV city-bus. The average current is approx. 4 C-rate with frequent transients up to 20 C-rates and the target SOC range is approx. 30-50% SOC.

Cycle B is a synthetic version of *Cycle A* that resulted in a slightly lower cycle life (see Table 3) than *Cycle A* and its degradation also followed another trend with relatively rapid initial loss of anode material and signs of lithium plating at MOL [1]. In contrast, when *Cycle A* was tested at a higher temperature, +39 °C, a longer cycle life was observed compared to the test with *Cycle A* at +32 °C.

The cycle life tests with these load profiles were conducted without forced air cooling. Therefore, the cell temperature varied over time and increased significantly as the impedance of the cells grew. A consequence of this is that it is difficult to find a good average value of the temperature to be used in the simulation of the ageing model, especially knowing that the temperature effect on the ageing is non-linear and path-dependent [51]. Despite this, an attempt to simulate the ageing was made, using the average temperature and SOC range for each case.

Likewise, the SOC control at medium SOC is generally difficult for LFP-cells since the OCV profile is comparably flat in the target SOC range (30-50%). In addition, complete charge and discharge was avoided in the cycle life test to prevent additional ageing. Hence, the actual SOC during the cycle life test may have varied, possibly causing increased degradation. Similarly to the temperature, an average value for the SOC range was used in the simulation.

The model responses to both cycles are similar; first and foremost the current distribution is highly non-uniform at BOL with significantly higher currents at the segments close to the separator and the current collectors, here expressed by significant differences in ageing factors (Figure 5.43) for *Cycle A*. This non-uniformity is to some extent reduced at later stages of the ageing since the degradation of the outer and inner segments of the anode leads to higher impedance in these segments, in turn shifting

currents to the segments in the middle. The non-uniformity is nevertheless surprisingly severe over the complete simulation and the trends are similar for *Cycle B*.

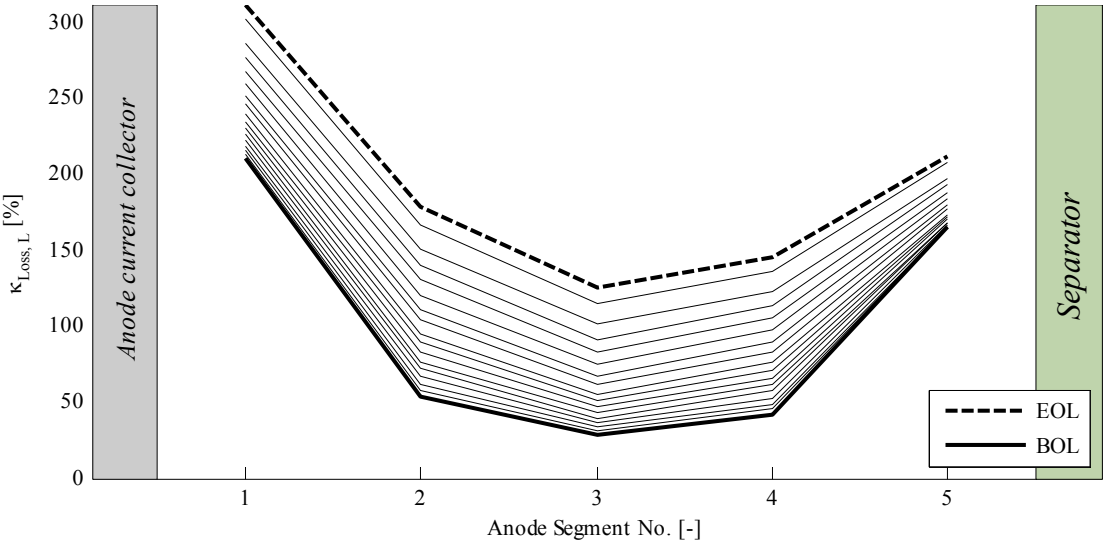

Figure 5.43 Normalised ageing factor $\kappa_{Loss,L}$ at the anode from BOL to EOL for *Cycle A* +32 °C. Thin lines represent values between BOL and EOL at fixed interval.

On the other hand, according to the model all segments operated within a narrow SOC range, well outside the area where cycle life is severely affected.

Consequently, the estimated cycle life is similar for the two HEV cycles, but with an average value close to the actual measurement (Figure 5.44). The loss of anode material is similar for both cycles and it follows the same trend as the estimated total cell capacity loss, but the model fails to predict the faster anode loss experimentally observed for *Cycle B*. This may, however, be influenced by the lack of precise temperature and SOC control in the laboratory test, causing HEV *Cycle B* to age the tested cells slightly faster than for HEV *Cycle A*.

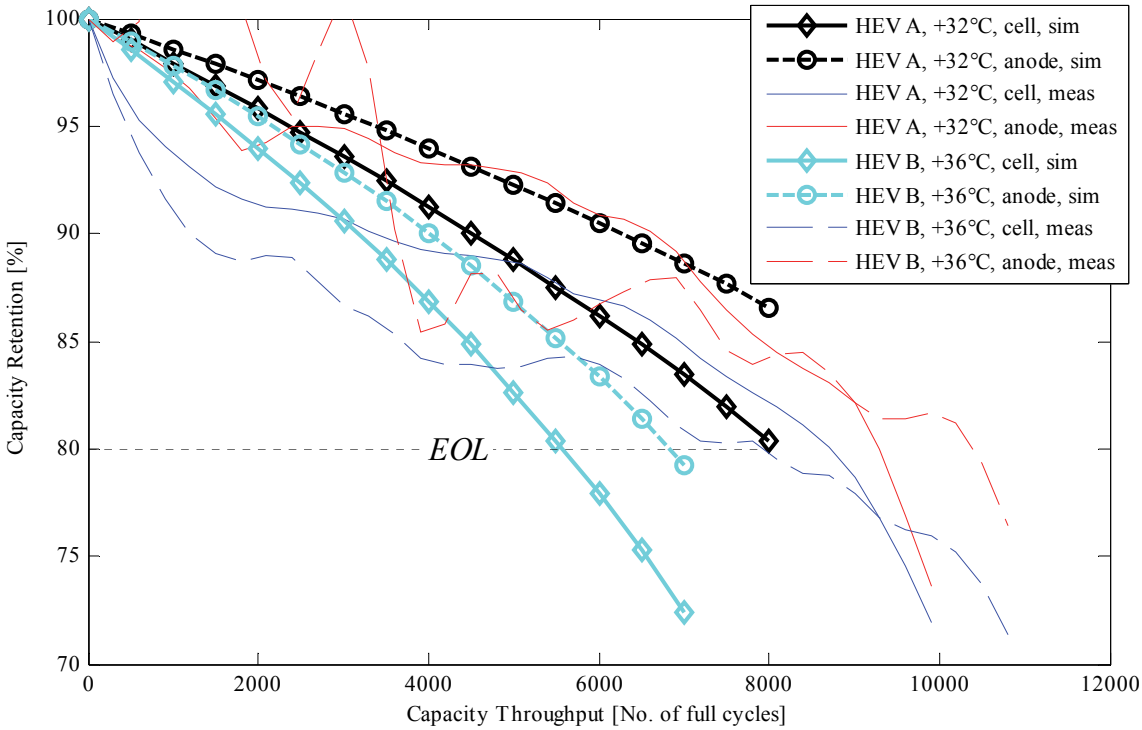

Figure 5.44 Estimated and measured cycle life of anode and cathode for HEV *Cycle A* at +32 °C compared to HEV *Cycle B* at +36 °C

Still, the model fails to capture the fast degradation at the first stages of ageing and the plateau at MOL often seen in this type of cycling.

The PHEV *Cycle E* & *F* are not based on logged data but were simulated in a full-vehicle simulation. Both consist of a charge depleting load cycle starting at full SOC for approx. 1h followed by a rapid re-charge at constant current, 2 C-rate for *Cycle E* and 4 C-rate for *Cycle F*. Further descriptions of these load cycles are given in Section 2.6 and in [1].

The simulated ageing factors per segment (Figure 5.45 & Figure 5.46) are noteworthy different for the two cycles with a more uniform distribution for PHEV *Cycle E*. In addition, the ageing accelerates dramatically towards EOL, more than for any other cycles.

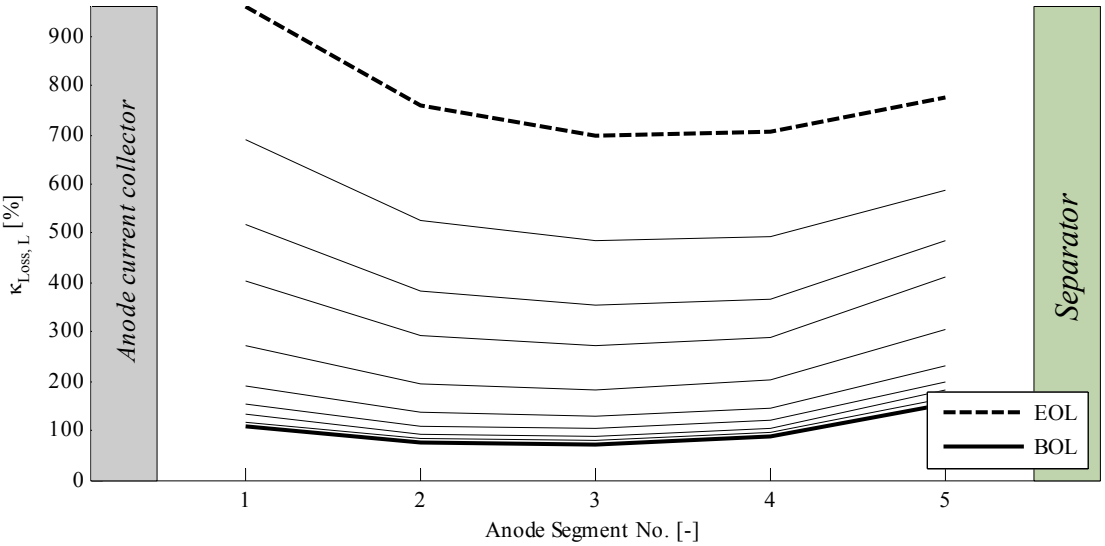

Figure 5.45 Normalised ageing factor $\kappa_{Loss,L}$ at the anode from BOL to EOL for *Cycle E* +35 °C. Thin lines represent values between BOL and EOL at fixed interval.

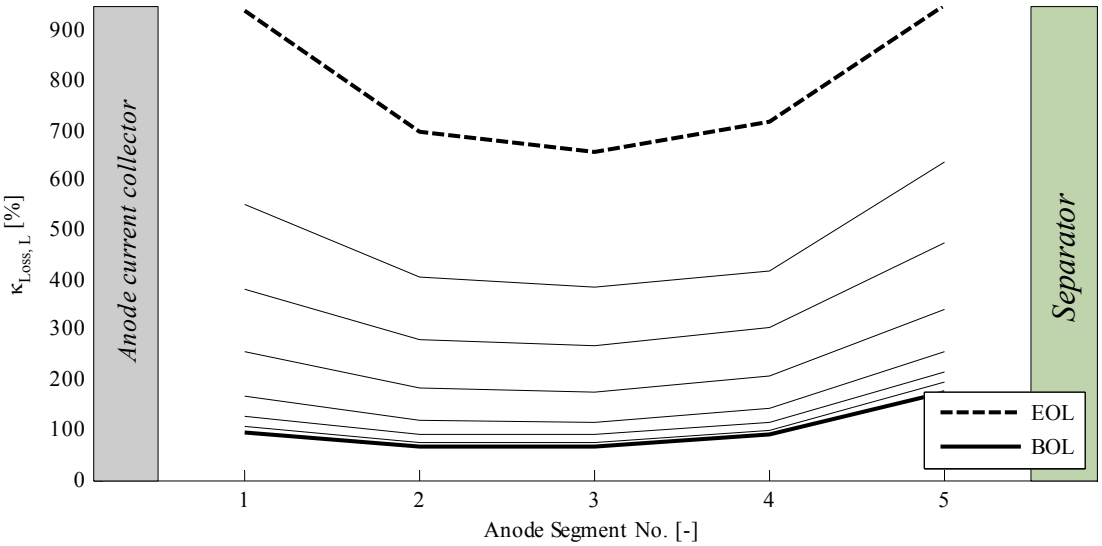

Figure 5.46 Normalised ageing factor $\kappa_{Loss,L}$ at the anode from BOL to EOL for *Cycle F* +30 °C. Thin lines represent values between BOL and EOL at fixed interval.

On the other hand, the model does not capture the overall ageing rate well for PHEV *Cycle F* since the discrepancy between laboratory data and estimation is profound, similarly to that of *Cycle H* that also contains a combination of slow discharge and fast charge.

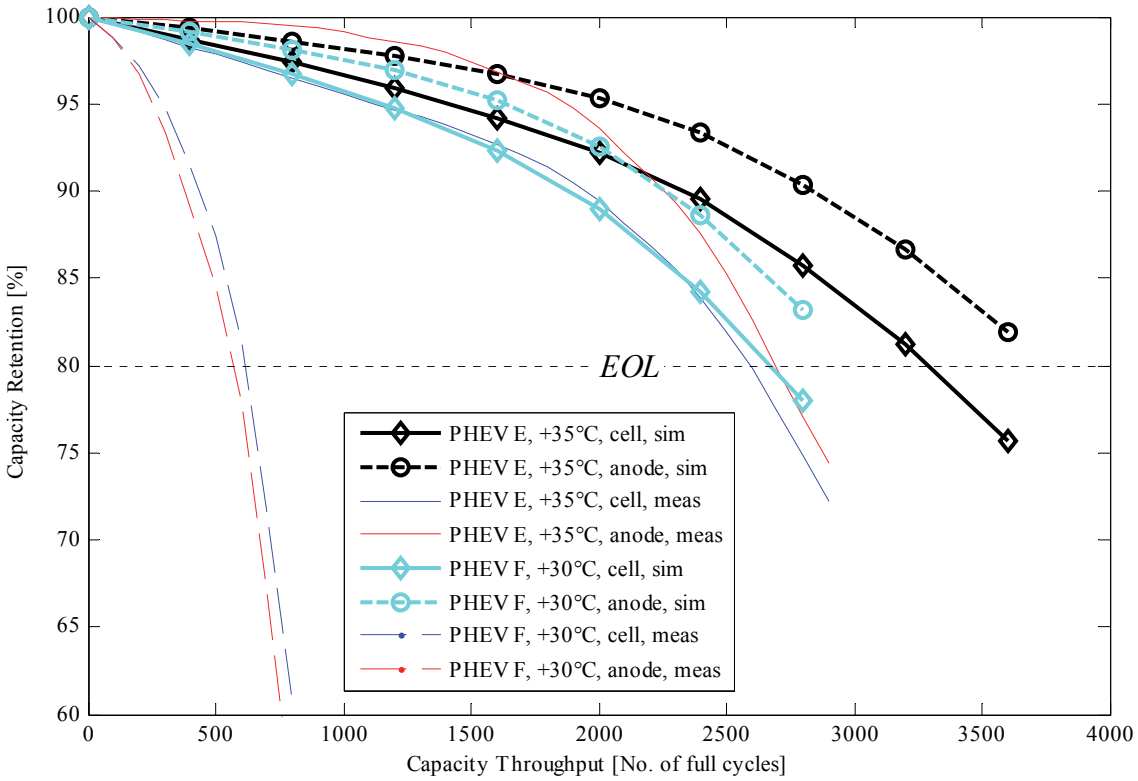

Figure 5.47 Estimated and measured cycle life of anode and cell for PHEV *Cycle E* at +35 °C and PHEV *Cycle F* at +30 °C

5.5 Validation Summary

The results suggest that the temperature indeed can be seen as a general ageing factor, *i.e.* an independent factor provided that the effect the temperature has on cell performance is taken into account. Likewise, the capacity throughput in different parts of the electrode appears to act as an independent factor.

On the other hand, the SOC has a profound effect on the degradation rate but in contrast to the temperature and the capacity throughput this ageing factor does not appear to be fully independent. That is, the ageing rate depending on the cell SOC may also be depending on other factors such as time, capacity throughput and local current density. Also, the test results suggest that it is highly non-linear. Hence, carefully measured degradation rates are required to derive relevant and accurate empirical relations, possibly also depending on other ageing factors.

Although the current rate at charge and discharge indeed can be treated as an ageing factor, the effect on cycle life is definitely depending on how charge and discharge steps

are combined; the average current is a poor approximation that is invalid for cycles with large differences in charge and discharge current. Also, when pauses are introduced other ageing effects must be considered. Possibly the time the cell spent at high or low SOC has an effect on the ageing rate in such cases, an effect not observed for any other cases treated in the present work.

In summary, the presented model and the resulting simulations show a fair accuracy for symmetrical cycles and for complex cycles operated at partial SOC, but lack accuracy for asymmetrical cycles, in particular cycles with low average discharge current and high average charge current or for cycles with pauses in between steps. Thus, the proposed model may be regarded as a first step towards a model with low complexity and sufficiently high accuracy.

Chapter 6 Concluding Remarks

Whereas some ageing mechanisms such as loss of active anode material, can be isolated from other mechanisms and characterised in terms of average loss *ex situ* using incremental capacity analysis, differential voltage analysis and fitting towards half-cell voltage profiles, it is often difficult to distinguish between loss of cyclable lithium and loss of active cathode material. Although detailed measurements at C/10 were performed for both charge and discharge, none of the above mentioned methods proved to be able to isolate the loss of active cathode material robustly. Possibly, voltage profiles at C/20 or even lower current rates, or using more sensitive test equipment, could enable a more stable estimation.

The high power graphite || $LiFePO_4$ cells studied in the present work show an interesting ageing behaviour when either high current rates are combined with low current rates or rest periods. In particular, cells cycled with 4 C-rate charge and 1 C-rate discharge over a wide SOC window showed rapid aging and loss of active anode material compared to symmetric cycling with 4 C-rate, regardless of temperature. This behaviour was also observed for the PHEV cycle that operated in a slightly reduced SOC region. Thus, fast charging of batteries used in PHEVs and EVs may induce substantial and additional stress to the battery, at least if the cells are operated in a comparably wide SOC region. Still, this has to be verified and characterised with additional tests. Also, this conclusion may not be valid for other cell types or designs. Furthermore, rapid and unexpected degradation was also observed when comparably short rest periods are introduced in between charge and discharge steps at 4 C-rate. This test resulted in short cycle life and rapid loss of active anode material. In contrast, when cells are cycled in a small SOC-window, the cycle life is significantly increased even though the peak currents are relatively high, up to 20 C-rates. Consequently, more research is needed to explain this behaviour, preferably using a combination of extensive testing and *post mortem* analysis.

The cycle life of cells cycled with simplified and symmetric load cycles with wide SOC range can relatively easy be estimated using empirical relations, at least within the investigated temperature and current rate, provided that sufficient experimental data is

available for validation. In addition, fairly simple relations for SOC range dependence can be utilised to estimate the cycle life of cells cycled in narrow SOC ranges and with simple cycles. Nevertheless, more complex models are needed in order to accurately forecast end of life for cells cycled with real load cycles, particularly if fast-charging is considered.

The lumped parameter model presented in this thesis demonstrated an ability to estimate the distribution of currents, SOC and hence ageing rates within the cross section of a Li-ion cell. Despite the lack of low-level validation, the model shows similar response as more complex first-principles physical models and the distribution of cycle life between segments also show similar trends as the *post mortem* analysis showed (*Paper IV*); uneven degradation. Furthermore, the parameterisation of the model proved to be reasonably simple with most effort needed to find relevant ageing functions, again indicating that extensive laboratory testing is still needed to validate ageing models.

Consequently, with a model complexity acceptable for use in full vehicle and/or energy storage simulations, the model showed promising results, especially when performing a step-wise simulation over the cycle life of cells aged with an HEV cycle.

Chapter 7 Future Work

Firstly, a larger test matrix for characterising ageing is needed, in particular to study the effect of rapid charging in combination with moderate, or mixed, discharging. Such a test matrix should not only rely on classical design of experiment (DOE) methods, but also rely on electrochemical analysis of sample cells to effectively target the specific load conditions believed to cause rapid degradation. Furthermore, *post mortem* analysis should be done on selected cells at EOL to validate *ex situ* characterisation techniques.

Secondly, when testing cells with the aim to not only characterise ageing, but also parameterise ageing models, it is of uttermost importance to control all possible ageing factors precisely. Hence, special efforts should be made to improve non-destructive characterisation techniques described in this thesis further and to keep known ageing factors such as temperature and SOC range as stable as possible throughout a cycle life test. Also, half-cell experiments would improve the quality of the parameter fitting and enable a complete separation of anode and cathode behaviour.

Lastly, the model presented here may serve as a first step towards a semi-empirical ageing model with acceptable overall accuracy, hence important improvements are likely if additional ageing functions are included and validated, especially for electrode degradation, physical modelling of SEI growth and for transient operation at high current rates. In addition, the path-dependence of the degradation should be included as well as the effect of calendar / time dependent aging. Also, a closed loop simulation should be performed were not only the estimated ageing directly affects the cell model parameters, but also the temperature and the state-of-health of the cell, thus continuously changing the ageing rate. Furthermore, other Li-ion cell types should be considered to expand the feasibility of the model and to further verify its validity as being a compromise between accuracy and computational effort.

Chapter 8 References

[1] J. Groot, *"State-of-Health Estimation of li-ion Batteries: Cycle Life Test Methods"*, Licentiate Thesis, Chalmers University of Technology, (2012).

[2] K. Amine, C.H. Chen, J. Liu, M. Hammond, A. Jansen, D. Dees, I. Bloom, D. Vissers, G. Henriksen*, "Factors responsible for impedance rise in high power lithium ion batteries"*, Journal of Power Sources 97-98 (2001) 684-687.

[3] I. Bloom, B.W. Cole, J.J Sohn, S.A. Jones, E.G. Polzin, V.S. Battaglia, G.L. Henriksen, C. Motlach, R. Richardson, T. Unkelhaeuser, D. Ingersoll, H.L. Case, *"An accelerated calendar and cycle life study of Li-ion cells"*, Journal of Power Sources 101 (2001) 238-247.

[4] M. Broussely, Ph. Biensan, F. Bonhomme, Ph. Blanchard, S. Herreyre, K. Nechev, R.J. Staniewicz, *"Main aging mechanisms in Li ion batteries"*, Journal of Power Sources 146 (2005) 90–96.

[5] J. Vetter, P. Novák, M.R. Wagner, C. Veit, K-C. Möller, J.O. Besenhard, M. Winter, M. Wohlfahrt-Mehrens, C. Vogler, A. Hammouche, *"Ageing mechanisms in lithium-ion batteries"*, Journal of Power Sources 147 (2005) 269–281.

[6] D.P. Abraham, E.M. Reynolds, E. Sammann, A.N. Jansen, D.W. Dees, *"Aging characteristics of high-power lithium-ion cells with $LiNi_{0.8}Co_{0.15}Al_{0.05}O_2$ and $Li_{4/3}Ti_{5/3}O_4$ electrodes",* Electrochimica Acta 51 (2005) 502–510.

[7] J. Li, E. Murphy, J. Winnick, P.A. Kohl, *"Studies on the cycle life of commercial lithium ion batteries during rapid charge–discharge cycling"*, Journal of Power Sources 102 (2001) 294–301 .

[8] M. Safari, C. Delacourt, "*Aging of a Commercial Graphite/$LiFePO_4$ Cell*", Journal of The Electrochemical Society 158 (10) (2011) A1123-A1135

[9] M. Dubarry, B.Y. Liaw, *"Identify capacity fading mechanism in a commercial $LiFePO_4$ cell"*, Journal of Power Sources 194 (2009) 541–549.

[10] P. Liu, J. Wang, J. Hicks-Garner, E. Sherman, S. Soukiazian, M. Verbrugge, H. Tataria, J. Musser, P. Finamore, *"Ageing Mechanisms of $LiFePO_4$ Batteries Deduced by Electrochemical and Structural Analyses"*, Journal of The Electrochemical Society 157 (4) (2010), A499-A507.

[11] K. Amine, J. Liu, I. Belharouak, *"High-temperature storage and cycling of C-$LiFePO_4$/graphite Li-ion cells"*, Electrochemistry Communications 7 (2005) 669–673 .

[12] M. Dubarry, B.Y. Liaw, M-S. Chen, S-S. Chyan, K-C. Han, W-T. Sie, S-H. Wu, *"Identifying battery aging mechanisms in large format Liion cells"*, Journal of Power Sources 196 (2011) 3420-3425.

[13] Y. Zhang, C-Y. Wang, X. Tang, *"Cycling degradation of an automotive $LiFePO_4$ lithium-ion battery",* Journal of Power Sources 196 (2011) 1513–1520.

[14] K.A. Striebel, J. Shim, *"Cycling performance of low-cost lithium ion batteries with natural graphite and $LiFePO_4$",* Journal of Power Sources 119-121 (2003), 955-958.

[15] T.G. Zavalis, M. Klett, M.H. Kjell, M. Behm, R.W. Lindström, G. Lindbergh, "*Aging in lithium-ion batteries: Model and experimental investigation of harvested $LiFePO_4$ and mesocarbon microbead graphite electrodes*", Electrochimica Acta 110 (2013) 335-348.

[16] D.P. Abraham, S.D. Poppen, A.N. Jansen, J. Liu, D.W. Dees, "*Application of a lithium–tin reference electrode to determine electrode contributions to impedance rise in high-power lithium-ion cells*", Electrochimica Acta 49 (2004) 4763–4775.

[17] S.C. Nagpure, R. Dinwiddie, S.S. Babu, G. Rizzoni, B. Bhushan, T. Frech, "*Thermal diffusivity study of aged Li-ion batteries using flash method*", Journal of Power Sources 195 (2010) 872-876.

[18] S.C. Nagpure, B. Bhushan, S.S. Babu, *"Multi-Scale Characterization Studies of Aged Li-Ion Large Format Cells for Improved Performance: An Overview "*, Journal of The Electrochemical Society 160 (11) (2013) A2111-A2154.

[19] S.C. Nagpure, B. Bhushan, S. Babu, G. Rizzoni, *"Scanning spreading resistance characterization of aged Li-ion batteries using atomic force microscopy"*, Scripta Materialia 60 (2009) 933–936.

[20] P. Ramadass, B. Haran, R.White, B.N. Popov, *"Mathematical modeling of the capacity fade of Li-ion cells"*, Journal of Power Sources 123 (2003) 230–240.

[21] E. Prada, D. Di Domenico, Y. Creff, J. Bernard, V. Sauvant-Moynot, F. Huet, "*Simplified Electrochemical and Thermal Model of $LiFePO_4$-Graphite Li-Ion Batteries for Fast Charge Applications*", Journal of Power Sources 159 (9) (2012) A1508-A1519

[22] E. Prada, D. Di Domenico, Y. Creff, J. Bernard, V. Sauvant-Moynot, F. Huet, "*A Simplified Electrochemical and Thermal Aging Model of $LiFePO_4$-Graphite Li-ion Batteries: Power and Capacity Fade Simulations*", Journal of Power Sources 160 (4) (2013) A616-A628

[23] G. Ning, R.E. White, B.N. Popov,*"A generalized cycle life model of rechargeable Li-ion batteries"*, Electrochimica Acta 51 (2006) 2012–2022.

[24] G. Ning, B.N. Popov, "*Cycle Life Modeling of lithium-Ion Batteries",* Journal of the Electrochemical Society 151 (10) (2004) A1584-A1591.

[25] K.A. Smith, C. D. Rahn, C-Y. Wang, *"Control oriented 1D electrochemical model of lithium ion battery"*, Energy Conversion and Management 48 (2007) 2565–2578.

[26] P. Singh, R. Vinjamuri, X. Wang, D. Reisner, *"Fuzzy logic modeling of EIS measurements on lithium-ion batteries"*, Electrochimica Acta 51 (2006) 1673–1679.

[27] P. Singh, R. Vinjamuri, X. Wang, D. Reisner, "*Design and implementation of a fuzzy logic-based state-of-charge meter for Li-ion batteries used in portable defibrillators*", Journal of Power Sources 162 (2006) 829–836.

[28] R. Spotnitz, *"Simulation of capacity fade in lithium ion batteries"*, Journal of Power Sources 113 (2003) 72-80.

[29] V. Pop, H.J. Bergveld, P.H.L. Notten, J.H.G. Op het Veld, P.P.L. Regtien, *"Accuracy analysis of the State-of-Charge and remaining run-time determination for lithium-ion batteries"*, Measurement 42 (2009) 1131–1138.

[30] A.T. Stamps, C.E. Holland, R.E. White, E.P. Gatzke, *"Analysis of capacity fade in a lithium ion battery"*, Journal of Power Sources 150 (2005) 229–239.

[31] M. Safari, M. Morcrette, A. Teyssot, C. Delacourt, *"Multimodal Physics-Based Aging Model for Life Prediction of Li-Ion Batteries"*, Journal of The Electrochemical Society 156 (3) (2009) A145-A153.

[32] J-W. Lee, Y.K. Anguchamy, B.N. Popov, "*Simulation of charge–discharge cycling of lithium-ion batteries under low-earth-orbit conditions"*, Journal of Power Sources 162 (2006) 1395–1400.

[33] M. Swierczynski, "*Lithium ion battery energy storage system for augmented wind power plants*", PhD Thesis, Aalborg University (2013)

[34] M. Swierczynski, D.I. Stroe, A.I. Stan, R. Teodorescu, H. Vikelgaard, "*Selection and impedance based model of a lithium ion battery technology for integration with virtual power plant*", 15th European Conference on In Power Electronics and Applications (EPE) (2013), p1-10.

[35] D.-I. Stroe, M. Swierczynski, A.-I. Stan, V. Knap, R. Teodorescu, S.J. Andreasen, "*Diagnosis of lithium-ion batteries state-of-health based on electrochemical impedance spectroscopy technique*", Energy Conversion Congress and Exposition (ECCE), (2014) IEEE, 2014, in press.

[36] M. Kassem, J. Bernard, R. Revel, S. Pélissier, F. Duclaud, C. Delacourt, "*Calendar aging of a graphite/LiFePO$_4$ cell*", Journal of Power Sources 208 (2012) 296–305

[37] J. Wang, P. Liu, J. Hicks-Garner, E. Sherman, S. Soukiazian, M. Verbrugge, H. Tataria, J. Musser, P. Finamore, "*Cycle-life model for graphite-LiFePO$_4$ cells*", Journal of Power Sources 196 (2011) 3942–3948

[38] M. Fleckenstein, O. Bohlen, M.A. Roscher, B. Bäker, "*Current density and state of charge inhomogeneities in Li-ion battery cells with LiFePO$_4$ as cathode material due to temperature gradients*", Journal of Power Sources 196 (2011) 4769-4778

[39] A123 Systems, Inc., "*High Power Lithium Ion ANR26650M1A*", Document No. MD100001-02, April 2009

[40] A123 Systems, Inc., "*SAFETY DATA SHEET, High Power Lithium Ion Cell, Phosphate-Based*", Document No. SF000003_16, Revised 2009-10-13

[41] "*Series 4000 - Industry Standard Automated Cell and Battery Test System*", http://www.maccor.com/series4000.php, accessed 2011-12-28.

[42] *"Reference 3000 Potentiostat » Gamry Instruments"*, http://www.gamry.com/products/potentiostats/reference-3000, accessed 2011-12-28.

[43] M. Dubarry, V. Svoboda, R. Hwu, B.Y. Liaw, "*Incremental Capacity Analysis and Close-to-Equilibrium OCV Measurements to Quantify Capacity Fade in Commercial Rechargeable lithium Batteries*", Electrochemical and Solid-State Letters 9 (10) (2006) A454-A457.

[44] I. Bloom, A.N. Jansen, D.P. Abraham, J. Knuth, S.A. Jones, V.S. Battaglia, G.L. Henriksen, "*Differential voltage analyses of high-power, lithium-ion cells 1. Technique and application*", Journal of Power Sources 139 (2005) 295–303.

[45] I. Bloom, J. Christophersen, K. Gering, "*Differential voltage analyses of high-power lithium-ion cells 2. Applications*", Journal of Power Sources 139 (2005) 304–313.

[46] I. Bloom, J.P. Christophersen, D.P. Abraham, K.L. Gering, "*Differential voltage analyses of high-power lithium-ion cells 3. Another anode phenomenon*", Journal of Power Sources 157 (2006) 537–542.

[47] I. Bloom, L.K. Walker, J.K. Basco, D.P. Abraham, J.P. Christophersen, C. D. Ho,"*Differential voltage analyses of high-power lithium-ion cells. 4. Cells containing NMC*", Journal of Power Sources 195 (2010) 877–882.

[48] F. La Mantia, J. Vetter, P. Novák, "*Impedance spectroscopy on porous materials: A general model and application to graphite electrodes of lithium-ion batteries*", Electrochimica Acta 53 (2008) 4109–4121.

[49] W. Prochazka, G. Pregartner, M. Cifrain, "*Design-of-Experiment and Statistical Modeling of a Large Scale Aging Experiment for Two Popular Lithium Ion Cell Chemistries"*, Journal of Power Sources 160(8) (2013) A1039-A1051

[50] J.R. Belt, C.D. Ho, C.G. Motloch, T.J. Miller, T.Q. Duong, "*A capacity and power fade study of Li-ion cells during life cycle testing*", Journal of Power Sources 123 (2003) 241-246

[51] K. L. Gering, S.V. Sazhin, D. K. Jamison, C. J. Michelbacher, B. Y. Liaw, M. Dubarry, M. Cugnet, "*Investigation of path dependence in commercial lithium-ion cells chosen for plug-in hybrid vehicle duty cycle protocol"*, Journal of Power Sources 196 (2011) 3395-3403.